Master's thesis

NTNU
Norwegian University of Science and Technology
Faculty of Natural Sciences
Department of Physics

Kristoffer Engedal Andreassen

Active matter states of self-propelled dipolar particles

Master's thesis in Fysikk og matematikk
Supervisor: Paul Gunnar Dommersnes
July 2019

NTNU
Norwegian University of
Science and Technology

Kristoffer Engedal Andreassen

Active matter states of self-propelled dipolar particles

Master's thesis in Fysikk og matematikk
Supervisor: Paul Gunnar Dommersnes
July 2019

Norwegian University of Science and Technology
Faculty of Natural Sciences
Department of Physics

NTNU
Norwegian University of
Science and Technology

NTNU
Norwegian University of
Science and Technology

Active matter states of self-propelled dipolar particles

Kristoffer Engedal Andreassen
Trondheim, July 2019

NTNU - Norwegian University of Science and Technology
Faculty of Natural Sciences
Department of Physics
TFY4900 - Physics, Master's Thesis

Sammendrag

Vi simulerer et 2D ensemble av selvdrevne partikler med dipolvekselvirkning. Dette er et eksempel på et aktivt system, en type mykt kondensert materie som oppstår i dyreflokker så vel som i mikroskopiske, selvdrevne kolloider. Vi sammenligner modellen vår med den minimale Vicsek-modellen og motiverer bruken av dipolvekselvirkninger på bakgrunn av deres fysiske enkelhet og utbredelse.

Likningene til dreiemoment og kraft mellom dipoler utledes, og sammen et stokastisk rotasjonsdiffusjonsledd danner de et sett med overdempede bevegelseslikninger. Disse stokastiske differensiallikningene integreres med en adaptiv to-steg Adams-Bashford-metode.

Uten selvdrift vil dipolpartiklene danne kjeder og ringer, som tolererer en viss mengde støy i form av rotasjonsdiffusjon før strukturene kollapser. Med selvdrift vil partikkelsystemet befinne seg i en diffunderende gassfase ved høy rotasjonsdiffusjon og i en polar væskefase som svømmer i en vilkårlig retning ved lav rotasjonsdiffusjon, et symmetribrudd som kan direkte sammenlignes med den vi ser i Vicsek-modellen med periodiske grensebetingelser.

Med sirkulær innesperring vil partiklene kondensere til en heksatisk-lignende fase som roterer langs veggen til domenet, og denne fasen sameksisterer og veksler partikler med en gassfase i sentrum av domenet. Denne oppførselen står i kontrast til den typiske oppførselen observert i andre innesperrede, aktive systemer i simuleringer og eksperimenter, hvor det ikke er et slikt tydelig grensesnitt. Vi foreslår at dette er en konsekvens av kombinasjonen av dipoltiltrekning og mykkjernefrastøting i modellen vår.

Abstract

We simulate a 2D ensemble of self-propelled particles with dipole-dipole interactions. This is an example of an active matter system, a type of soft condensed matter that can manifest itself in flocks of animals as well as in microscopic propelled colloids. We compare our model to the minimal Vicsek model and motivate the use of dipole interactions due to their physical simplicity and ubiquity.

The equations for torque and force between dipoles are derived, which are combined with a stochastic rotational diffusion term into a set of overdamped equations of motion. These stochastic differential equations are integrated using an adaptive two-step Adams-Bashford scheme.

Without propulsion the dipolar particles form chains and rings, which can tolerate some level of noise in the form of rotational diffusion before the structures collapse. With self-propulsion the system enters a diffusive gas phase for high rotational diffusion and a polar liquid phase swimming in an arbitrary direction for low diffusion, a symmetry breaking behaviour directly analogous to the Vicsek model with periodic boundary conditions.

With circular confinement, the particles condense into a hexatic-like phase rotating along the boundary, which coexists and exchanges particles with a gaseous phase in the central region of the domain. This behaviour is in contrast to the typical behaviour observed in other confined active matter simulations and experiments, where there is no clear interface. We hypothesise this is caused by the combination of the dipole attraction and soft-core repulsion in our model.

Contents

1 | Preface

This work is the continuation of my master's project last semester at NTNU's Soft and Complex Matter Lab[1]. In that project we experimented with microscopic particle systems using ferromagnetic fluids and external magnetic fields, with the goal of finding applications within the greater context of active matter. In the end, this particular experimental setup ended up being more relevant for self-assembly than for active matter, but the numerical simulations done to demonstrate an ideal active matter system motivated further investigations into such systems. Therefore I decided to pursue a purely numerical and theoretical project as the final master's thesis, which is what you're reading right now.

Essentially all code used in this project, both for simulations, data analysis and plotting, was written from scratch in Python with the help of scientific computing packages NumPy, SciPy and Matplotlib. Creating a serviceable framework was therefore crucial to not drown in an endless amount of similar scripts, and so was the need to create routines which track the simulation progress and which can be run over long periods on both home computers and external servers. This engineering aspect of the thesis work may not be exhaustively covered in a written report like this, but the process of developing these tools and skills was a very rewarding learning experience.

The most important collaborator in this thesis work has of course been my supervisor **Paul Gunnar Dommersnes**, who has guided and assisted me throughout the semester, be it at meetings during his visits to Trondheim or via after-work Skype calls. This work would simply not have existed without his encouragement and I want to thank him for the opportunity to do this master's thesis.

I would also like to thank Terje Røsten and Ingve Simonsen at NTNU for helping me with the practicalities of using the Department of Physics' Linux clusters for my simulations. And I would also like to mention Job Thijssen and Davide Marenduzzo at the University of Edinburgh, who during my exchange year there opened my eyes to the world of soft matter physics and reaffirmed my interest in computational physics.

Finally, I want to thank all my fellow students of Applied Physics and Mathematics here at NTNU, without whom these 5 years would have been decidedly less fun. *Alt er relativt!*

[1] `https://www.ntnu.edu/physics/research/soft-complex`

2 | Introduction

Physics can give off the impression that it solely deals with "dead" objects. A rock does not have a say in how it should fly through the air any more than an atom can decide what orbitals its electrons should occupy. Living beings, on the other hand, have agency to move in any way they deem favourable and are seemingly not bound by simple mathematical equations. However, we still observe collective behaviour across all scales of life, as exemplified in fig. 2.1, not unlike how molecules can condense to form liquid crystals. There is an ongoing effort to classify such collective systems in a physics framework as a type of *soft condensed matter*, and to construct synthetic systems mimicking these biological phenomena.

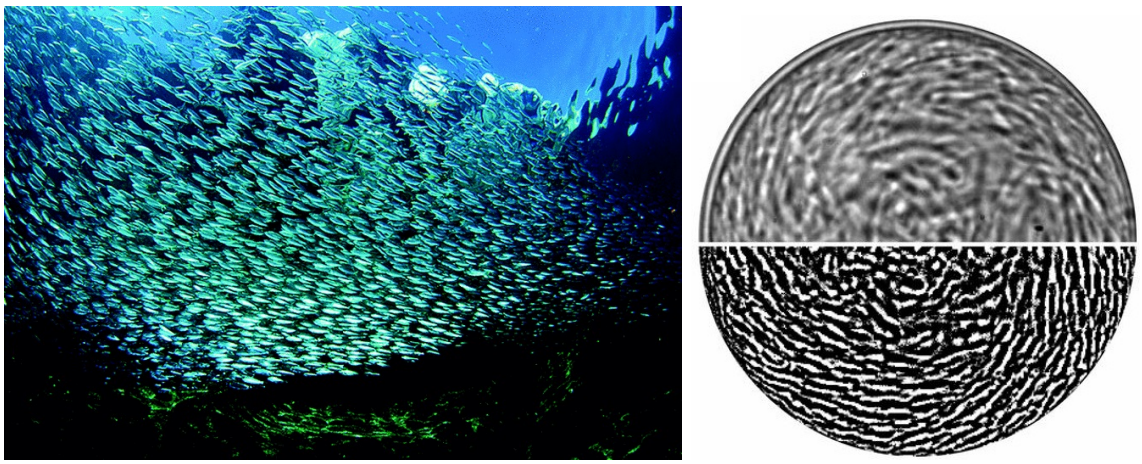

(a) **(b)**

Figure 2.1: *Biological active matter* phenomena at different scales. **(a)** shows a school of sardines, all orientationally aligned (reused from [1]). **(b)** shows a rotating spiral-vortex state of confined *Bacillus subtilis* bacteria, with the upper part being a bright field image and the lower part using edge-detection filtering (reused from [2])

The field of soft condensed matter physics distinguishes itself from traditional solid state physics in that it emphasises the qualities of mutability and responsiveness of the material to changes in its surroundings[3]. The general objective of solid state physics, to understand the macroscopic properties of solids from a microscopic picture, might seem like an impossible many-body problem, but by leveraging the crystalline symmetries that the solids display, microscopic models can be solved[4]. Soft condensed matter does not tend to have strong crystalline symmetry and is often manifested as a *colloidal dispersion*, meaning a suspension of particles in a solvent. The trade-off from these less sharply defined properties is that the material is more easily deformed, resulting in interesting phase diagrams and dynamics. In a biological context, it is then clear why collectively moving animals can also be characterized as "soft", as, for example, the fish in fig. 2.1a depend on their ability to react quickly to avoid obstacles and predators.

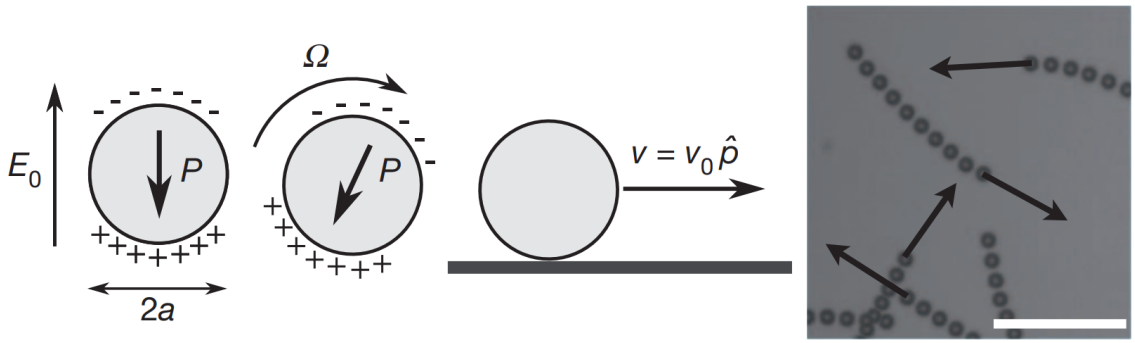

Figure 2.2: An example of *synthetic active matter*: Quincke rollers. The polarized particles roll around in random directions, as shown in the superimposed image on the right of successive snapshots. Time interval, 5.6 ms; scale bar, 50 µm. Reused from [5].

An interesting class of soft matter is therefore *active matter*: systems composed of a large number of self-propelled units which convert stored or ambient free energy into systematic movement[1]. This very general definition ends up describing a wide variety of different systems, including the previously discussed examples of *biological active matter*. Active particles generally have some anisotropy, which determines their direction of self-propulsion. This makes orientational order of the particles a running theme in studies of active matter.

A simple type of *synthetic active matter* that has received some attention in recent years are systems consisting of Quincke rollers[6]. This is a colloidal suspension of insulating spheres in a conducting fluid, which when exposed to an external electric field will have electric dipole moments induced in the spherical particles. This turns out to be an unstable configuration for electric fields stronger than some critical value, and the dipole moments of the particles will end up at a random angle with respect to the external field. Therefore, there will be an induced torque and the particles will begin to spontaneously roll along the bottom of their container in a random direction. See fig. 2.2 for an illustration of this phenomena. The dipole moment and the translational velocity due to the rolling is the anisotropy that defines the orientation of the particles, and through electrical and hydrodynamic interactions the particles can align and display macroscopic directed motion[5]. When confined to a circular domain, the rollers will spontaneously form a vortex state[7], much like the bacteria in fig. 2.1b.

While the active Quicke roller system can be replicated in simulations, it is not immediately obvious which of the interactions are responsible for the alignment and resulting macroscopic motion. This motivates a more bottom up approach, where instead of trying to recreate exact experimental conditions one tries to create the most simple model that displays these emergent phases. This was part of the motivation for the Vicsek model[8] discussed in the next chapter, but in our case we will consider pure dipole interactions. This model is essentially a subset of the Quincke model and has previously been explored with respect to the formation and motion of small clusters in [9]. How such a system behaves in bulk and with or without confinement is what we will investigate in this work.

***

The remaining chapters are structured as follows:

- Chapter 3 introduces active matter models via the Vicsek model.
- Chapter 4 discusses dipole interactions in general and derives the equations of motion for active dipolar particles.
- Chapter 5 parametrises the system and describes the numerical simulation method.
- Chapter 6 presents and discusses the simulation results.
- Chapter 7 presents the conclusion.

3 | Active matter models

3.1 Motivation

One of the most fundamental concepts in physics is symmetry, i.e. what is left invariant under different transformations. For example, the basic laws of physics are rotationally invariant, meaning they have no preferred direction. This famously leads to conservation of angular momentum due to Noether's theorem[10], which is the principle that keeps both planets and electrons in orbit. However, at all scales in nature we can observe phenomena that *do* have a preferred direction. Some are easy to explain, like raindrops falling from the sky down to the ground due to the downwards direction of gravity[1], but what is more interesting is systematic movement that is not caused by such an external force, i.e. steady states that break the symmetry of the system.

Examples of such collective motion phenomena include panics in human crowds[11], animal groups like schools of fish and flocks of bird[12], slimes of unicellular organisms like amoebae and bacteria[13], cultures of individual cells[14], and dynamics of actin filaments[15, 16], microtubules and molecular motors[17]. The ubiquity of this phenomenon suggests underlying universal features[18], and attempting to link these living systems to condensed matter physics is one of the main goals of the active matter paradigm. The problem can also be attacked from the opposite direction: studying the emergent statistical and thermodynamic laws governing matter made of self-propelling particles[19]. Understanding active systems would not only help us model such living systems, but also give insight for novel technological advancements, like drug delivery[20] or drone swarms[21, 22].

3.2 Theory

Active matter systems consist of large numbers of individual units (also called agents or particles), which dissipate energy to produce mechanical work. This process is generally irreversible, making active systems break detailed balance at the microscopic level. Breaking detailed balance means that the probability of going from state A to state B is not the same as the probability of going from state B to state A, the reverse. Therefore, active systems can not be described by equilibrium statistical mechanics, but they still share many similarities with equilibrium systems[23]. Like equilibrium systems, active systems can be in different phases depending on an effective temperature and density. For example, similar to the ferromagnetic phase transition from disorder to order in the Ising model, active matter systems can go from a disordered/gas phase to a flocking/polar liquid phase.

Another important concept of equilibrium systems is universality: all "microscopic models" that display the same symmetries and conservation laws should have the same long-distance behaviour[24]. In other words, the details of the mechanics are not important in the big picture. This motivates studying the simplest model that displays a phase transition, also for non equilibrium systems like active matter. A common candidate for the minimal model displaying collective symmetry-breaking motion is the *Vicsek model*, which

[1] On a global scale this system is also rotationally invariant, as rain on the other side of the globe falls in the opposite direction

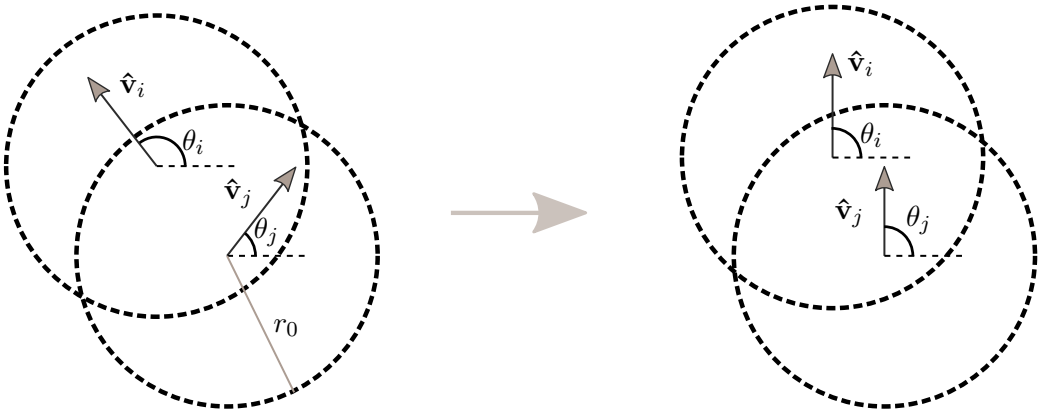

Figure 3.1: Diagram of the average alignment mechanism of the Vicsek model.

will be the focus for the remainder of this chapter.

3.2.1 The Vicsek model

Proposed by T. Vicsek et al.[8] in 1995, the Vicsek model is perhaps the most important model is the field of active matter, both for its simplicity and its interesting consequences. The set up is simple: you have N point particles in a system of dimension $L \times L$. Each particle has position $\mathbf{x}_i$ and velocity $\mathbf{v}_i$, but the absolute velocity is kept constant at v for all particles, so the important parameter is the particle orientation θ_i. Thus, the equation of motion for each particle is simply

$$\mathbf{x_i}(t + \Delta t) = \mathbf{x_i}(t) + \mathbf{v_i}(t)\Delta t = \mathbf{x_i}(t) + v\Delta t\hat{x}\cos\theta_i(t) + v\Delta t\hat{y}\sin\theta_i(t), \tag{3.1}$$

Additionally, at each time step the orientation of each particle is set equal to the average orientation in its neighbourhood (see fig. 3.1 for a two particle scenario), plus a noise term. This is formulated as

$$\theta_i(t + \Delta t) = \langle\theta_j\rangle_{|\mathbf{x_j}-\mathbf{x_i}|<r_0} + \tilde{\eta} \tag{3.2}$$

where $\tilde{\eta}$ is a stochastic variable with a uniform probability distribution in the range $[-\eta, \eta]$[2]. This is where the two competing effects of the system are present: the energy-like particle aligning term and the temperature-like noise term. The radius r_0 defining the particle neighbourhood is set to unity. Changing this will only change the effective size of the system, as the it is the only defining dimension of the otherwise point-like particles. As the average of angles can be somewhat ill-defined, this is usually calculated with complex numbers on the unit circle, with some default behaviour in case the complex numbers sum to zero.

In the limit $v \to 0$ the system is reduced to the familiar XY spin model, and when $v \to \infty$ the particles will always see an average of the whole system, making it a mean-field spin model. At intermediate velocities however, the particles will only interact with their neighbours. The way the speed affects the system is through the natural dimensionless

[2]The range is also commonly defined as $[-\eta/2, \eta/2]$

parameter $C \equiv v\Delta t/r_0$.

Notice that while the "collisions" in this system can be seen as elastic due to the constant v, *conversation of momentum is not observed*. This makes the sum of the velocity vectors a meaningful order parameter of this system, defined as

$$\Pi \equiv \frac{1}{Nv}|\sum_i \mathbf{v_i}|. \tag{3.3}$$

For a disordered gas where there is no orientational correlation Π will go to zero as $\sim 1/\sqrt{N}$, and for a completely ordered system where all the particles are aligned it will approach unity. This is completely analogous to equilibrium spin models, where the order parameter is the magnetization. It is in this order parameter that the phase transitions will present themselves. The important parameters effecting the order of the model are the density $\rho \equiv N/L^2$ and noise amplitude η.

3.2.2 The nature of the phase transition

Vicsek et al. simulated this system with periodic boundary conditions and observed phase transitions from a disordered gas phase to an ordered phase with collective motion in a single direction, meaning the rotational symmetry of eq. (3.1) and eq. (3.2) had been broken. This phase transitions was first seen as a *continuous phase transition*, also called a 2nd order phase transition, as the order parameter appears to remain continuous in the transition, but the derivative of the order parameter does not. This is the case for many equilibrium spin models, including the Ising model for $d \geq 2$ (number of dimensions greater or equal to 2). The system was observed to become ordered at noises below the systems critical noise $\eta_c(\rho)$, or at densities above the density $\rho_c(\eta)$). The system was also observed to be robust to against changes in v over a large range of velocities and showed convergence toward the phase transition in the thermodynamic limit ($N \to \infty$).

The Vicsek model was later the same year shown to be a subset of a larger universality class, namely the Toner and Tu model[25]. This model can be seen as a coarse-grained version of the agent based Vicsek model, as it is a continuum model using velocity and density fields. This model is of theoretical importance, as it was able to analytically show a phase transition for a two dimensional system. In equilibrium statistical mechanics, it is impossible to break a continuous symmetry in dimensions $d \leq 2$ due to the Mermin-Wagner theorem[26], but in this non-equilibrium system we have broken the continuous rotational symmetry.

However, almost 10 years later, the continuous nature of this phase transition was challenged by G. Grégoire and Hugues Chaté[18]. They argued that the class of models including the Vicsek model would always show a *discontinuous phase transition*, also called a 1st order phase transition. This means that the order parameter should display a jump in value at the critical point. The most common example of a discontinuous phase transitions is the liquid-gas transition, where both phases coexist at the critical point. The discontinuous nature of the Vicsek model was argued for by using another parameter, the Binder cumulant $G \equiv 1 - \langle\Pi^4\rangle/3\langle\Pi^2\rangle^2$, which is clearly discontinuous for large N. A modified Vicsek model, where "vectorial noise" proportional to the number of neighbouring particles was used, also displayed much clearer discontinuous jump in the normal order parameter Π.

The reason for the faux apparent continuous phase transition in the Vicsek model are

the strong finite-size effects which are present around the critical point. More precisely, near the critical point of the transition the ordered phase is unstable to a long wavelength instability, with travelling unstable modes $k < k_0$. Therefore, a system with $L < L_0 \sim 1/k_0$ will not be able to support these modes, and the system instead appears as a mix of ordered and unordered phases, causing the continuous behaviour of the order parameter. Indeed, it has been later argued that the phases of the system should not be seen as ordered or disordered, but rather as a disordered gas phase and a polar liquid phase, which can mix[27].

3.3 Vicsek simulation results and discussion

The original Vicsek model was implemented in order to compare its behaviour to the more complex active dipole system later. The number of particle used was $N = 1600$ and the system size was $L = 40$ (periodic boundary conditions and $r_0 = 1$, as usual), resulting in a density $\rho = 1$. The velocity was set to $v = 5$ and $\Delta t = 0.05$, mostly just to be able to animate them in real time. This results in $C = 0.25$, in the same order of magnitude of previous studies[28]. As previously stated, the system is not strongly sensitive to this value.

The order parameter in eq. (3.3) as a function of the noise amplitude η for our system is shown in fig. 3.3. With zero noise, representing a zero temperature, the order goes to unity, and as the noise increases the order drops of until it approaches zero for $\eta \gtrsim 0.4\pi$. $\eta = \pi$ represents the infinite temperature point, as each particle will have completely uncorrelated angles randomly picked in the range $[-\pi, \pi]$.

At this point we can see why this was originally thought to be a continuous phase transition. It is quite similar to the ferromagnetic phase transition of the Ising model, complete with the apparent diverging standard deviation at the critical point. These results are in good agreement with previous studies[28].

The time evolution of the order for 3 different noise levels are shown in fig. 3.4, with snapshots of the end states shown in fig. 3.2a, fig. 3.2b and fig. 3.2c. The high and low order states both show little variance in their orders, but at the critical point the order is distributed over a large range of values. The distribution also seems to be bimodal, as it seems to jump between a higher order level of $\Pi \sim 0.5$ and a lower order level of $\Pi \sim 0.2$. For a continuous phase distribution we should expect the distribution to be unimodal, though this sample might not be over a long enough time scale to determine it's character one way or another. Nevertheless, the bimodal distribution of the order near the critical point was one of the arguments used by Grégoire and Chaté in [18] to establish the discontinuous nature of this phase transition.

The snapshots show the position and orientation of the particles at different noise levels. In addition to the arrows, the colour of the particles also show the orientation of each particle according to fig. 3.2d. Figure 3.2a show a clear collective motion in the positive x direction, made clear by the uniform colouring of the particles. Different runs with the same parameter values will result in different, arbitrary global orientation, all depending on the initial particle positions, orientations, and the stochastic noise term.

Figure 3.2b shows some correlated orientation over small distances, but it overall still unordered. This is consistent with the view of a polar liquid phase mixed with an unordered gaseous background. A pure gaseous phase is clearly shown in fig. 3.2c, where there is no correlation between the particles.

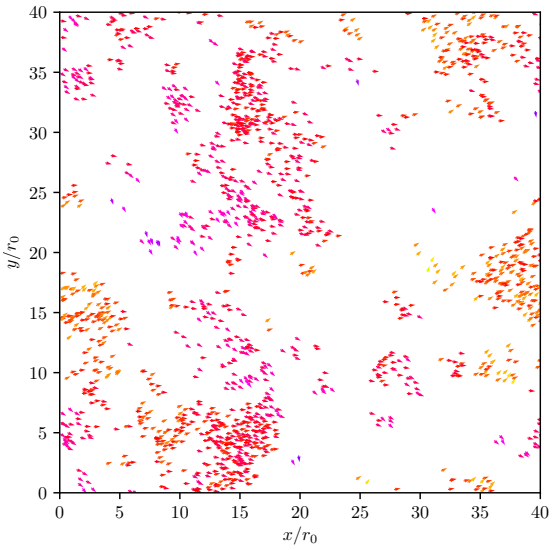

(a) Noise amplitude $\eta = 0.1\pi$, polar liquid phase.

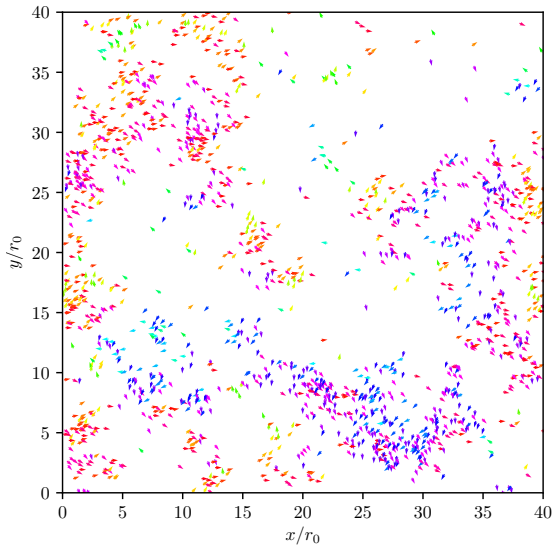

(b) $\eta = 0.32\pi$, critical phase.

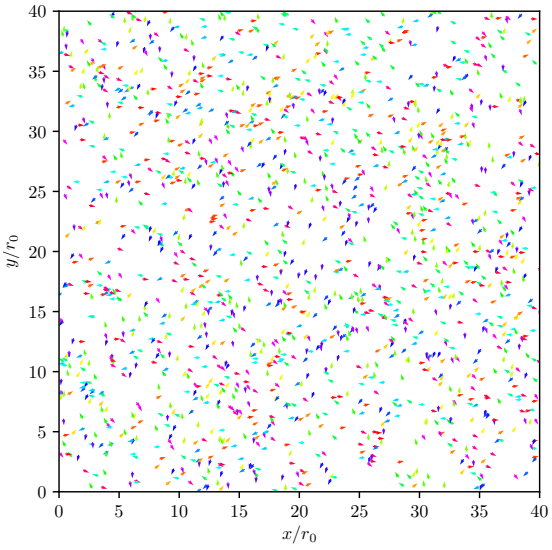

(c) $\eta = 0.72\pi$, gaseous phase.

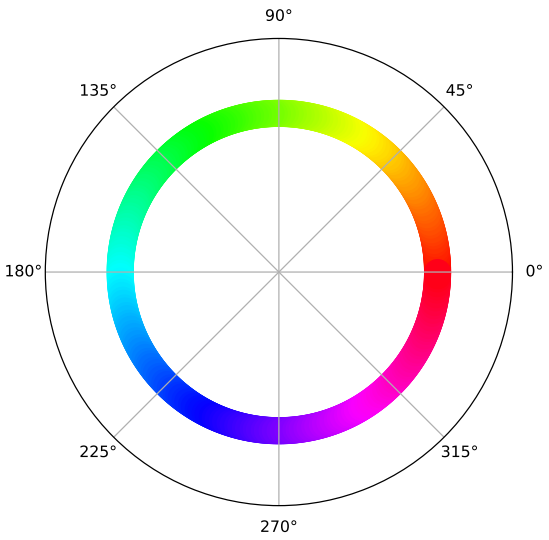

(d) Orientational colour mapping.

Figure 3.2: Snapshots of **(a)** an ordered state, noise amplitude $\eta = 0.1\pi$ and density $\rho = 1$, **(b)** a system near the critical point, $\eta = 0.32\pi$, $\rho = 1$ and **(c)** an unordered state, $\eta = 0.72\pi$, $\rho = 1$. **(d)** shows what orientation the particle colours correspond to.

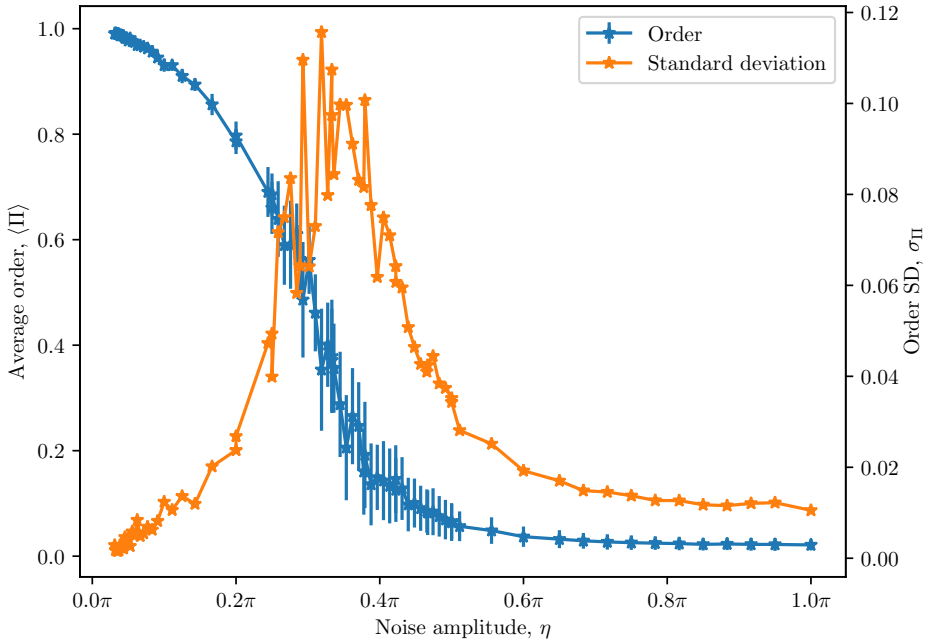

Figure 3.3: The order parameter Π (left axis) and its standard deviation σ_Π(left axis) as a function of the noise amplitude η. The order fluctuations are largest around the critical point $\eta_c \sim 0.35\pi$. Density $\rho = 1$, number of particles $N = 1600$.

The conclusion we can draw from the Vicsek model is that short-range interactions between active particles can lead to global collective motion. The question then remains if dipole interactions can fill this role. Though they can not be described as short-ranged, they are much less explicitly aligning than the interactions described by eq. (3.2). The details of these interactions are covered in the following chapter.

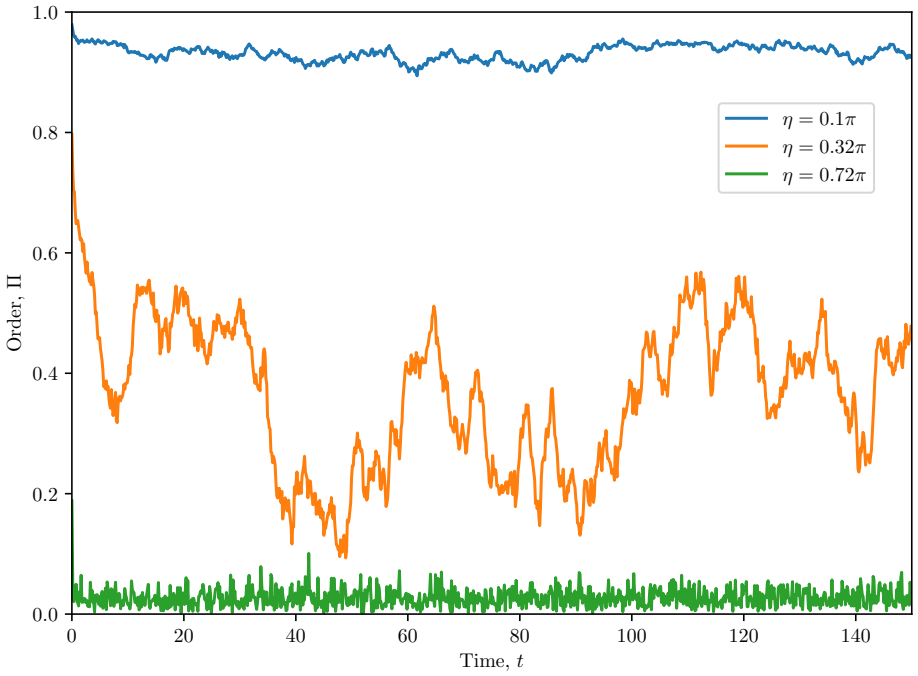

Figure 3.4: The evolution of the order parameter over time for different noise levels: a highly ordered phase (blue), a wildly fluctuating critical phase (orange) and a disordered phase (green). Snapshots of the end states are shown in fig. 3.2a, fig. 3.2b and fig. 3.2c.

4 | Equations of motion for dipole-dipole interaction

This chapter derives the equations of motion for a collection of dipoles, starting with the basic theory of electrostatics. The details of this derivation (4.2) are represented in full, as it provides helpful intuition for interpreting the simulation results and motivates the additional choice of a repulsive potential (4.3). The equations of motion are finalized with the addition of a self-propelling force and rotational diffusion, resulting in *active Brownian dynamics* (4.4). Finally, we describe the possible wall interactions for confined systems, which in our case will be either secularly reflective or normally repulsive (4.5).

4.1 Introducing dipoles

Dipoles are absolutely fundamental both for how particles are ordered in solid matter and how electric and magnetic fields interact with it. For electric fields, the concept of dipoles is introduced as charges of equal magnitude but opposite signs ($\pm q$) separated by a displacement vector $\mathbf{d}$, as sketched in fig. 4.1a. The central question to answer is how such a configuration behaves in the limit where the distance between the charges goes to zero with respect to the distance at which the dipole is observed. The naive approach to this would be to treat such a charge configuration as if there was zero charge present, as the charges would seem to completely overlap and sum to zero. The field produced by the dipole would indeed be dominated by the usual $1/r^2$ behavior seen in monopoles, but in fact the field decays as $1/r^3$, only an order faster. This is shown later in eq. (4.3).

However, an electric dipole is more than just a "weakened" charge, it has a defined orientation: the displacement vector $\mathbf{d}$ from the negative charge to the positive charge and its associated proportional dipole moment $\mathbf{p}$. The departure from the $SO(3)$ symmetry of the lone point charge lets the interaction between two dipoles depend on not only the distance between them, but possibly also their orientation with respect to each other. This is the first hint that dipole-dipole interactions can possibly be used as an alignment mechanism for active matter.

Dipoles are, however, not a phenomena exclusive to electric fields. Amazingly, a small current loop will produce a magnetic field that is asymptotically equivalent to the electric field produced by an electric dipole. The dynamics of the two seemingly disparate physical phenomena will be identical if one exchanges the dipole moments $\mathbf{p} \leftrightarrow \mathbf{m}$, the dimensional physical constants $1/\epsilon_0 \leftrightarrow \mu_0$ and associated fields $\mathbf{E} \leftrightarrow \mathbf{B}$. One might be tempted to interpret these magnetic dipoles as a combination of two supposedly separate magnetic monopoles, one being the "north pole" and the other being the "south pole", as seen in fig. 4.1b. This is the *Gilbert model* and gives a clear intuition of the vector size $\mathbf{m}$, which would be proportional to the the displacement vector $\mathbf{d}$ from the south pole to the north pole. This direct analogy from electric dipoles to magnetic dipoles unfortunately falls quickly apart on inspection, as *single magnetic monopoles do not exist* as far as modern physics is concerned[29]. This difference is seen in Maxwell's equations, as $\nabla \cdot \mathbf{E} = \rho/\epsilon_0$, but $\nabla \cdot \mathbf{B} = 0$, telling us that the "magnetic charge density" ρ_m will always be 0.

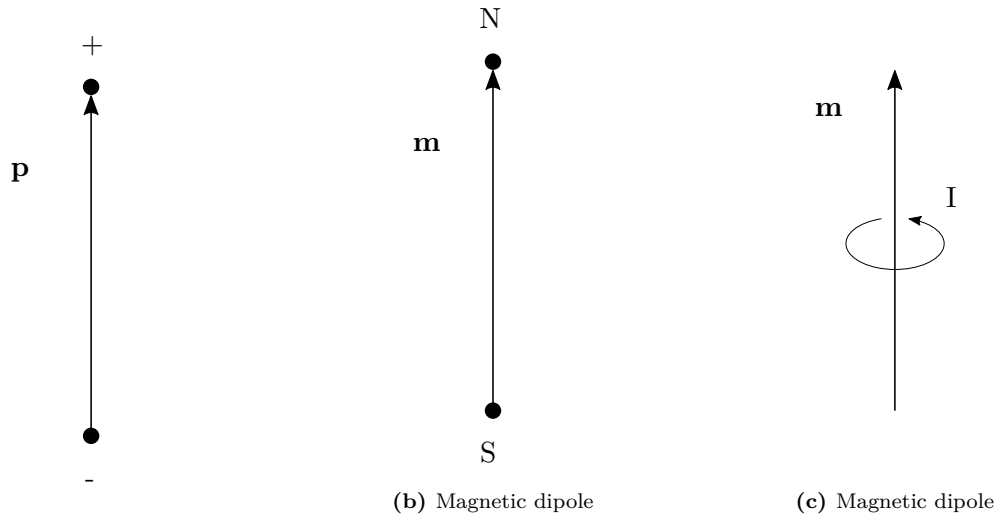

(a) Electric dipole

(b) Magnetic dipole (Gilbert model)

(c) Magnetic dipole (Ampère model)

Figure 4.1: Different models for the physical origin of electric and magnetic dipoles.

A more correct way to interpret magnetic dipoles is therefore simply as small circular currents. In this view the magnetic dipole moment **m** is oriented relative to the current loop **I** by a "right-hand rule", as shown in fig. 4.1c. This is the *Ampère model*, and holds up until one considers that subatomic particles like electrons and protons also have an associated magnetic dipole moment without having any sort of current loop. One might be fooled into imagining this as the particle rotating on it's own axis, but it would be impossible to distinguish a "rotating" spherically symmetric identical particle from its non-rotating counterpart unless one opens up for there being some intrinsic vector quantity present. There actually turns out to be such an intrinsic vector associated with each particle called *spin*, but this is entirely quantum mechanical and can not be simply interpreted as rotation about its own axis.

The actual source of the dipole potential, whether it is electric, magnetic or quantum mechanical, is of course relevant for designing physical experiments, but the fact that the equations of motion end up being invariant to an exchange in the dimensional physical constants motivates an investigation purely into the dynamics of the dipole-dipole interactions. A dipole potential is perhaps *the most fundamental anisotropic potential in all of physics*, so understanding how an ensemble of dipoles interact is essential for any theory of symmetry breaking active particles. Therefore, without loss of generality, in this work we follow the formalism of electric dipoles, as it is more intuitive to imagine separated charges than current loops.

4.1.1 Examples of dipoles in active matter

In physical experiments, it is often simpler to deal with magnetic fields, as they interact with fewer materials than electric fields (materials are much more likely to be conductive or dielectric than magnetic). In my master's project last semester we created magnetic dipoles in the form of "magnetic holes", which are non-magnetic particles suspended in a

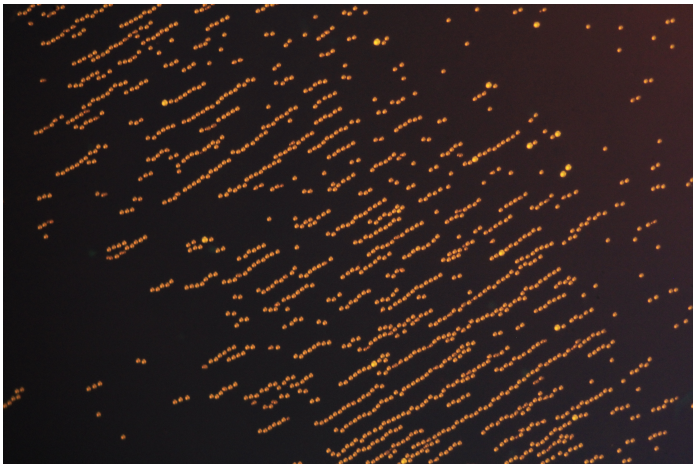

Figure 4.2: "Magnetic holes" aligned into particle chains by an in-plane external magnetic field. The particles are non-magnetic spheres with diameter 40 µm, but they are suspended in a ferrofluid. Own work from last year's master's project.

ferrofluid[30]. When exposed to an external magnetic field these particles will interact as dipoles, leading to the chain formations shown in fig. 4.2 for an external field parallel to the plane of the system. This attraction will be explained as we derive the properties of dipole-dipole interactions.

However, to have interesting applications in active matter the dipole moment should be intrinsic to each particle and not directly linked to an external field, and, of course, the particles need to have a source of self-propulsion. The most commonly discussed implementation of active dipoles are therefore half-capped "Janus particles" embedded with permanent magnetic dipoles, which are driven catalytically or by thermophoresis[31].

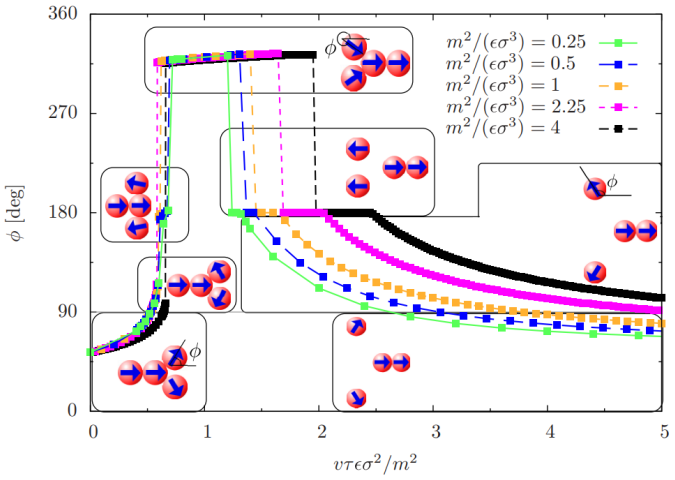

Figure 4.3: Evolution of an active dipole "Y junction" as the self-propulsion speed is increased. Different series are for different dipole strengths. Reused from [9]

A. Kaiser et al. have performed simulations of active dipoles for up to $N = 5$ particles, which show complex cluster dynamics depending on the self-propulsion speed v and the dipole strength m. The evolution of a four-particle cluster is shown in fig. 4.3. The non-trivial interactions these active dipoles display further motivates simulations with larger particle numbers.

Additionally, dipole potentials show up in more than just electromagnetism. The velocity field of a particle moving in a fluid can also be modelled as a dipole field, and such interactions are quite well studied for active matter systems[5, 7, 32]. This study will not model the hydrodynamics beyond each particle having a constant mobility, but it is important to note that dipole interactions are present in essentially all of confined colloidal active matter.

4.2 Dipolar forces and torques

We start by looking at two point charges, $+q$ and $-q$ separated by the displacement vector $\mathbf{d}$ from negative to positive. Using Coulomb's law and the superposition principle the total field for a dipole situated at the origin is

$$\mathbf{E}(\mathbf{r}) = \frac{1}{4\pi\epsilon_0}\left[\frac{+q(\mathbf{r}-\mathbf{d}/2)}{|\mathbf{r}-\mathbf{d}/2|^3} + \frac{-q(\mathbf{r}+\mathbf{d}/2)}{|\mathbf{r}+\mathbf{d}/2|^3}\right]. \tag{4.1}$$

This is the exact field generated, but it's more sensible to consider the case where $|\mathbf{d}| \ll |\mathbf{r}|$. Using the series expansion $1/(1+x)^{3/2} = 1 - 3x/2 + 15x^2/8 - ...$ we have for each charge

$$\begin{aligned}\mathbf{E}_{\pm}(\mathbf{r}) &= \frac{1}{4\pi\epsilon_0}\frac{\pm q(\mathbf{r}\mp\mathbf{d}/2)}{r^3}\left[\frac{1}{\left(1\mp\frac{\mathbf{d}\cdot\mathbf{r}}{r^2}+\frac{d^2}{4r^2}\right)^{3/2}}\right] \\ &= \frac{1}{4\pi\epsilon_0}\frac{\pm q(\mathbf{r}\mp\mathbf{d}/2)}{r^3}\left[1 - \frac{3}{2}\left(\frac{d^2}{4r^2}\mp\frac{\mathbf{d}\cdot\mathbf{r}}{r^2}\right) + \frac{15}{8}\left(\frac{d^2}{4r^2}\mp\frac{\mathbf{d}\cdot\mathbf{r}}{r^2}\right)^2 - ...\right].\end{aligned} \tag{4.2}$$

Now adding together the two contributions and focusing on the leading order terms of d/r gives

$$\begin{aligned}\mathbf{E}_{dip}(\mathbf{r}) &= \mathbf{E}_+(\mathbf{r}) + \mathbf{E}_-(\mathbf{r}) \\ &= \frac{1}{4\pi\epsilon_0}\frac{q}{r^3}\left[\mathbf{r}\left(3\frac{\mathbf{d}\cdot\mathbf{r}}{r^2} + \mathcal{O}((d/r)^3)\right) - \mathbf{d}\left(1+\mathcal{O}((d/r)^2)\right)\right] \\ &\approx \frac{1}{4\pi\epsilon_0}\frac{1}{r^3}\left[3(q\mathbf{d}\cdot\hat{\mathbf{r}})\hat{\mathbf{r}} - q\mathbf{d}\right].\end{aligned} \tag{4.3}$$

As we see from eq. (4.3), the expression for the electric dipole field is quite clean and simple to a leading order. The terms that completely characterize a dipole, the charge magnitude q of each monopole and their separation vector $\mathbf{d}$, always come together as a product. This motivates defining a new vector quantity $\mathbf{p} = q\mathbf{d}$, which is the electric dipole

moment mentioned in section 4.1. The expression for the electric field $\mathbf{E}_j$ at coordinate $\mathbf{r}_i$ produced by dipole j with dipole moment $\mathbf{p}_j$ then becomes

$$\mathbf{E}_{j,dip}(\mathbf{r}_i) = \frac{1}{4\pi\epsilon_0}\frac{1}{r_{ij}^3}\left[3(\mathbf{p}_j \cdot \hat{\mathbf{r}}_{ij})\hat{\mathbf{r}}_{ij} - \mathbf{p}_j\right], \tag{4.4}$$

where $\mathbf{r}_{ij}$ is the displacement vector from dipole j to coordinate $\mathbf{r}_i$, or simply $\mathbf{r}_{ij} = \mathbf{r}_i - \mathbf{r}_j$. An example of the field lines produced by two dipoles is shown in fig. 4.4.

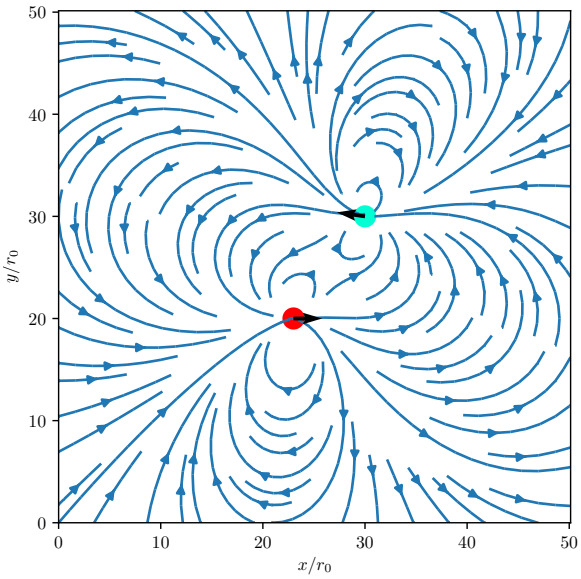

Figure 4.4: Field lines produced by two dipoles of equal strength. The arrow on each particle shows its orientation $\hat{\mathbf{p}}$.

This is the field produced by a dipole, but how it the dipole itself affected by external electric fields? For a *constant* field, the positive charge q_+ will experience a force $\mathbf{F}_+ = q\mathbf{E}$ and the negative charge q_- will experience a force $\mathbf{F}_- = -q\mathbf{E}$, so that $\mathbf{F}_{tot} = \mathbf{F}_+ + \mathbf{F}_- = \mathbf{0}$. While the net force is zero, the dipole can still experience a non-zero torque. Each charge will experience a torque $\mathbf{N}_\pm = (\pm\frac{1}{2}\mathbf{d}) \times (\pm q\mathbf{E}) = \frac{1}{2}\mathbf{p} \times \mathbf{E}$, making the total torque simply $\mathbf{N}_{tot} = \mathbf{p} \times \mathbf{E}$[1].

The important result here is that a dipole j will exert a non-zero torque in a neighbouring dipole i as long as $\mathbf{p}_i$ is not parallel to the field at its coordinate, $\mathbf{E}_j(\mathbf{r}_i)$. In other words, the dipole will be forced to align with the local $\mathbf{E}$ field. For a collection of dipoles we use Einstein summation convention, where we imply summation over the index j, but excluding the absurd $i = j$ "self-torque" case:

$$\mathbf{N}_{i,dip} = \mathbf{p}_i \times \mathbf{E}_{j,dip}(\mathbf{r}_i) = \frac{1}{4\pi\epsilon_0}\frac{p_i p_j}{r_{ij}^3}\left[3(\hat{\mathbf{p}}_j \cdot \hat{\mathbf{r}}_{ij})(\hat{\mathbf{p}}_i \times \hat{\mathbf{r}}_{ij}) - (\hat{\mathbf{p}}_i \times \hat{\mathbf{p}}_j)\right] \tag{4.5}$$

Equation (4.5) is all we need to calculate the alignment interaction for a collection of dipoles, but if we only considered the torque we would be neglecting an essential component

[1] We're using $\mathbf{N}$ instead of the more usual τ because the latter will be used as the time unit in section 5.1.

of dipole-dipole interactions. While we have seen that a *constant* field will not induce a net-force on a dipole, what happens if the field is not constant? The sum of forces for a dipole located at $\mathbf{r}_i$ $\mathbf{F}_{tot} = \mathbf{F}_+ + \mathbf{F}_- = q\mathbf{E}(\mathbf{r}_i + \mathbf{d}_i/2) - q\mathbf{E}(\mathbf{r}_i - \mathbf{d}_i/2)$. Assuming again that $\mathbf{d}$ is small, we linearise the field around $\mathbf{r}_i$, so that the force on dipole i from dipole j becomes

$$\begin{aligned}\mathbf{F}_i &= q(\mathbf{d}_i \cdot \boldsymbol{\nabla}(E_{x,i}(\mathbf{r}_i) + E_{y,i}(\mathbf{r}_i) + E_{z,i}(\mathbf{r}_i))) \\ &= \mathbf{p}_i \cdot \boldsymbol{\nabla}(E_{x,i}(\mathbf{r}_i) + E_{y,i}(\mathbf{r}_i) + E_{z,i}(\mathbf{r}_i)) \\ &= (\mathbf{p}_i \cdot \boldsymbol{\nabla})\mathbf{E}_j(\mathbf{r}_i) \\ &= \boldsymbol{\nabla}(\mathbf{p}_i \cdot \mathbf{E}_j(\mathbf{r}_i)).\end{aligned} \tag{4.6}$$

The last line is true in our case because $\mathbf{p}_i$ is constant in space for each dipole, but in general where $\mathbf{p}$ can be a function of $\mathbf{r}$ we would need to stick with $(\mathbf{p}_i \cdot \boldsymbol{\nabla})\mathbf{E}_j(\mathbf{r}_i)$.

A useful result from eq. (4.6) is that we can use the gradient theorem to find the work done when moving a dipole from $\mathbf{r} \to \infty$ to $\mathbf{r}_i$, which is a measure of the potential energy a dipole has in an external field. The expression is simply

$$\begin{aligned}U(\mathbf{r}_i) &= -\int_{\infty}^{\mathbf{r}_i} \boldsymbol{\nabla}(\mathbf{p}_i \cdot \mathbf{E}_j(\mathbf{r})) \cdot d\mathbf{r} \\ &= \mathbf{p}_i \cdot \underbrace{\mathbf{E}_j(\infty)}_{\to 0} - \mathbf{p}_i \cdot \mathbf{E}_j(\mathbf{r}_i) \\ &= -\mathbf{p}_i \cdot \mathbf{E}_j(\mathbf{r}_i),\end{aligned} \tag{4.7}$$

where we have assumed the external field vanishes at infinity, which is the case for dipoles as shown in eq. (4.4). This result agrees with the expression for torque eq. (4.5), as the energy in eq. (4.7) is minimized when $\mathbf{p}_i \parallel \mathbf{E}_j(\mathbf{r}_i)$, which is the state the torque will force the dipole into.

So to find the dipole-dipole force we only need to insert eq. (4.4) into eq. (4.6). The two results needed to do this are the identities $\boldsymbol{\nabla}\frac{1}{r^n} = -\frac{n\mathbf{r}}{r^{n+2}}$ and $\boldsymbol{\nabla}(\mathbf{v_1} \cdot \mathbf{r}) = \mathbf{v_1}$, courtesy of [33]. Working it out then gives

$$\begin{aligned}\mathbf{F}_{i,dip} &= \boldsymbol{\nabla}\left(\frac{1}{4\pi\epsilon_0}\frac{1}{r_{ij}^3}\left[3(\mathbf{p}_j \cdot \hat{\mathbf{r}}_{ij})(\mathbf{p}_i \cdot \hat{\mathbf{r}}_{ij}) - (\mathbf{p}_i \cdot \mathbf{p}_j)\right]\right) \\ &= \frac{1}{4\pi\epsilon_0}\boldsymbol{\nabla}\left(\frac{3(\mathbf{p}_j \cdot \mathbf{r}_{ij})(\mathbf{p}_i \cdot \mathbf{r}_{ij})}{r_{ij}^5} - \frac{(\mathbf{p}_i \cdot \mathbf{p}_j)}{r_{ij}^3}\right) \\ &= \frac{1}{4\pi\epsilon_0}\left(\frac{3(\mathbf{p}_i \cdot \mathbf{r}_{ij})}{r_{ij}^5}\boldsymbol{\nabla}(\mathbf{p}_j \cdot \mathbf{r}_{ij}) + \frac{3(\mathbf{p}_j \cdot \mathbf{r}_{ij})}{r_{ij}^5}\boldsymbol{\nabla}(\mathbf{p}_i \cdot \mathbf{r}_{ij})\right. \\ &\qquad \left. +3(\mathbf{p}_j \cdot \mathbf{r}_{ij})(\mathbf{p}_i \cdot \mathbf{r}_{ij})\boldsymbol{\nabla}\frac{1}{r_{ij}^5} - (\mathbf{p}_i \cdot \mathbf{p}_j)\boldsymbol{\nabla}\frac{1}{r_{ij}^3}\right) \\ &= \frac{3p_ip_j}{4\pi\epsilon_0}\frac{1}{r_{ij}^4}\left[(\hat{\mathbf{p}}_i \cdot \hat{\mathbf{p}}_j)\hat{\mathbf{r}}_{ij} + (\hat{\mathbf{r}}_{ij} \cdot \hat{\mathbf{p}}_j)\hat{\mathbf{p}}_i + (\hat{\mathbf{r}}_{ij} \cdot \hat{\mathbf{p}}_i)\hat{\mathbf{p}}_j - 5(\hat{\mathbf{r}}_{ij} \cdot \hat{\mathbf{p}}_i)(\hat{\mathbf{r}}_{ij} \cdot \hat{\mathbf{p}}_j)\hat{\mathbf{r}}_{ij}\right].\end{aligned} \tag{4.8}$$

Equation (4.8) shows that the force between two dipoles depends quite strongly on their relative orientation, making the interaction *attractive* when the dipoles are stacked along their orientation ($(\hat{\mathbf{r}}_{ij}\cdot\hat{\mathbf{p}}_i)(\hat{\mathbf{r}}_{ij}\cdot\hat{\mathbf{p}}_j) = 1$) and *repulsive* when side by side ($(\hat{\mathbf{r}}_{ij}\cdot\hat{\mathbf{p}}_i) = (\hat{\mathbf{r}}_{ij}\cdot\hat{\mathbf{p}}_j) = 0$). In both cases the interaction decays as $1/r^4$, making the translational interaction an order weaker than the rotational interaction from the torque.

This concludes the description of interaction between electrical dipoles, but, as stated in section 4.1, magnetic dipoles will interact in the exact same way if one exchanges $\mathbf{p} \leftrightarrow \mathbf{m}$, $1/\epsilon_0 \leftrightarrow \mu_0$ and $\mathbf{E} \leftrightarrow \mathbf{B}$. This derivation is left out for brevity here, but can be seen in [29] or [33, 34]. The gist is that one studies small, circular current loops, where their interaction is derived using the magnetic Lorentz force $F = q\mathbf{v} \times \mathbf{B}$. The expression corresponding to $\mathbf{p} = q\mathbf{d}$ turns out to be $\mathbf{m} = IA\hat{\mathbf{n}}$, with I being the current, A the area enclosed by the loop and $\hat{\mathbf{n}}$ the normal vector of the loop using the right-hand rule mentioned in section 4.1.

In the actual calculations, we will rescale the physical units so that the vacuum permittivity ϵ_0 is set to unity, making eq. (4.4) and eq. (4.8) equivalent in a similar case where the units are instead rescaled so that the vacuum permeability μ_0 is unity. The actual rescalings from the SI system will be different in these two cases, but the physics will be the same. So while the results following results will be valid for magnetic dipoles, we will still use the labels $\mathbf{E}$ and $\mathbf{p}$ for this generalised field and dipole moment.

4.3 The repulsive potential

The evolution of a system of dipoles is indeed fully described by the equations in section 4.2, but a simulation using only those rules will end up having issues with the attractive aspect of eq. (4.8). Nothing stops attracting dipoles from becoming arbitrarily close to each other, causing the simulation to need a progressively smaller time step to remain stable, but also breaking down the $|\mathbf{d}| \ll |\mathbf{r}|$ assumption used to derive eq. (4.4). Clearly, an additional repulsive potential is needed.

A hard sphere potential is one way to solve this, meaning that the particles are forbidden to get any closer than some limit σ to each other by an infinite potential for $r < \sigma$ and $U = 0$ otherwise. However, this makes any sort of compression impossible and can be numerically troublesome for densly packed structures. Instead one can use a soft potential that gradually becomes more repulsive as the particles approach each other. The regular prescription for this is to use a truncated *Lennard-Jones potential*. The original Lennard-Jones potential[35] is written as

$$U_{LJ}(r) = 4\epsilon\left[\left(\frac{\sigma}{r}\right)^{12} - \left(\frac{\sigma}{r}\right)^{6}\right] \tag{4.9}$$

where there is a $1/r^6$ attractive component inspired by van der Waals forces and a $1/r^{12}$ repulsive component, which is just a numerically convenient choice of a strong repulsion, ultimately due to Pauli repulsion. The potential is fully described by two parameters: the depth of the potential well ϵ and the distance at with the potential equals zero σ. This potential is shown in 4.5a.

However, we are not interested in the attractive component, only the repulsive part. This is why we truncate the Lennard-Jones potential, so that only the initial repulsive

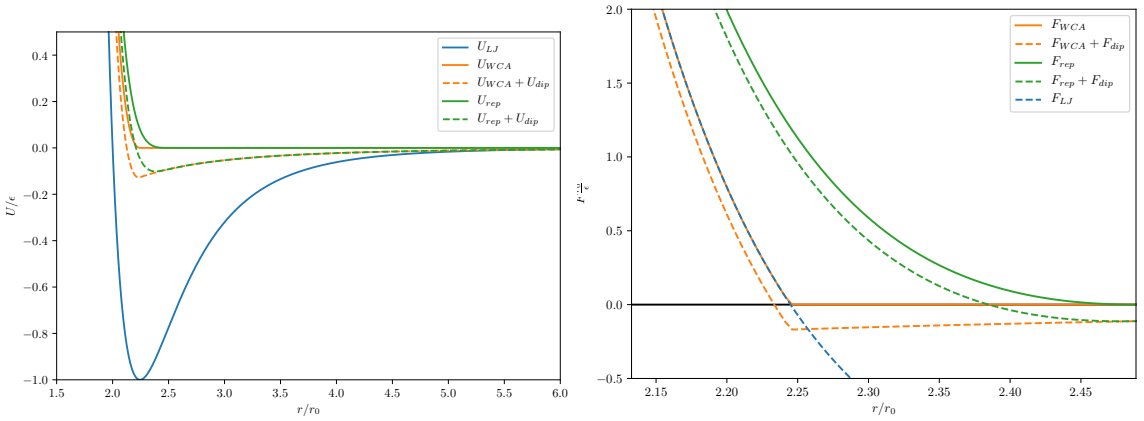

(a) Potentials in units of ϵ.

(b) Radial component of force in units of ϵ/r_0.

Figure 4.5: Lennard-Jones (LJ), Weeks-Chandler-Andersen (WCA) and the eq. (4.11) potential. $\sigma = 2r_0$ and r_0 is set to unity (essentially the radius of the dipole particles). The purely repulsive potentials have also been plotted along with a dipole potential with $(\hat{\mathbf{r}}_{ij} \cdot \hat{\mathbf{p}}_i)(\hat{\mathbf{r}}_{ij} \cdot \hat{\mathbf{p}}_j) = 1$ (purely attractive) and $|\mathbf{p}| = 3\sqrt{\epsilon_0 \epsilon r_0^3}$ (the value used in the simulations).

section is preset. This is called a *Weeks-Chandler-Andersen* potential[36] and is expressed as

$$U_{WCA}(r) = \begin{cases} 4\epsilon \left[\left(\frac{\sigma}{r}\right)^{12} - \left(\frac{\sigma}{r}\right)^{6} \right] + \epsilon, & r \leq r_c \\ 0, & r > r_c, \end{cases} \tag{4.10}$$

where $r_c = 2^{1/6}\sigma \approx 1.12\sigma$, the distance where $\frac{\partial}{\partial r} U_{LJ}(r_c) = 0$, making the force continuous at r_c. However, is this study we decided to also ensure the force also was *differentiable* at the cut-off distance r_c. In other words we need $\frac{\partial^2}{\partial r^2} U_{LJ}(r_c) = \frac{\partial}{\partial r} U_{LJ}(r_c) = 0$, which can be done by introducing a linear term into U_{WCA}. The potential ends up having the expression

$$U_{rep}(r) = \begin{cases} 4\epsilon \left[\left(\frac{\sigma}{r}\right)^{12} - \left(\frac{\sigma}{r}\right)^{6} \right] - f_s r + \epsilon_s, & r \leq r_c \\ 0, & r > r_c, \end{cases} \tag{4.11}$$

with a new cut-off distance $r_c = (26/7)^{1/6}\,\sigma \approx 1.24\sigma$, a potential shift $\epsilon_s = 49/13\epsilon \approx 3.77\epsilon$ and a force shift $f_s = \frac{252}{169} 2^{5/6} \sqrt[6]{7/13} \frac{\epsilon}{\sigma} \approx 2.40 \frac{\epsilon}{\sigma}$. The force resulting from this potential is then

$$\mathbf{F}_{rep}(r) = \begin{cases} 4\epsilon \left[\frac{12}{r} \left(\frac{\sigma}{r}\right)^{12} - \frac{6}{r} \left(\frac{\sigma}{r}\right)^{6} \right] \hat{\mathbf{r}} + f_s \hat{\mathbf{r}}, & r \leq r_c \\ 0, & r > r_c. \end{cases} \tag{4.12}$$

This might seem quite convoluted due to the numerical factors in the constants, but it will not be any more costly to integrate numerically. See fig. 4.5 for a comparison with the usual WCA potential.

The motivation for using this modified potential was to make the repulsive potential softer, to hopefully encourage more stable simulations. As shown in fig. 4.5b (where we

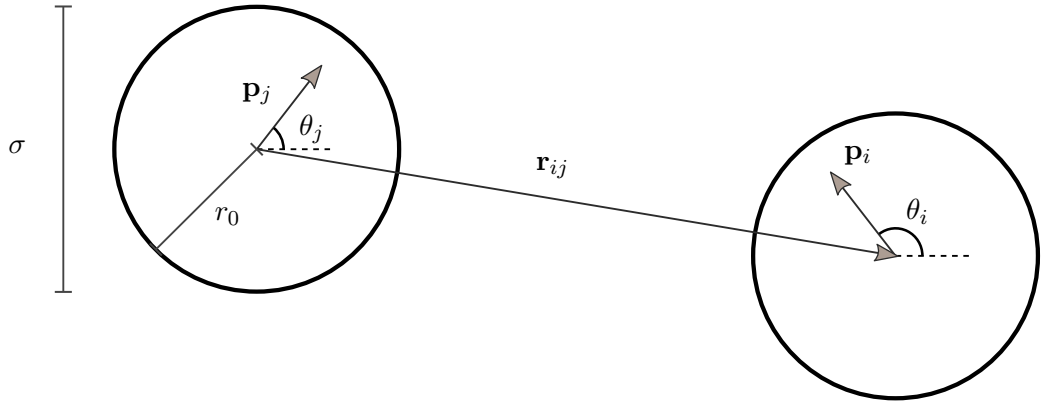

Figure 4.6: Diagram of the scalar and vector quantities associated with the dipole particles.

use the same parameter values as in the simulations), when combining a repulsive WCA potential and an attractive dipole potential there in a quite significant kink in the force curve. Having a non differentiable point this close to the attractive minimum (less than $0.02r_0$ away) might cause some strange effects, as the curve around this point determines the expected variance in nearest-neighbour separation, shown as wider peaks in the pair correlation function (i.e. the radial distribution function). In comparison, the potential with the added linear term has a defined 2nd derivative in all points, but the attractive minimum is quite a bit further out than for the LJ potential ($1.19\sigma = 2.38r_0$ for the values used in fig. 4.5) and the potential is less convex at that point. Thus we should expect wider peaks in the pair correlation and more distance between them compared to a LJ potential with the same σ.

4.4 Active Brownian dynamics

All the equations so far have been completely deterministic, giving us the system of partial differential equations

$$m\frac{\partial^2 \mathbf{x}_i}{\partial t^2} = \mathbf{F}_{i,dip}(\mathbf{r}_{ij}; \mathbf{p}_i, \mathbf{p}_j) + \mathbf{F}_{rep}(\mathbf{r}_{ij}) \tag{4.13}$$

and, restricting the particles and their dipole moments to a plane,

$$I\frac{\partial^2 \theta_i}{\partial t^2} = (\mathbf{p}_i \times \mathbf{E}_{j,dip}(\mathbf{r}_{ij}; \mathbf{p}_i, \mathbf{p}_j)) \cdot \hat{\mathbf{n}}, \tag{4.14}$$

with summation over all $j \neq i$ still implied. m is the mass off the dipole particle, I is its moment of inertia and θ is the angle the dipole moment has in the plane, see fig. 4.6. $\hat{\mathbf{n}}$ is simply the normal vector of the plane, as rotations will only occur around this axis.

In order to make these particles *active* we will now introduce a self-propelling force $\mathbf{F}_a$, which will be constant and always directed along $\hat{\mathbf{p}}_i$. Since these forces do *not* originate from another particle in the system, these forces will be able to do some net work on the system. This makes this a *non-equilibrium system*, as energy is constantly pouring into

the system to make the particles self-propel. We are not interested in the specific physical origin of the self-propelling force in this case, but keeping it aligned to the dipole moment will mimic the typical hydrodynamic potential caused by moving particles in a confined solution[32]. Equation (4.13) then becomes

$$m\frac{\partial^2 \mathbf{x}_i}{\partial t^2} = \mathbf{F}_{i,dip}(\mathbf{r}_{ij};\mathbf{p}_i,\mathbf{p}_j) + \mathbf{F}_{rep}(\mathbf{r}_{ij}) + F_a\hat{\mathbf{p}}_i. \tag{4.15}$$

Since the particles are now driven by a constant external force, we can no longer ignore the viscous forces which a colloidal system like this would experience, as the particles would otherwise accelerate without bounds. We will make the assumption that Reynolds number is very low for this system (about 10^{-4} or 10^{-5}[37]), making the viscous drag forces essential cancel out all other forces at all times. The drag forces are modelled linearly as $\mathbf{F}_{drag} = -\gamma_t\mathbf{v} = -\gamma_t\partial_t\mathbf{x}_i$ and $N_{drag} = -\gamma_r\omega = -\gamma_r\partial_t\theta_i$, where γ_t and γ_t are correspondingly the translational and rotational friction coefficients. The result of this are the overdamped equations

$$\gamma_t\frac{\partial \mathbf{x}_i}{\partial t} = \mathbf{F}_{i,dip}(\mathbf{r}_{ij};\mathbf{p}_i,\mathbf{p}_j) + \mathbf{F}_{rep}(\mathbf{r}_{ij}) + \gamma_t v_a\hat{\mathbf{p}}_i \tag{4.16}$$

$$\gamma_r\frac{\partial \theta_i}{\partial t} = (\mathbf{p}_i \times \mathbf{E}_{j,dip}(\mathbf{r}_{ij};\mathbf{p}_i,\mathbf{p}_j)) \cdot \hat{\mathbf{n}}. \tag{4.17}$$

where we have replaced the self propelling force with the active swim speed $v_a = F_a/\gamma_t$. In these equations both m and I have completely dropped out, making this a non-inertial system.

The final missing ingredient is some sort of fluctuation or noise source, be it thermal or biological in nature. The usual way this is implemented in Brownian dynamics simulations is to have a stochastic translational force term with a random direction and amplitude at each time t. However, for active particles the direction of self-propulsion would not be affected by this sort of noise term, making the classical diffusive behaviour of Brownian particles dominated by ballistic swimming even in high noise regimes.

A better way to implement the stochastic term in our system is therefore to instead include it in the rotational equation eq. (4.17). The equation then becomes

$$\gamma_r\frac{\partial \theta_i}{\partial t} = (\mathbf{p}_i \times \mathbf{E}_{j,dip}(\mathbf{r}_{ij};\mathbf{p}_i,\mathbf{p}_j)) \cdot \hat{\mathbf{n}} + \gamma_r\sqrt{2D_r}\Xi_i(t), \tag{4.18}$$

where $\Xi_i(t)$ is a Gaussian random variable with properties

$$\langle \Xi_i(t) \rangle = 0 \tag{4.19}$$

$$\langle \Xi_i(t)\Xi_j(t') \rangle = \gamma_r\delta_{ij}\delta(t-t'). \tag{4.20}$$

The magnitude of the fluctuation is in the form $\sqrt{2D_r}$ to make the characteristic decorrelation time of the particle orientation $\tau_0 = 1/D_r$ [38], meaning that high values of D_r will make the particles highly correlated with itself in time, and low values will make them quickly lose correlation.

Notice that this is not true Brownian motion, as the diffusion is in that case explained by

the Einstein relation $\gamma D = k_B T$[39], an example of the more general fluctuation-dissipation theorem[40]. Our "active Brownian" system in not in thermal equilibrium, so it does not have a well defined temperature. Instead the rotational diffusion is in our case rather a continuous time model of, for example, tumbling events in run-and-tumble bacteria, or particle reorientation occurring due to hydrodynamic scattering off other particles. The rotational diffusion of purely thermal origin is typically several orders of magnitude weaker than these mechanisms, which is another argument to neglect the translational diffusion also due to thermal fluctuations[38].

4.5 Periodic and bounded domains

While the dynamics of the particles are determined by eq. (4.16) and eq. (4.18), it remains to consider what sort of domain the particles should inhabit. As we are interested in the thermodynamic limit where the number of particles goes to infinity (or rather to 10^{23}), a typical trick to approximate an infinite system is to have periodic boundary conditions. For a 2D system, this can be done by having a square $L \times L$ system, where the right/top and left/bottom edges are glued together. This gives the system the topology of a torus, but the intention is that the effects of this exotic topology will vanish as $L \gg r_0$. This is the approach used in the original Vicek model, which we demonstrated in chapter 3.

Using periodic bounds will allow the particles to translate in the same direction for arbitrarily long periods, leading to the spontaneous rotational symmetry breaking of the Vicsek model. However, this is obviously an unobtainable experimental system configuration. Instead, experiments typically use circular or rectangular bounds. The question then remains how these walls should interact with the particles.

One approach is to have reflective walls, where the particles will bounce off the wall when it hits it. This is how the circular walls are implemented in [41] and [7], where in the latter this is justified experimentally from their observations of Quincke rollers. To have specular reflection, the particle orientation is transformed as

$$\mathbf{p}_i \to \mathbf{p}_i^* = \mathbf{p}_i - 2(\mathbf{p}_i \cdot \hat{\mathbf{n}}_w) \cdot \hat{\mathbf{n}}_w, \tag{4.21}$$

where $\hat{\mathbf{n}}_w$ is the normal vector of the wall at the point of impact, see fig. 4.7. The physics behind such a reflection is a bit dubious in our case, as the only way to change the particle orientation in our overdamped, inertialess system is to exert a torque on the particle. However, is it the most reasonably way to avoid the particles piling up at the boundary as they collide into it.

A mechanism more in line with the dynamics of the system otherwise would be to simply treat the wall like colliding into a stationary particle, with the force always pointing radially inwards. For a circular system with radius R with its centre in $\mathbf{R}_0$, the repulsive potential of the wall would be

$$U_{wall}(\mathbf{r}_i) = \begin{cases} 8\epsilon \left[\left(\frac{\sigma}{r_c + R - |\mathbf{r}_i - \mathbf{R}_0|} \right)^{12} - \left(\frac{\sigma}{r_c + R - |\mathbf{r}_i - \mathbf{R}_0|} \right)^{6} \right] - 2 f_s r + 2\epsilon_s, & |\mathbf{r}_i - \mathbf{R}_0| \geq R \\ 0, & |\mathbf{r}_i - \mathbf{R}_0| < R, \end{cases} \tag{4.22}$$

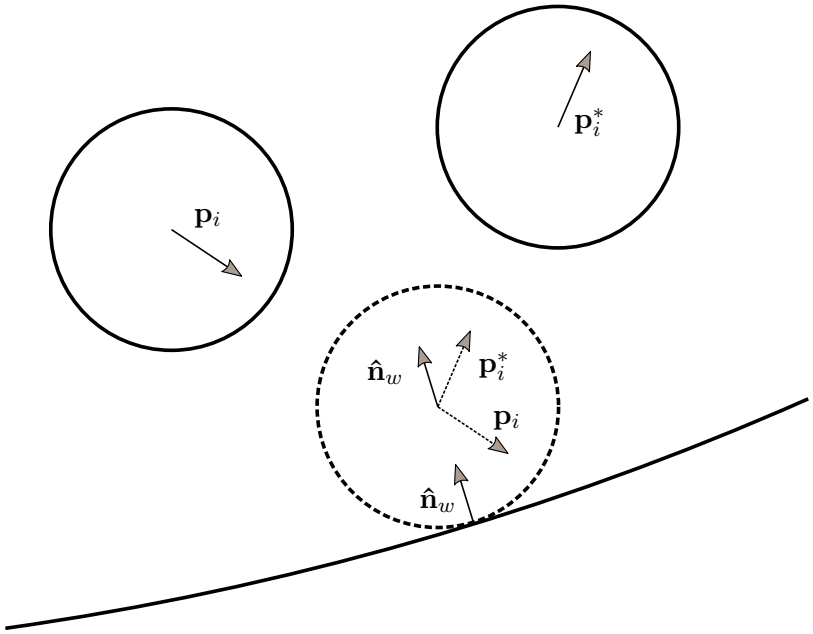

Figure 4.7: Specular reflection of a particle on the boundary.

where $r_c = (26/7)^{1/6}\,\sigma \approx 1.24\sigma$ like for eq. (4.11). The case where $|\mathbf{r}_i - \mathbf{r}_0| \geq R + r_c$ is forbidden and will only occur if the simulation is for some reason unstable. Notice that the strength of this potential has been doubled compared to eq. (4.11). This is because two colliding particles will both be affected by the potential of the other, making the *difference* in force acting on these particles twice the value of eq. (4.12). Since the particle does not affect the wall, the strength is doubled to make the difference in force equal.

The presence of walls has the potential to change the dynamics of active systems quite dramatically, as the domain is no longer homogenous like it is for periodic boundary conditions. Numerical and theoretical studies have been made into confined active matter using Vicsek-like models[41, 42], which show rotating swarms. The radial density is found to go as a power law, with higher exponents for lower noise, which should be possible to identify with a log-log plot. See appendix C for more details and examples of circularly confined active systems from other studies.

5 | Simulation method

With the equations of motion laid out in full, it is time to put the pieces together and set up a simulation. The numerical and computational details are found in section 5.2 and section 5.3, but first we will map out the physical parameters of the simulated systems and reduce them down to the free parameters $(\phi, \zeta^{-1}, \tilde{v}_a, \tilde{p})$. This is useful both for simplifying the calculations and for understanding the simulation results.

5.1 Units and parameter values

Table 5.1

Quantity	Symbol	Dimensions	Dimensionless form	Value
Particle radius	r_0	L	1	Length unit
Potential energy	ϵ	GL^3	1	Modulus unit
Translational friction coefficient	γ_t	GTL	1	Time unit
Permittivity	ϵ_0	$P^2G^{-1}L^{-6}$	1	Dipole moment unit
Dipole moment	p	P	$\tilde{p} = p/\sqrt{\epsilon_0 \epsilon r_0^3}$	3 (unless specified)
Repulsion diameter	σ	L	$\tilde{\sigma} = \sigma/r_0$	2
Rotational friction coefficient	γ_r	GTL^3	$\tilde{\gamma}_r = \gamma_r/r_0^2$	1
Rotational diffusion coefficient	D_r	T^{-1}	$\zeta^{-1} = D_r r_0/v_a$	To be varied
Active swim speed	v_a	LT^{-1}	$\tilde{v}_a = v_a \gamma_t r_0/\epsilon$	1 (or 0 for passive)
Number of particles	N	1	N	1024 (or 2048)
Effective area fraction	ϕ	1	ϕ	To be varied

Table 5.1 shows the parameters defining the active dipole system described in chapter 4. We are using the GLT dimensions space, consisting of modulus G[1], length L and time T, with the addition of dipole moment P representing either electric or magnetic dipole moment. This additional dimension can be cut out entirely, abstracting the interaction further away from the underling physics, but it essentially is anyway by setting the permittivity (or equivalently permeability) to unity and using the dimensionless form $\tilde{p}$ as defined in table 5.1. The other dimensions have their units set by the the particle radius r_0, the energy scale of the repulsion ϵ and the translational friction coefficient γ_t.

[1]Using the symbol G as in the shear modulus, same dimension as pressure.

5.1.1 Repulsion diameter σ

After these 4 quantities have been set to unity, there still remains 7 potentially free parameters. The particle diameter σ does play into the dynamics of the particles both in the repulsive potential eq. (4.11) and rotational friction coefficient (see eq. (5.3)), so one might be lead to believe that its value would impact the balance between the difference forces acting on the particles. This would obviously be absurd, as it's pegged to the length unit, the particle radius r_0, by definition. As a sanity check, we consider how the time rates related to rotation and translation scale with the particle size if the distance between the particles is also rescaled equally. The angular velocity will scale as $\omega = N_{dip}\frac{1}{\gamma_r} \propto \frac{p^2}{\sigma^3}\frac{1}{\sigma^2} = \frac{p^2}{\sigma^5}$ and the time to translate one particle length $\frac{v}{\sigma}$ will scale as some linear combination of $\frac{F_{rep}}{\gamma_t\sigma} \propto \frac{1}{\sigma^2}$, $\frac{F_{dip}}{\gamma_t\sigma} \propto \frac{p^2}{\sigma^5}$ and $\frac{F_a}{\gamma_t\sigma} \propto \frac{v_a}{\sigma}$. So any change in particle size from σ_1 to σ_2 can be reciprocated by a rescaling of the dipole moment so that $\frac{p_1^2}{\sigma_1^3} = \frac{p_2^2}{\sigma_2^3}$ and the active velocity so that $v_{a,1}\sigma_1 = v_{a,2}\sigma_2$, which will make sure that both ω and $\frac{v}{\sigma}$ scale as $\frac{1}{\sigma^2}$. In other words, the dimensionless forms $\tilde{p}$ and $\tilde{v}_a$ together span the space of particle interactions, making it redundant to also vary the value of σ.

5.1.2 Friction coefficients γ_t and γ_r

Off the quantities containing the dimension time, the rotational diffusion coefficient and swim speeds are not suitable for defining the time unit, as we want to preserve the opportunity to set them both to zero. Therefore the translation friction coefficient γ_t is the logical choice for this role, making the unit of time be

$$\tau = \gamma_t r_0^2/\epsilon. \tag{5.1}$$

However, using γ_t for this ends up having some, at first glance, puzzling side effects. Using Stokes law[43], the translational friction coefficient from (low Reynolds number) drag on a small sphere is

$$\gamma_t = 6\pi\mu r_0, \tag{5.2}$$

where μ is the dynamic viscosity of the solvent. Since μ has dimension GT we can use it to define the time unit, but the inclusion of the modulus dimension G makes it quite sensitive to a rescaling of L through the fixed ϵ value. This is why the active swim speed has to be *decreased* when the particle radius is *increased*, as stated above in section 5.1.1. Increasing the particle radius, but not changing the friction coefficient and repulsive potential scale will indirectly make the fluid much more viscous, meaning the active swim speed has to be decreased to keep it in line with the other forces.

Related to the translation friction coefficient is the rotational friction coefficient, which through a similar argument as Stokes law is related to its translational sibling as

$$\gamma_r = \gamma_t\sigma^2/3 = 4\gamma_t r_0^2/3 \tag{5.3}$$

for small spheres[9]. In our unit system, the dimensionless rotational friction coefficient should then be $\tilde{\gamma}_r = \gamma_r/r_0^2 = 3/4$, but we have simplified it to unity. Since both friction coefficient are set to unity the calculations get somewhat simpler, and the change can either be interpreted as the particles not being totally smooth spheres or deviating from a simple

sphere otherwise. This simple constant particle mobility approach is very simplified anyway compared to more complex hydrodynamic models, but since we are focusing on the dipole interactions and not hydrodynamics we leave it at this level.

5.1.3 Rotational diffusion coefficient D_r and ζ

Looking at the way the rotational diffusion coefficient D_r is included in eq. (4.18) it might seem that the dimensions do not match up at first glance. $\sqrt{2D_r}\Xi(t)$ should have dimension T^{-1}, but that is also the dimension of D_r. A way to justify this is to remember that this stochastic term only obtains a macroscopic value as you integrate it over t. This requires Itô calculus for rigorous treatment, but if we imagine it as a sum of $n = t/\Delta t$ terms we can relate it to the central limit theorem. Essentially, while $\int_0^t C dt = Ct$, for a standard Gaussian variable you instead get $\int_0^t C\Xi(t)dt = C\Xi(t)\sqrt{t}$. This way the dimensions end up being correct.

The dimensionless form of D_r deviates from the others, as it does not purely use the dimension units but rather related the diffusion to the swim speed v_a. As stated in section 4.4, $\tau_o = 1/D_r$ is the characteristic decorrelation time of the particle's orientation. Following the argument of [38], the characteristic time interval between particle collision is

$$\tau_c = \frac{Rf(\phi)}{v_a}, \tag{5.4}$$

where $f(\phi)$ is an adimensional function of the area fraction, believed to decrease with increasing ϕ. For a dilute system it could be estimated as $f = \pi/\phi$ from mean free path arguments, but for more crowded systems we might assume $f \approx 1$. Since we don't want to make too many assumptions about how the system will behave, we keep it as 1. The ratio between these two time scales is then

$$\zeta = \frac{\tau_o}{\tau_c} = \frac{v_a}{D_r r_0}. \tag{5.5}$$

This is a dimensionless version of the otherwise equivalent *persistence length* defined in [44].

For $\zeta \ll 1$ we should expect the particle motion to be primarily diffusive, as it changes orientation many times between collisions with other particles. In the non-interacting limit, this will give the particle an effective translational diffusion coefficient $D_{eff} = v_a^2/(2D_r)$ [45]. We can verify this by considering the measured mean squared displacement of the particles $\langle|\mathbf{x}(t) - \mathbf{x}_0|^2\rangle_i$ which (for $N \to \infty$) is expected to be equal to $4D_t t$ for stochastic translational diffusion in two dimensions.

For $\zeta \gg 1$ the motion will instead be dominated by ballistic swimming between collisions, with slow orientational corrections being less important. It's in this regime that we expect the dipole interactions will be important, as the affects will not be averaged away by the rapid fluctuations in $\mathbf{p}_i \cdot \mathbf{p}_j$.

We will use both ζ and ζ^{-1} when describing about this parameter, as the non-inverse version is more human-readable for $\zeta > 1$ (mainly the values we'll be using), but ζ^{-1} is the actual dimensionless form of D_r. ζ^{-1} can also be interpreted as an *effective temperature*, as an analogue to the equilibrium Einstein relation mentioned in section 4.4.

5.1.4 Effective area fraction ϕ

The last intensive defining system parameter is the effective area fraction ϕ, a measure of the systems density. For rectangular $L \times L$ systems it is defined as

$$\phi_{rect} = \frac{N\pi r_0^2}{L^2}, \tag{5.6}$$

and for a circular system with radius R it is defined as

$$\phi_{circ} = \frac{Nr_0^2}{R^2} \tag{5.7}$$

Using these definitions we imply that the size of the particles are set by the diameter $\sigma = 2r_0$ used in the repulsion potential U_{rep}. However, this is a soft potential, meaning that it is possible to potentially pack the system with $\phi \gtrsim 1$. This would be a severely stressed system due to the sharp $1/r^{12}$ behaviour, so it would require a much smaller time step than usual to remain stable. The most dense way to pack circles in the plane without overlap is hexagonal, which can be shown to have area fraction $\phi_{hex} = \pi\sqrt{3}/6 \approx 0.9069$ [46]. This is the maximum density we should expect to observe anywhere in the system, but seeing how the attractive minimum shown in fig. 4.5 is located further out than σ the realistic maximum is likely even lower. The particles are also possibly not the only soft part of the system, as a system with a bounded domain can have similarly soft walls as described by eq. (4.22). These soft walls will make the effective area of the domain bigger than for reflective walls, but the difference should be small for $R \gg r_0$.

5.1.5 Particle number N

Finally, the particle number N is the only really extensive parameter of the system, and together with the area fraction ϕ it defines the domain size. For the thermodynamic limit we want this number to go to infinity, but as this is obviously impossible to directly simulate we have to settle for the largest number that is still practical. When calculating the interaction between every particle at each time step, the run time will scale as $\mathcal{O}(N^2)$. Meanwhile, the error of the measured averages will only scale as $\mathcal{O}(1/\sqrt{N})$ due to the central limit theorem, so at some point you have to make a compromise between the scale of the simulation and the time it takes to run it. For our program a practical value ended up being $N = 1024$, but larger values like $N = 2048$ are also used, which provides us with a convergence check. A last consequence of N is that it affects the local curvature the particles see for a circular boundary, as the radius increases with N but the particle radius remains the same. This has some consequences for the results, discussed in section 6.3.3

5.1.6 Summary

So in summary, the important free parameters of the simulation are the dipole moment p, the rotational diffusion coefficient D_r, the active swim speed v_a and the density ϕ. This is a very large parameter space, represented in dimensionless form as $(\phi, \zeta^{-1}, \tilde{v}_a, \tilde{p})$, so one has to prioritize what to investigate first. Physical experiments like the one in [7] primarily vary the density, as this is controlled by the amount of particles used in the sample. The other parameters are more difficult to control, but in a simulation the only limiting factor

is the time available to experiment.

In our case, as we are most interested in observing a phase transition, we focus on the diffusion parameter D_r, or rather it's inverse ζ, the dimensionless persistence length. Different ϕ are also experimented with, but not with the same resolution as ζ. p is fixed as $\tilde{p} = 3$ unless stated otherwise, as this was found to be a satisfactory sweet spot for interesting behaviours, but low and high p regimes are also investigated (see appendix B). v_a is only checked for 1 and 0, as different v_a will strongly affect the convergence of the simulation. In [9] the active dipole-dipole dynamics are investigated with much higher resolution in the swim speed parameter, but it is for only a handful of particles without noise. While they study the micro interactions, we study the macro interactions. And finally, we also look at the different boundary configurations, as described in section 4.5.

5.2 Integrating the equations of motion

Now that both the dynamical equations and system parameters have been defined, it only remains to define the integration scheme of the differential equations. In previous studies it seems that the most prevailing method is the simplest one of them all: Euler's method, or rather the Euler-Maruyama (EM) method due to the stochastic diffusion term. Adapting eq. (4.16) and eq. (4.18) with this first order method gives

$$\begin{aligned}\mathbf{x}_i(t+\Delta t) &= \mathbf{x}_i(t) + \Delta t(\mathbf{v}_a(t) + \mathbf{F}_i(\mathbf{r}_{ij})/\gamma_t) \\ &= \mathbf{x}_i(t) + \Delta t\hat{\mathbf{x}}(v_a\cos\theta_i(t) + F_{x,i}(\mathbf{r}_{ij})/\gamma_t) \\ &\quad + \Delta t\hat{\mathbf{y}}(v_a\sin\theta_i(t) + F_{y,i}(\mathbf{r}_{ij})/\gamma_t)\end{aligned} \tag{5.8}$$

$$\begin{aligned}\theta_i(t+\Delta t) &= \theta_i(t) + \Delta t(\mathbf{p}(t)\times\mathbf{N}_i(\mathbf{r}_{ij}))\cdot\hat{\mathbf{n}}/\gamma_r + \sqrt{2D_r\Delta t}\Xi_i(t) \\ &= \theta_i(t) + \Delta t(v_a\cos\theta_i(t)N_{y,i}(\mathbf{r}_{ij}) - v_a\sin\theta_i(t)N_{x,i}(\mathbf{r}_{ij}))/\gamma_t \\ &\quad + \sqrt{2D_r\Delta t}\Xi_i(t)\end{aligned} \tag{5.9}$$

where $\Xi_i(t)$ is for each i and t a sample of $\mathcal{N}(0,1)$. $\mathbf{F}_i$ is the total force acting on particle i, a sum of eq. (4.8) and eq. (4.12) from all other particles $j \neq i$, and $\mathbf{N}_i$ is the torque acting on particle i from all other $j \neq i$ according to eq. (4.5). Using $\sqrt{\Delta t}$ instead of Δt in the stochastic term will make the means squared displacement equal for different time steps.

5.2.1 Adams-Bashforth integration

While it is advised to stick to first order methods due to the time it takes to calculate all the forces, you are not necessarily stuck with using EM. Using linear multistep methods you can leverage the information from previous time steps to (hopefully) gain efficiency. One such method is the Adams-Bashforth (AB) method, of which we will use the 2 step version (AB2). It is quite easily adaptable for our stochastic equation due to the fact that all the prefactors of Ξ are constants, but the general case is more complicated[47]. It is most simply stated by first defining

$$
\begin{aligned}
Y_{x,i}(t) &= v_a \cos\theta_i(t) + F_{x,i}(\mathbf{r}_{ij})/\gamma_t, \\
Y_{y,i}(t) &= v_a \sin\theta_i(t) + F_{y,i}(\mathbf{r}_{ij})/\gamma_t, \\
Y_{\theta,i}(t) &= (v_a \cos\theta_i(t) N_{y,i}(\mathbf{r}_{ij}) - v_a \sin\theta_i(t) N_{x,i}(\mathbf{r}_{ij}))/\gamma_t.
\end{aligned}
$$

Using this we can state the AB method as

$$
\begin{aligned}
\mathbf{x}_i(t+\Delta t) = \mathbf{x}_i(t) &+ \Delta t \hat{\mathbf{x}} \left(\frac{3}{2} Y_{x,i}(t) - \frac{1}{2} Y_{x,i}(t-\Delta t) \right) \\
&+ \Delta t \hat{\mathbf{y}} \left(\frac{3}{2} Y_{y,i}(t) - \frac{1}{2} Y_{y,i}(t-\Delta t) \right)
\end{aligned}
\tag{5.10}
$$

$$
\theta_i(t+\Delta t) = \theta_i(t) + \Delta t \left(\frac{3}{2} Y_{\theta,i}(t) - \frac{1}{2} Y_{\theta,i}(t-\Delta t) \right) + \sqrt{2 D_r \Delta t}\, \Xi_i(t) \tag{5.11}
$$

AB, compared to EM, is more responsive to changes in the integrand, as it will essentially extrapolate the current trend based on the a sample from times t and $(t-\Delta t)$. A previous active matter study [48] found the AB scheme more accurate for Brownian dynamics than the more typical EM scheme. A comparison of the relative displacement error (essentially the error in the value of $\sqrt{Y_{x,i}(t)^2 - Y_{y,i}(t)^2}$ at the same time t) is shown in fig. 5.1, where AB has a smaller error at almost all times. This motivates using AB in the remaining simulations.

5.3 Implementation

The system is simulated in Python, mainly relying on the scientific computing package NumPy[2]. Python is not a compiled programming language, so it trades off speed for ease of development and use. NumPy tries to bridge the gap by implementing N-dimensional array objects, which can be efficiently transformed element-by-element with "universal functions". This is done under the hood in C, making NumPy computations much quicker than procedural for loops in Python. The Python overhead can be further minimized using packages like Numba[3], which is able to compile functions which use NumPy and can approach machine code speeds.

The force and torque calculations both depend on the distance and angle between the particles, so in each time step the x_i and y_i position vectors are broadcast into $N \times N$ matrices and used to calculate the distance matrix r_{ij} and angle matrix α_{ij}. The remaining calculations are then done by operating on these matrices with NumPy's universal functions, along with the similarly broadcast θ_i vector. Lastly, the j dimension is summed over and we get the forces and torques used eq. (5.10) and eq. (5.11). No for-loops are used within the time step calculation, which enables "plug-and-play" parallelization through Numba. Numba is able to do this so painlessly because it doesn't matter which order the element-

[2] https://docs.scipy.org/doc/numpy/reference/index.html
[3] http://numba.pydata.org/

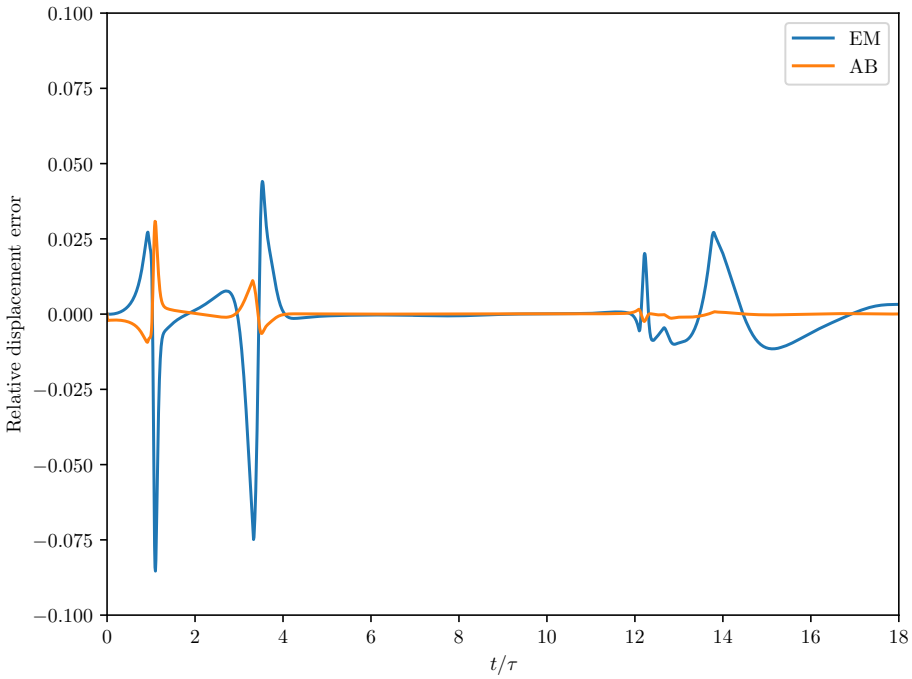

Figure 5.1: The relative displacement error of a single particle at different times. Both method used a time step of $\Delta t = 0.01\tau$, and they were compared to a EM simulation with $\Delta t = 0.0001\tau$. The large fluctuations in the beginning are due to particles being initialized close together. We conclude from this plot that AB is clearly more suited. With $N = 128$ and $D_r = 0$, as it would be difficult to compare simulations with noise of different time steps.

wise universal functions are evaluated, only the final output matters. On a laptop with 4 available threads this amounts to about a 6x speed up, and on the Department of Physics' servers with 12 available threads this can be increased even more.

The time step is typically initiated as $\Delta t = 0.01\tau$, but the displacement is monitored at each step to ensure that is stays less than $\sigma/100$ for all particles. If the displacement becomes much larger than this the system is likely to become unstable, as the particles that end up to close will be violently repelled by the $1/r^{12}$ potential and can a chain reaction of overlapping particles. If any displacement over $\sigma/100$ is detected then the time step is halved and the system reloaded to the last saved snapshot. The system is saved every 1τ and will keep the current reduced time step for 6τ before it is reverted to the initial value. For systems with $v_a < 1$ a larger initial time step can be used, but $v_a > 1$ will require smaller time steps. And before the simulation is run, the initial random particle positions are relaxed with $v_a = 0$ and smaller time steps.

A curious artefact of using Numba is that it uses slightly different algorithms for various functions acting on floating-points compared to standard NumPy, like trigonometric functions. This causes simulations using the different suites to diverge from each other after some time, typically after $\Delta t > 100\tau$ for $N = 1024$. Though the difference is very small at first, barely over machine epsilon $\sim 10^{-16}$, using a time step of $\Delta t = 0.01\tau$ means there have been at least $\sim 1024 \cdot 1024 \cdot 100/0.01 \approx 10^{10}$ operations. Since all the particles interact

with each other, it is not really surprising that the small errors propagate forward until the system state diverges. This is however nothing to lose sleep over, as the truncation error from the first order integration method is almost certainly much more important than these tiny round-off errors, as fig. 5.1 shows the relative error can be around the order of 0.01. It can really be thought off as merely another source of noise in addition to the rotational diffusion.

5.3.1 Considerations for interaction cut-off

The fact that the calculations are done element-wise on $N \times N$ matrices makes the runtime scale as $\mathcal{O}(N^2)$, but it might not be necessary to calculate the interaction between very distant particles. This is easier to justify for short-range interactions, but the interactions here might be sufficiently dominated by the closest particles that we can neglect particles far away. A way to do this, as described in [49], is to divide the domain into cells, eg. 5×5, and have the particles only interact with other particles in the same or adjacent cells. If the number of particles is then multiplied by 4, you can make the grid 10×10 instead and each cell will on average have the same amount of particles. This can make the run time scale as $\mathcal{O}(N)$ instead, as the time taken to calculate each cell will remain constant, a great improvement over the standard case.

Implementing this in our heavily NumPy based code does however cause some issues, as this deviates from the usual fixed $N \times N$ dimension matrix operations. The time spent indexing the particles to interact with essentially cancelled out the time gained from neglecting distant particles for $N = 1024$. It might be worth implementing for higher N, but multiplying the particle number by 10 would still take at best 10 times longer to run. For higher particle numbers like 10^5 or 10^6 the program should probably be completely rewritten to C/C++ or Fortran, or with GPU support through a platform like CUDA. So with our program it is best to stick to long range interactions between all particles.

Another form of cut-off is however indirectly implemented in the case of periodic boundary conditions. The classical physics intuition will of course break down if one considers this an *actual* "Escheresque" periodic system, but it can instead be interpreted more meaningfully as a representation of an infinite system where there just happens to be a translation symmetry. The rigorous way to treat this system would then be to sum over all the infinite but progressively weaker contributions to eq. (4.4). This is usually done through what's called Ewald summation[50], which leverages the power of Fourier transformations to deal with this infinite periodic system. However, we have not implemented this in our program and instead make it so that particle i only sees the *nearest* copy of particle j. This is quite easily implemented by calculating the signed distance in each direction, $(x_i - x_j)$ and $(y_i - y_j)$, and operating on them as $\left[\left(\alpha_i - \alpha_j + \frac{L}{2}\right) \mod L\right] - \frac{L}{2}$ so that each of these distances lies in the range $\left[-\frac{L}{2}, \frac{L}{2}\right)$. This is the implicit cut-off range in our system, which has the shape of a $L \times L$ square around each particle.

This square shaped cut-off does have some subtle differences from the usual circular or spherical cut-off. Operating with a fixed r_{cut} preserves the isotropic symmetry of the dynamics, but using the modulus approach instead imposes a discrete D_4 square symmetry. But again, the effect of this new symmetry and the lack of any Ewald-like approach should vanish as L is increased.

6 | Results and discussion

6.1 Passive dipole particles

To gain insight into how an ensemble of dipoles interact we first run simulations with $v_a = 0$, removing the "active" aspect of the system. This is the closest we get to normal, or "passive", Brownian particles, but we are still missing the translational diffusion coefficient. Thus we should expect no net diffusion, but rather relaxation to minimize the total potential eq. (4.7). From our working out in section 4.2 we expect the particles, in the case $\hat{\mathbf{p}}_i \parallel \hat{\mathbf{p}}_j$, to attract when $\hat{\mathbf{p}}_i \cdot \hat{\mathbf{r}}_{ij} = \pm 1$ and repel when $\hat{\mathbf{p}}_i \perp \hat{\mathbf{r}}_{ij}$, and the opposite in the case $\hat{\mathbf{p}}_i \parallel -\hat{\mathbf{p}}_j$. This, in combination with the fact that the particle orientation will align with the local dipole field, leads us to expect the particles to form chains. This is indeed what we observe for low D_r (high ζ) values in our simulations, as shown in fig. 6.1. Here both the arrows on the particles and the particle's colour show the orientation $\hat{\mathbf{p}}$, with the colour according to fig. 3.2d.

The formations shown in fig. 6.1 are more than simply chains, as we also see ring formations of different sizes. This is in line with the findings of de Gennes and Pincus for ferromagnetic colloids with no external field[51]. We also note that the system evolves very slowly and seems to be unable to relax to its global energy minimum even when $D_r = 0$, leaving the system is a frustrated state[52].

The snapshots in fig. 6.1 show examples of particles in different chains with $\hat{\mathbf{p}}_i \parallel -\hat{\mathbf{p}}_j$ attracting, but they also show examples of column aggregation of parallel dipole chains, which might seem contrary to our previous discussion of dipole interactions. This is because we have only been considering single particle interactions and not chains. An explanation of this behaviour is given by fig. 6.3, where we have plotted the potential seen along different paths normal to a signle dipole particle of a chain of 6 particles. The red path toward a single particle shows what we've already discussed for two particles with $\hat{\mathbf{p}}_i \perp \hat{\mathbf{r}}_{ij}$, as it is purely repulsive. However, for a slightly off-centre approach like the green path there seems to be a small potential minima close to $r_{ij} = 2r_0 = \sigma$. This is however not a stable point, as the particle would rather stray off the green path and go in front of the other particle.

The situation changes for a *chain* of dipole particles, here in the case of a chain of 6 particles. While the potentials are still repulsive when the particle is several σ away from the chain centre, when it comes closer than $\sim 8r_0 = 4\sigma$ it will start to attract. Of the orange and blue minima positions shown in fig. 6.3b, the blue has the lowest potential an is therefore the stable position. This causes the triangular interlocking of parallel chains shown in the fig. 6.2. For antiparallel chains we simply change the sign of the dipole potential, as $U_{dip} = -\mathbf{E}_{dip} \cdot \mathbf{p} = \mathbf{E}_{dip} \cdot (-\mathbf{p})$. This would make the red position in fig. 6.3b the one with the lowest potential, explaining why the antiparallel chains in fig. 6.2 have a square crystal structure instead of triangular.

The introduction of rotational diffusion threatens to destabilize these chain and ring formations, as the attraction between the particles is entirely dependent on their relative orientation. It then becomes a balancing act between the torque from neighbouring particles in the chain and the stochastic rotation term to keep these structures. Figure 6.1c shows that the formations in fig. 6.1a can survive weak diffusion, as the $D_r = 0.01$ state was initialized from the relaxed $D_r = 0$ state shown in the figure and ran for a considerable

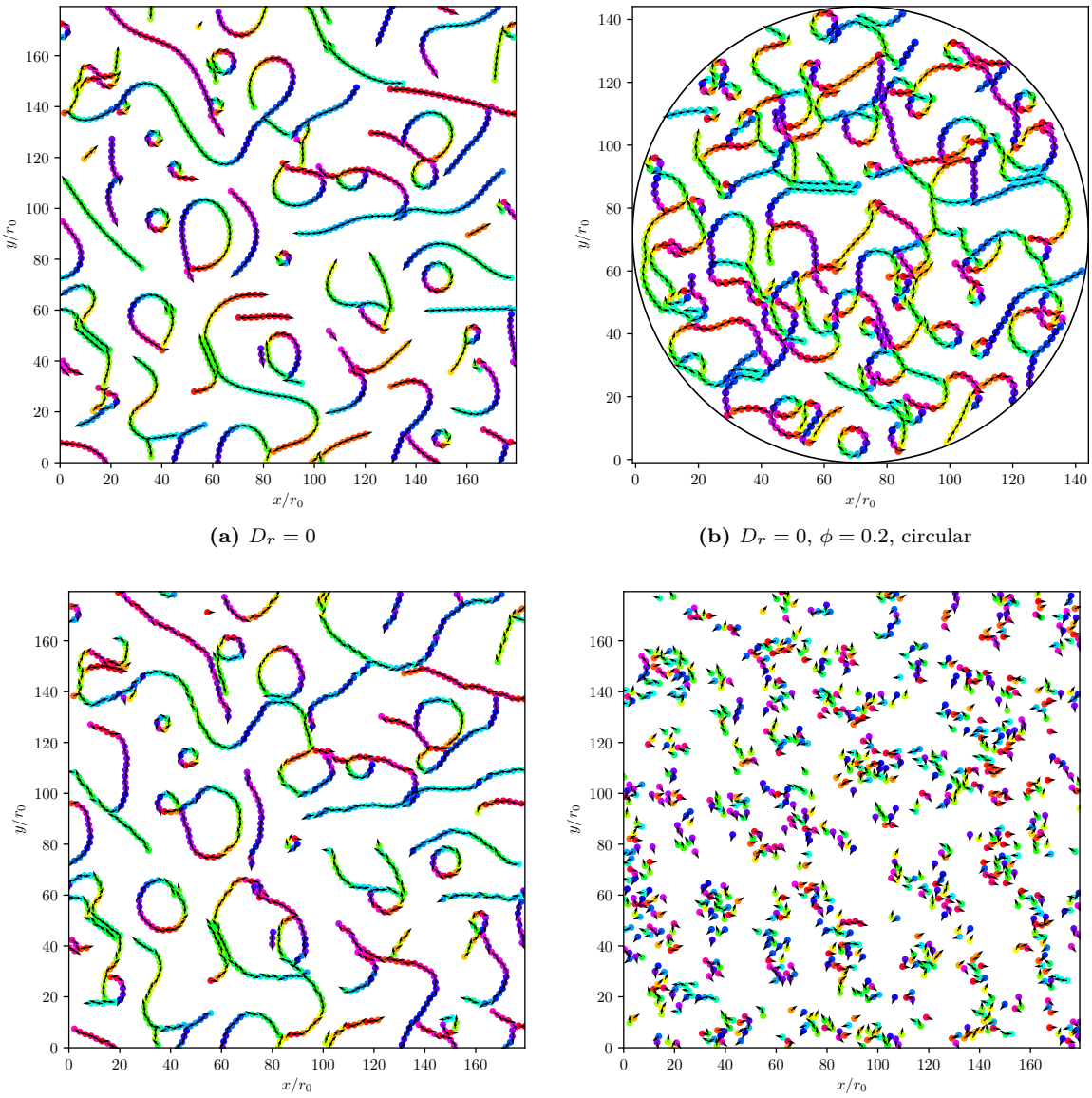

(a) $D_r = 0$

(b) $D_r = 0$, $\phi = 0.2$, circular

(c) $D_r = 0.01$

(d) $D_{=}0.1$

Figure 6.1: Dipole particles with zero propulsion speed, $v_a = 0$. **(a)**, **(c)** and **(d)** show the gradual melting of the structures as rotational diffusion is increased from 0, with area fraction $\phi = 0.1$ and particle number $N = 1024$ in periodic boundary conditions. **(b)** is again a $D_r = 0$ system, but circularly confined and with $\phi = 0.2$. All snapshots are taken after $\Delta t = 10000\tau$ and the colour of the particles indicate its dipole orientation.

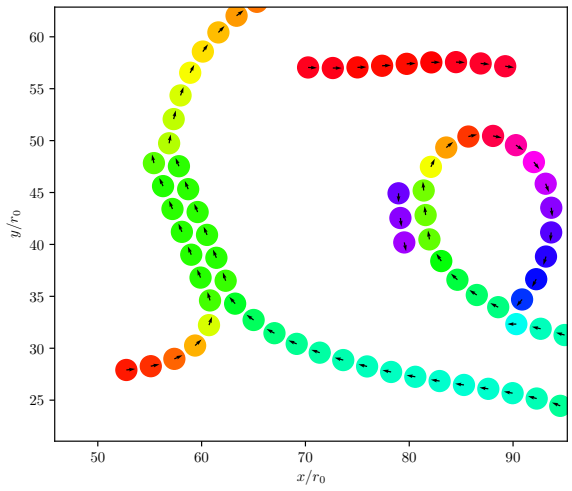

Figure 6.2: Detail of fig. 6.1a, showing both parallel and antiparallel chain attraction. Colours still indicate dipole orientation.

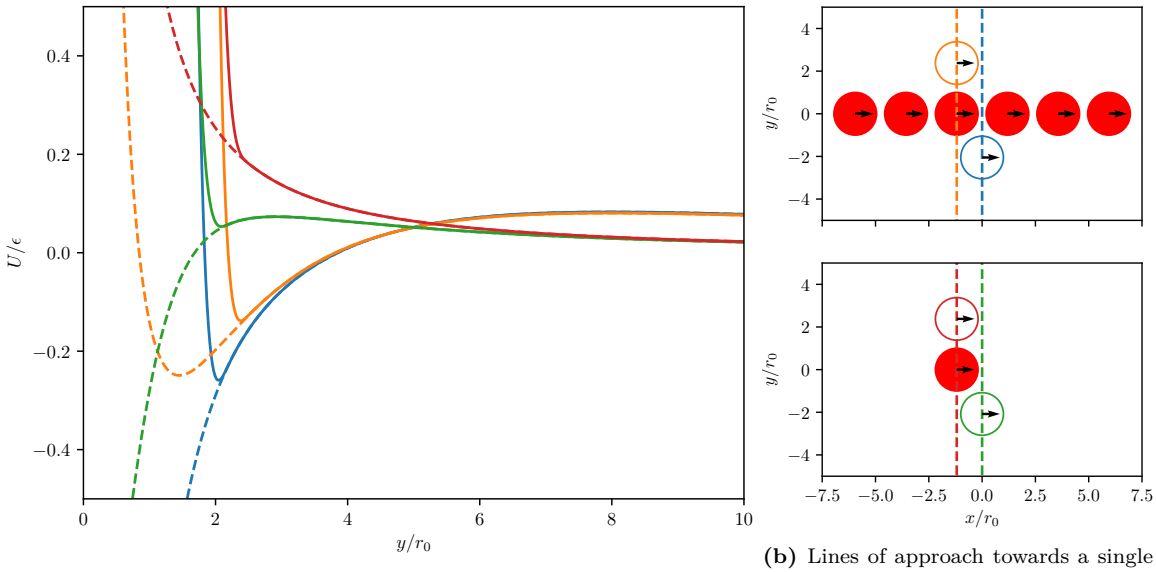

(a) Potential along the paths shown in (a)

(b) Lines of approach towards a single dipole particle and a chain of 6.

Figure 6.3: Diagram showing the difference in potential when approaching a single dipole particle and a chain. The dashed lines (a) is the dipole potential alone, and the solid line is the total potential including the repulsive potential U_{rep}. The different colours in (a) are different lines of approach, corresponding the same coloured paths in (b). The coloured particle outlines in (b) are placed according to the potential minima in (a), except for the red path which has no minimum.

amount of time ($\Delta t = 10000\tau$). Increasing D_r further caused the formations in fig. 6.1a to melt, collapsing into unordered clusters as shown in fig. 6.1d. It is interesting that these clusters appear to form, as it suggests that the randomly rotating dipole particles are more attractive than repulsive. The clear cluster formation is also helped by initializing the system in an ordered state, as a random initialization should take even longer to display any sort of cohesion.

6.2 Active particles in periodic boundary conditions

Though the passive dipole particles displayed a great deal of self-assembly in the case of low rotational diffusion, they did not attain a homogenous global order. The ring and chain formations are entirely local phenomena and end up locking the system into a frustrated state where it does not evolve further. This can be blamed on there not being a mechanism for the particles to explore the phase space of the system, as there is no translational diffusion as long as there is no active speed ($v_a = 0$).

Using $v_a > 0$ means that each of the particles do work along their axis of orientation, allowing them to break out of the relaxed states shown in fig. 6.1. To keep track of the order of these systems, we use the same order parameter as the one used for the Vicsek model in chapter 3, this time expressed as

$$\Pi \equiv \frac{1}{N} \left| \sum_i \hat{\mathbf{p}}_i \right|. \tag{6.1}$$

Like before, for completely ordered (aligned) system this will be 1 and for unordered systems it should go to 0. As an example, this value is correspondingly 0.06, 0.09 and 0.02 for the passive systems shown in fig. 6.1a, fig. 6.1c and fig. 6.1d, reflecting a low degree of global alignment.

Snapshots of systems with $\phi = 0.1$ and $N = 1024$, but $\tilde{v}_a = 1$, are shown in fig. 6.4. Systems of these now active particles with low (dimensionless) persistence length ζ do not lead to any particular ordering and appear like a gas, but for high ζ the particle orientations will spontaneously become ordered along an arbitrary axis and swim that way, appearing like a polar liquid. This results in a order parameter Π with a macroscopic value, without any external field acting on the particles. Figure 6.5a shows the order parameter for a series of ζ values. The order parameter is plotted versus an inverse ζ^{-1} so we can include the case where $\zeta \to \infty$, but also because it then becomes similar to the corresponding plot for the Vicsek model fig. 3.3 and the Ising model, where the quantity along the x-axis is correspondingly rotational noise and temperature. Like these models, the system appear to have a critical ζ^{-1} value below which spontaneous ordering occurs, with a variance peak at this critical point. This again supports the interpretation of $\zeta^{-1} = \frac{D_r r_0}{v_a}$ as an effective temperature, as mentioned in section 5.1.

The critical point for $(\phi, \tilde{p}, \tilde{v}_a) = (0.1, 3, 1)$ using $N = 1024$ seems to be around $\zeta = 70$, as this values corresponds to the peak Π variance in fig. 6.5a. The snapshot of this critical system, fig. 6.4b, does not seem to be globally ordered in a specific direction like the systems with lower "temperature" ζ^{-1}, but it appears to be more clustered than the high ζ^{-1} system shown in fig. 6.4a. The time series of the order parameter for $\zeta = 70$, the orange

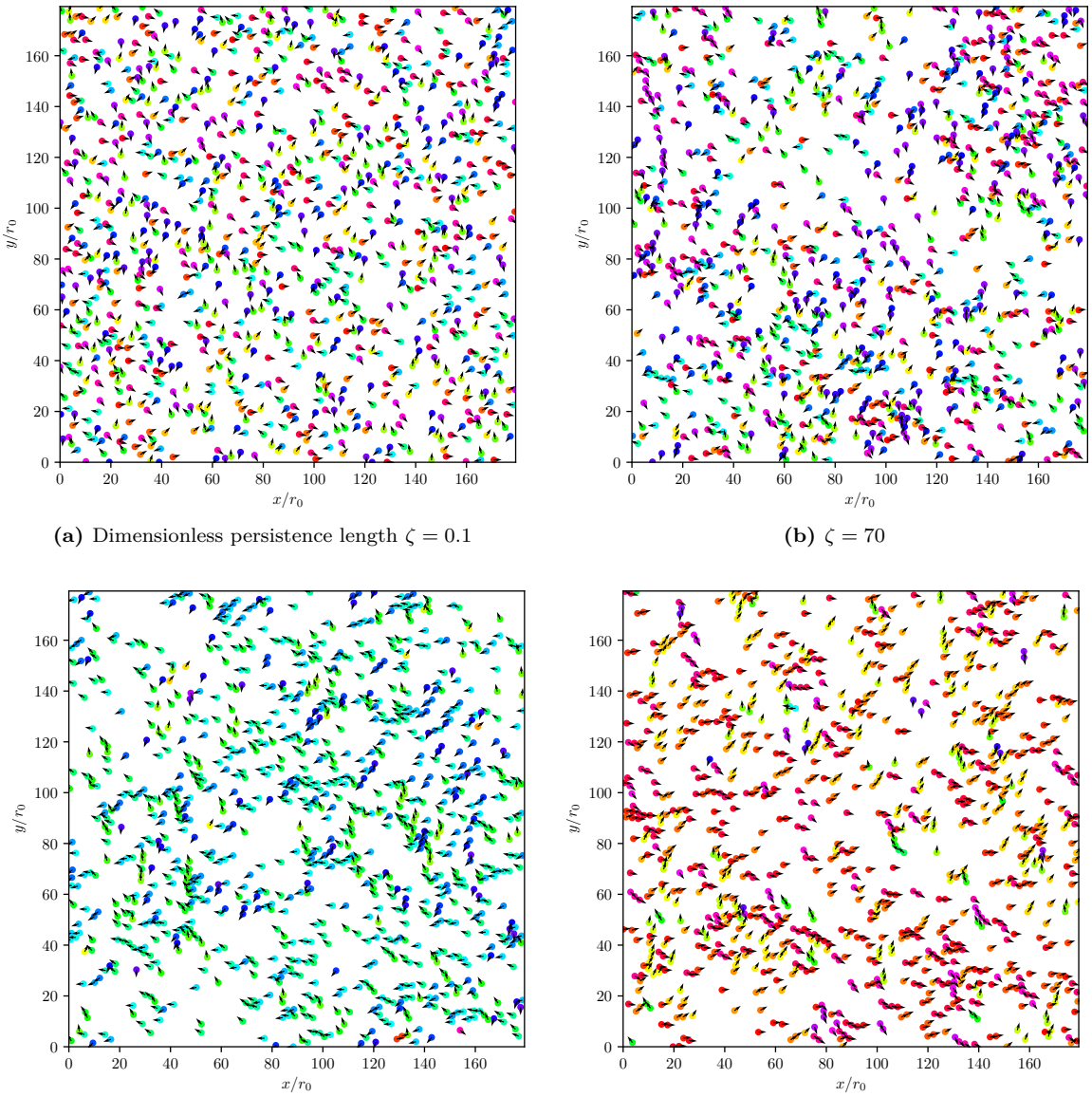

(a) Dimensionless persistence length $\zeta = 0.1$

(b) $\zeta = 70$

(c) $\zeta = 200$

(d) $\zeta = \infty$ ($D_r = 0$)

Figure 6.4: Snapshots of a periodic system with active speed $\tilde{v}_a = 1$, area fraction $\phi = 0.1$ and particle number $N = 1024$, after being simulated for $\Delta t = 8000\tau$. As the dimensionless persistence length ζ is increased, the systems goes from a diffusive gaseous phase in **(a)**, through a critical phase in **(b)** and ending up as an orientationally ordered polar liquid in **(c)** and **(d)**. Colours indicate orientation, once again following fig. 3.2d.

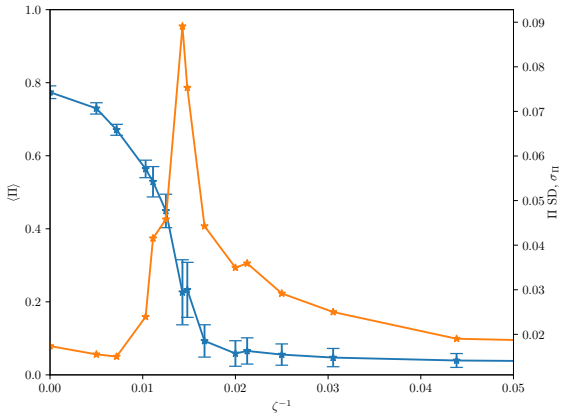

(a) Average order parameter Π (blue) and its standard deviation (orange, and blue error bars) as a function of ζ^{-1}.

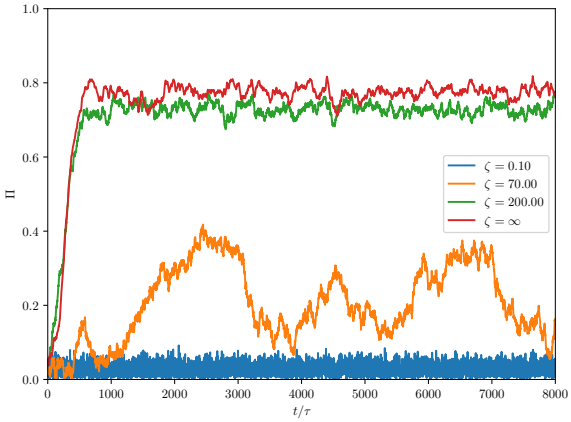

(b) Instantaneous order parameter as the systems evolves from a random initialization for 4 different ζ values. Corresponding to the snapshots in fig. 6.4.

Figure 6.5: Order parameter Π for different ζ. Other parameters corresponding to fig. 6.4. **(a)** shows a clear peak in Π fluctuations at a critical point between the ordered and onordered regime, very similar to fig. 3.3 for the Vicsek model. The averages and standard deviations are estimated from the time series of Π, like the ones shown in **(b)**, after it has stabilized, eg. after $\Delta t = 1000\tau$.

series in fig. 6.5b, reveals that this system fluctuates strongly between partially ordered and unordered, fitting the hypothesis that it is on the threshold between ordered and unordered phases.

Interestingly, the order time series of the two low ζ^{-1} systems shown in fig. 6.5b seem to be quite similar, with the $\zeta^{-1} = 0$ system (red series) being on average more ordered. This system is in theory completely deterministic based on it's initial condition, as there is no stochastic rotation when $\zeta^{-1} = D_r = 0$. Yet it does not become completely ordered with $\Pi = 1$ like its Vicsek model equivalent and has very much the same character as the $\zeta = 200$ system, with sporadic unaligned particles and no persistent long chains, as seen in the snapshots fig. 6.4c and fig. 6.4d. For higher N we expect the order parameter of the unordered phases to become closer to zero and the critical point to become more defined, but the upper limit of Π likely depends on the details of $\tilde{p}$, $\tilde{v}_a$ and ϕ.

6.2.1 Diffusive and ballistic behaviour

Another way to characterise the different phases is to track the paths of the particles and study the mean squared displacement (MSD) $\langle |\mathbf{x}(t) - \mathbf{x}_0|^2 \rangle_i$. In section 5.1 we predicted that systems with $\zeta \ll 1$ would be primarily diffusive, as the decorrelation time of the particle orientations is much lower than the time between collisions. The effective translational diffusion coefficient $D_{eff} \equiv \langle |\mathbf{x}(t) - \mathbf{x}_0|^2 \rangle_i / 4t$ characterizing the random walk of the particles is then predicted to approach $v_a^2/(2D_r) = v_a r_0 \zeta/2$[45].

In contrast, when the system is in an ordered phase the particles should travel in more or less the same direction at all times, making the MSD go as $v_{eff}^2 t^2$, where v_{eff} is the effective drift speed of the particles. So to separate this ballistic regime form the diffusive regime we simply try fitting the MSD to a linear and a quadratic function of time and

extract the leading coefficients, which should be correspondingly $4D_{eff}$ and v_{eff}^2.

Figure 6.6 shows the results of these fits. In fig. 6.6a we see the measured D_{eff} and v_{eff} of the systems with different ζ. Notice that both ζ and the dimensionless $D_{eff}/(r_0 v_a)$ have logarithmic axis, which helps us display a bigger range of ζ values than the ones presented in fig. 6.5a. We see that the measured values follow the theoretical prediction quite closely, although it is consequently lower than the prediction. A likely explanation for this is that the inter-particle repulsion is slowing down the particles as they collide or block each other. The theoretical prediction was originally just for $\zeta \ll 1$, but here we observe this linear behaviour long over this limit. This suggests the dipole alignment interactions are quite weak, since it can't overcome the diffusive behaviour even when the particles collide regularly.

For ζ values high enough to allow spontaneous ordering we start to measure a non-zero v_{eff}, meaning the particles are now in the ballistic regime. Much like the order parameter Π, the dimensionless drift speed v_{eff}/v_a increases until it levels off at a value less than 1. In fact, for particles where the translational motion is entirely determined by the orientation and fixed active speed (ie. the other forces do not contribute), then both the Π and v_{eff}/v_a only depend on the distribution of orientations and should in fact be equal. Π is a sum over the particles and then an average over time, and v_{eff}/v_a is a sum over time and then an average over particles, and in both cases the components of the orientation/displacement perpendicular to the main orientation/displacement cancel each other out, leaving only the sum over the parallel components over the distribution of orientations. And when comparing these values in our simulation they are indeed very close, with v_{eff}/v_a on average being 2% less than the corresponding Π value. This suggests that the particles do not block each others paths very much and allow each other to pass by quite easily.

Lastly, the systems with $\zeta = 60$ and $\zeta = 80$ are used as examples of typical diffusive and ballistic behaviour, as they are correspondingly right below and above the critical point $\zeta_c \sim 70$. Figure 6.6b shows how the character of the MSD changes when going between these two different phases, and fig. 6.6c shows a single particle path. While the blue path in the diffusive regime seems to go no where in particular as it wanders around randomly, the orange path in the ballistic regime has a clear preferred direction. This is a very abrupt change for not a very large jump in ζ, again indicating a phase transition.

6.3 Active particles with circular confinement

We continue looking at active dipole particles with $\tilde{v}_a = 1$, but now we introduce another factor: confinement. We simulated circular systems using the two different boundary interactions described in section 4.5: reflective and repulsive walls. In these systems is it obviously not possible to get the same liquid polar phase as the periodic systems, as the particles are not free to travel in the same direction indefinitely. However, there is still an apparent phase transition as the effective temperature ζ^{-1} is lowered, as shown in the snapshots in fig. 6.7. The particles are observed to form a densely packed layer along the boundary, where they move together as a vortex. The handedness of the emergent vortex is arbitrary, as seen in fig. 6.7c and fig. 6.7d which rotate anti-clockwise and clockwise respectively.

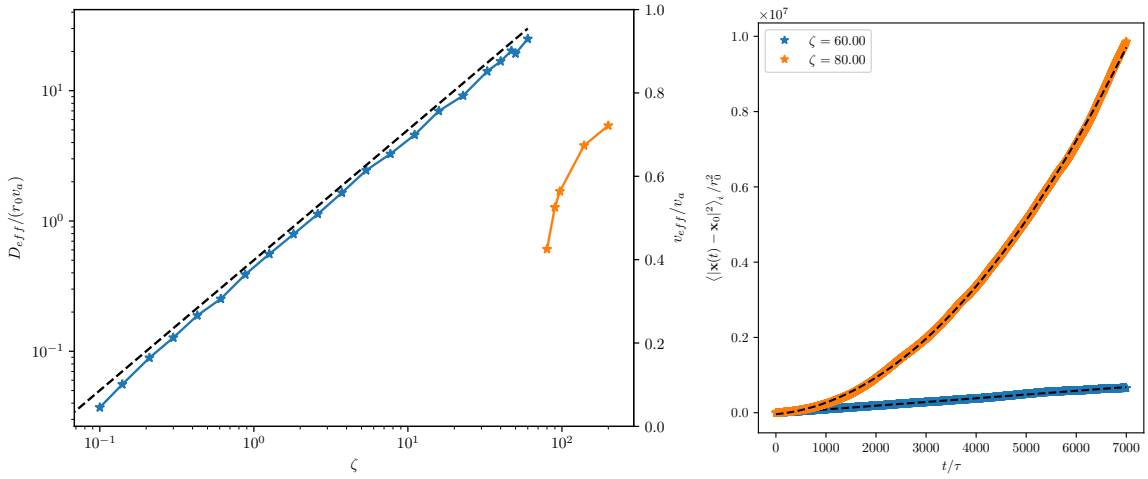

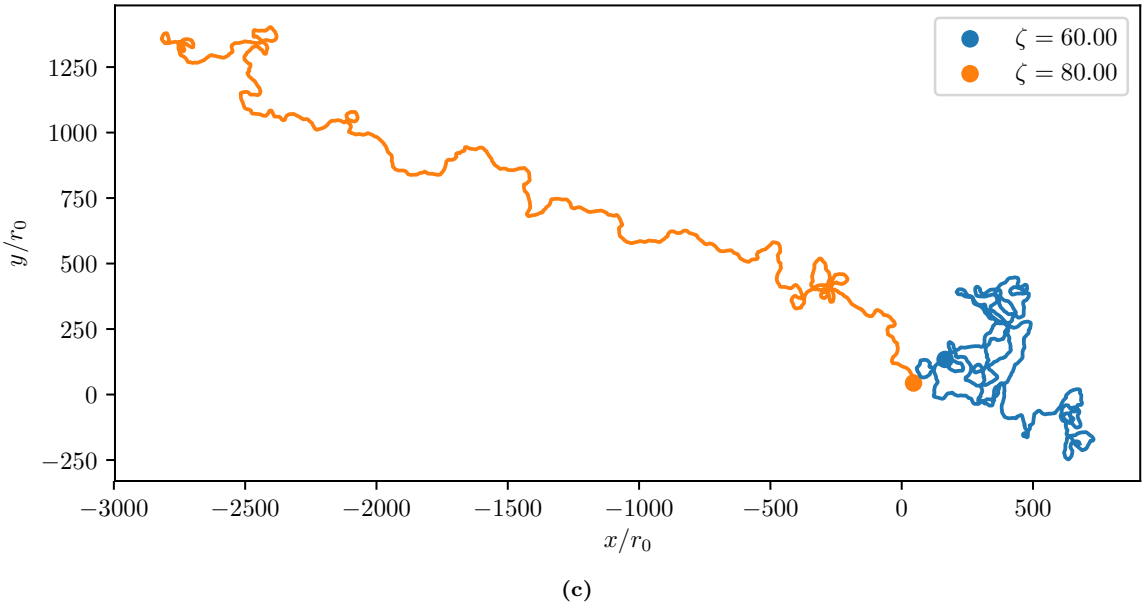

Figure 6.6: Diffusive and ballistic regiment of the particles with periodic boundaries. **(a)** shows the dimensionless effective diffusion coefficient D_{eff} (blue) for the low ζ range and the dimensionless effective drift speed v_{eff} (orange) for the high ζ range. The dashed line is the theoretical prediction for effective diffusion $D_{eff} = v_a^2/(2D_r)$. **(b)** shows how the values of (a) are obtained, through either linear or quadratic fits of the mean squared displacement. Both of the fits shown are very close fits, even though they are close to the critical point. **(c)** shows a single particle path for the diffusive and ballistic regimes, which have a very clear difference in character.

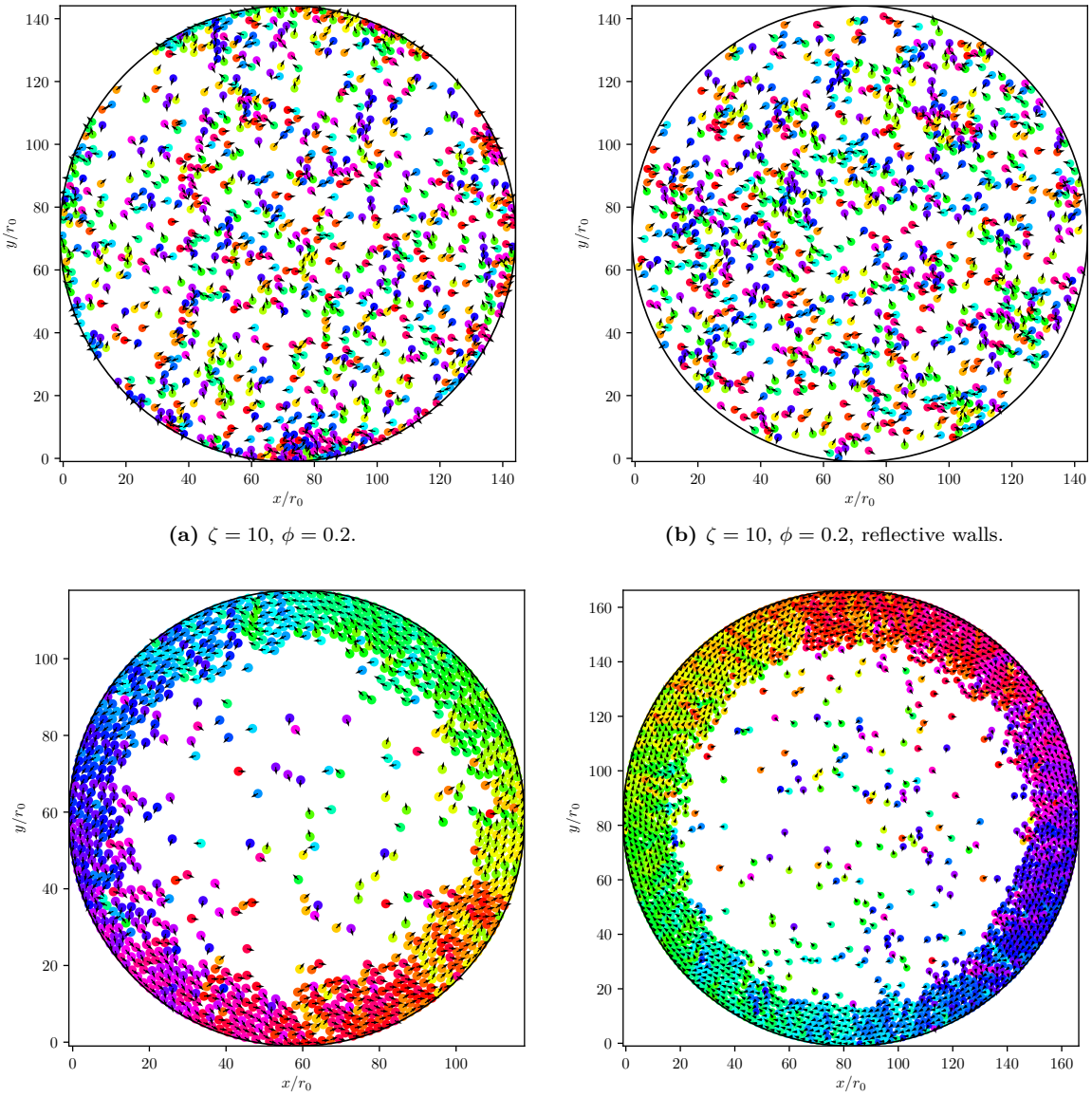

(a) $\zeta = 10$, $\phi = 0.2$.

(b) $\zeta = 10$, $\phi = 0.2$, reflective walls.

(c) $\zeta = 50$, $\phi = 0.3$.

(d) $\zeta = 50$, $\phi = 0.3$, $N = 2048$.

Figure 6.7: Snapshots of active systems on a disk with area fraction $\phi = 0.2$ after several thousand τ. $N = 1024$ for all except (d). **(a)** and **(b)** are entirely gaseous phases, while **(c)** and **(d)** with higher ζ have closely packed orientationally ordered layer which rotates along the boundary.

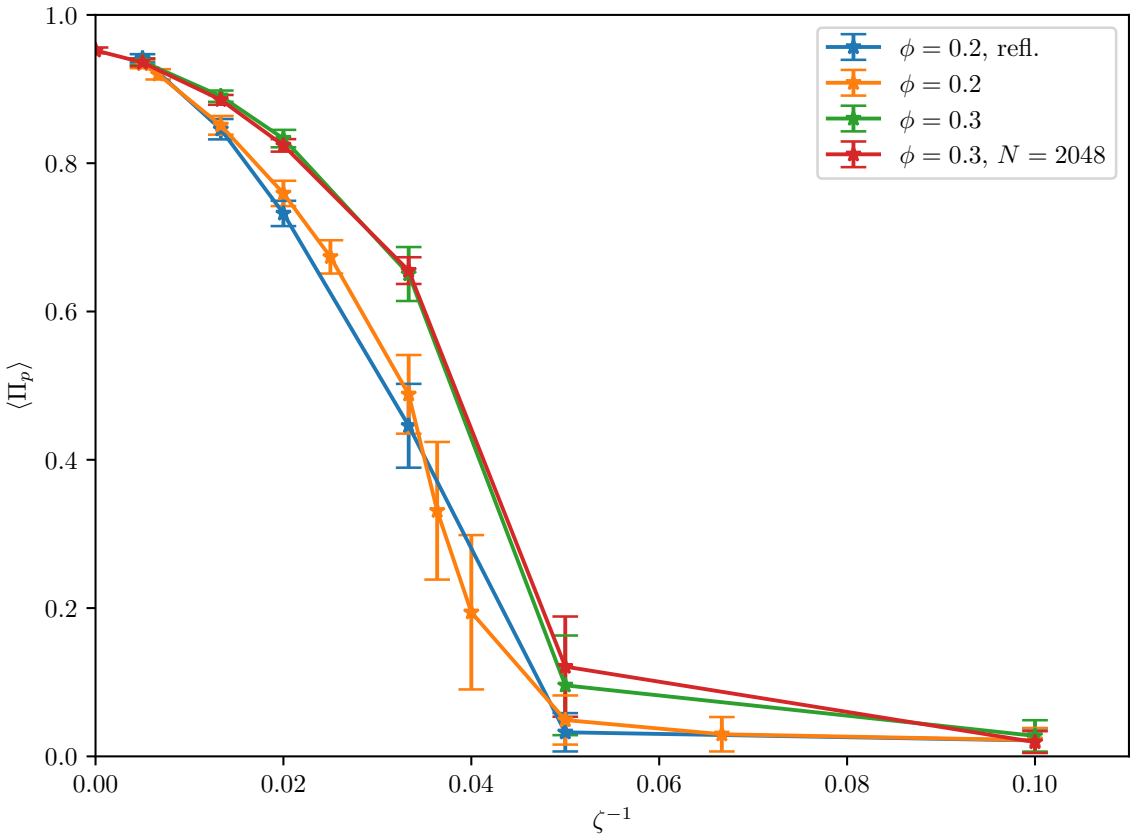

Figure 6.8: Order parameter for different circular systems. The error bars are the standard deviations of the measured order parameter. The average is taken over several thousand τ, starting after the system has stabilized. The walls are repulsive for all except the blue series. Once again we see a critical point where the fluctuation are the largest, between an ordered and unordered phase.

This rotational behaviour clearly calls for a new order parameter, as using the previous definition does not account for the now azimuthally dependent alignment orientation. The projected ordered parameter is defined as

$$\Pi_p \equiv \frac{1}{N} \left| \sum_i \left(\hat{\mathbf{p}}_i \times \frac{\mathbf{r}_i - \mathbf{R}_0}{|\mathbf{r}_i - \mathbf{R}_0|} \right) \cdot \hat{\mathbf{n}} \right|, \tag{6.2}$$

where $\mathbf{R}_0$ is the centre of the domain and $\hat{\mathbf{n}}$ is the normal vector of the plane the particles are confined to. The average value of Π_p for some different ϕ, N and walls are show in fig. 6.8.

The similarity to the order plot for the periodic system is clear, again appearing to have a critical point where the phase become ordered. The blue and orange series in fig. 6.8, representing $\phi = 0.1$ systems with correspondingly reflective and repulsive walls, end up being quite similar, especially for the low ζ^{-1} systems. For intermediate ζ^{-1} the systems with reflective wall have on average a lower measured order. This can be blamed on the fact that particles aggregate much more easily for the repulsive walls, as they simply stop the

particles at the boundary until they change their orientation themselves. This difference is shown in fig. 6.7a and fig. 6.7b, where there is no aggregation along the reflective walls but plenty of particles pushing against the repulsive walls.

As the rotating vortex stabilizes for $\zeta^{-1} \lesssim 0.2$, the difference starts to vanish and both systems will appear like what's shown in fig. 6.7c and fig. 6.7d. This is not surprising, as once the outer layer of particles is in place the walls will not interact with any new particles. But it is still interesting that both types of wall interactions allow this outer layer to form, with onset around the same ζ^{-1} values. The repulsive walls allow aggregation much more easily than the reflective walls, but there is no obvious mechanic that keeps the particles oriented parallel to the boundary, again in contrast to the reflective walls where we can easily imagine a particle reflecting along the walls. Because both the boundary configurations seem to give the same end result, we decide to mainly explore different parameter with the repulsive walls as they are more easily justified for this inertialess approximation.

Increasing the effective area fraction to $\phi = 0.3$ has the effect of increasing the system order, but again the difference start to vanish very low ζ^{-1}. In fig. 6.8 we compare using $N = 1024$ and $N = 2048$. The effect of increasing N seems to be making the variance of the order parameter lower but keeping the average similar. This fits nicely with the idea that increasing N should make the measured values converge to some thermodynamic limit. Additionally, the area fraction covered by the ordered layer seems to remain invariant for increased N. This observation, that the ordered area fraction resembles a state function of density ϕ and effective temperature ζ^{-1}, is also found in [7].

6.3.1 Radial area fraction

Unlike the periodic system which has continuous translational symmetry, for the circular systems it is now interesting to see how measured quantities depend on the distance r from the domain centre. We can therefore consider the radial density $\rho(r)$, which is defined to that the number of particle centres present between r and $r + dr$ is $dN = 2\pi r\rho(r)dr$. This can simply be plotted with a histogram, but the interpretation of this radially depended number density is not obvious when the histogram bin width is much less than the particle diameter $2r_0$. Therefore we convolve $\rho(r)$ with the individual particle area as a function of the distance from its centre. This function is simply[1]

$$h(r)dr = \begin{cases} 2\sqrt{r_0^2 - r^2}dr & -r_0 < r < r_0, \\ 0, & r \geq r_0 \vee r \leq -r_0, \end{cases} \tag{6.3}$$

making the radial area fraction $\phi(r) = \frac{1}{\pi R^2}\int_{-\infty}^{\infty} \rho(r')h(r - r')dr'$ for a circular domain of radius R. This is essentially a smeared out radial number density, so $\phi(r)$ can be thought of as a sort of coarse graining of $\rho(r)$.

The radial area fraction is shown for two different systems: $\phi = 0.2$ and $N = 1024$ with reflective walls in fig. 6.9a and $\phi = 0.3$ and $N = 2048$ with reflective walls in fig. 6.9a. Both start out constant far from the boundary, but as we get closer the area fraction increases and starts to show the clear layered structure of the ordered particles. An exception to this are

[1] It is simple because we are assuming that the particles are many r_0 away from the domain centre. Close to the centre we have to take into account the curvature of the concentric slices between r and $r + dr$ we're considering.

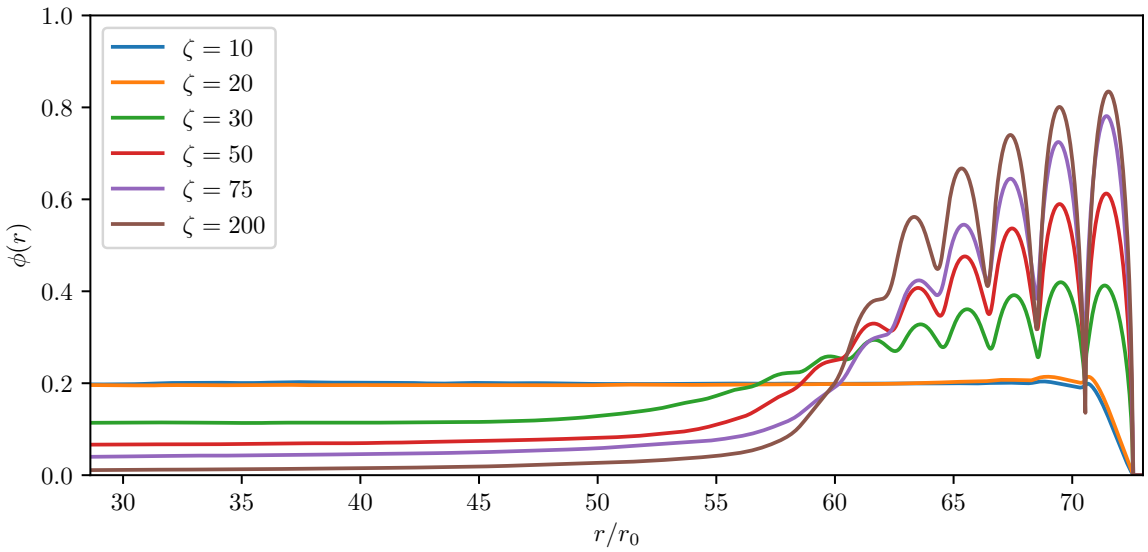

(a) $\phi = 0.2$, $N = 1024$ and reflective walls.

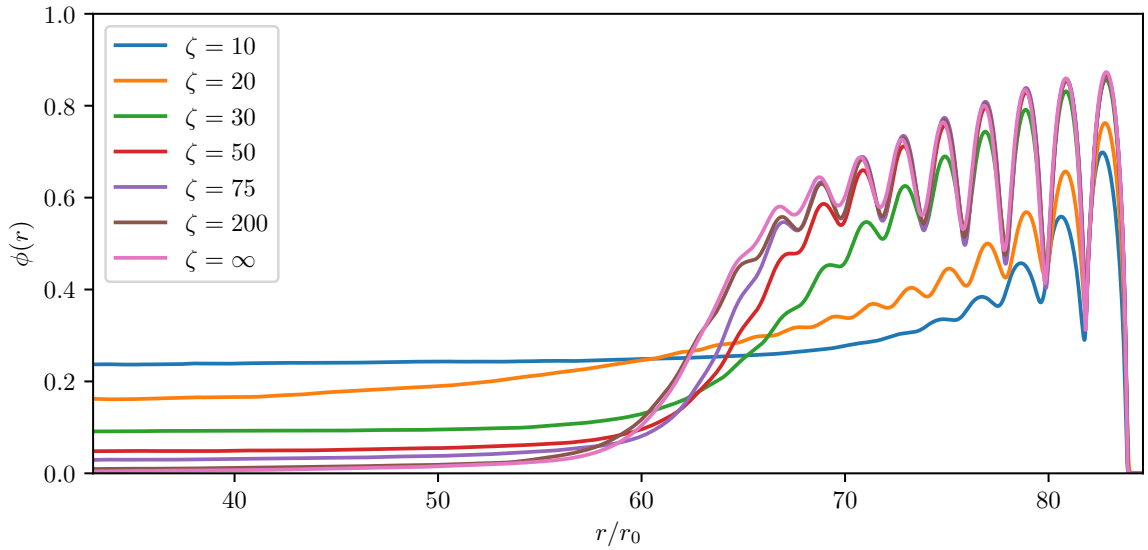

(b) $\phi = 0.3$, $N = 2048$ and repulsive walls.

Figure 6.9: Radial area fraction for two different systems across a range of ζ values. Lower effective temperature ζ^{-1} leads to a more depleted central, gaseous phase and a more sharply layered phase near the boundary.

the high ζ^{-1} plots for the reflective systems, as there is no aggregation along the boundary in these cases and the area fraction remains constant at $\phi = 0.2$ throughout (except very near the boundary, which is caused by the particle centres not being able to be closer than r_0 to the wall). The corresponding systems for the repulsive walls show aggregation even though they have Π_p close to 0, but they increase much less abruptly than the ordered systems. Recalling our discussion of bounded systems in section 4.5 (and the results in appendix C) we should expect a power-law behaviour of $\rho(r)$ for a Vicsek-like system, but here we clearly have something more involved. Close to the boundary the density is so high that it needs to be close packed, making the layer structure and therefore the peaks in fig. 6.9 unavoidable. But also far away from the boundary does it not behave as a power-law, as $\phi(r)$ is essentially constant in this region. Only in the intermediate region, between the constant ϕ region and the close packing region, can one observe something resembling a power-law, and the exponent of this hypothetical power-law would indeed increase with ζ. But we will not attempt to estimate this exponent, as the whole comparison is somewhat dubious.

The existence of two distinct regions, the constant ϕ region and the close packed polar region, suggest that we actually have an interface between two different phases present. The central region resembles a gaseous phase, which is gradually depleted as the temperature ζ^{-1} is lowered and condensed into a condensed polar phase near the boundary of the domain. This interpretation is also supported by fig. 6.10, where we have plotted the speed distribution of the particles and some sample paths. The speed distribution in fig. 6.10a is very clearly bimodal, with the particles in the central region having speeds very sharply peaked around $\tilde{v} = \tilde{v}_a = 1$, while the particles near the boundary are on average slower, with a Gaussian-like distribution peaked around $\tilde{v} \approx 0.92$. The cut-off between the regions was chosen to be the radius at which $\phi(r)$ equalled the total ϕ of the system, which we see from fig. 6.9b is in this case is around $r \approx 65r_0$. The slow-down in the boundary region is in all likelihood caused by the collisions the particles constantly experience from being so densely packed, in contrast to the particles outside of this region which are free to move unaffected at their self-propelled speed v_a. Figure 6.10b shows how the particles move in and out of the different phases, much like how a liquid constantly exchanges particles with its surrounding gas phase at some vapour pressure.

6.3.2 Radial distribution function

We've argued that there are two phases present for the ordered circular systems, but what is the nature of the rotating polar phase at the boundary? From fig. 6.7 we see that it appears close packed, but to properly investigate it we first calculate the radial distribution function $g(r)$, also called the pair correlation function. This function is defined as the average local number density of particles a distance r from any given particle, normalized to be 1 at large distances (meaning distances much greater than the correlation length)[53]. The details of how this normalized are shown in appendix A, as it is not immediately obvious due to the finite size of our systems.

The radial distribution function for a ordered circular system is shown in fig. 6.11, where it compared to $g(r)$ for an unordered circular system and an ordered periodic system. The two latter systems, shown in blue and orange, actually have the most similar $g(r)$, as they both share a strong 1st order peak and a much weaker 2nd order peak at double the

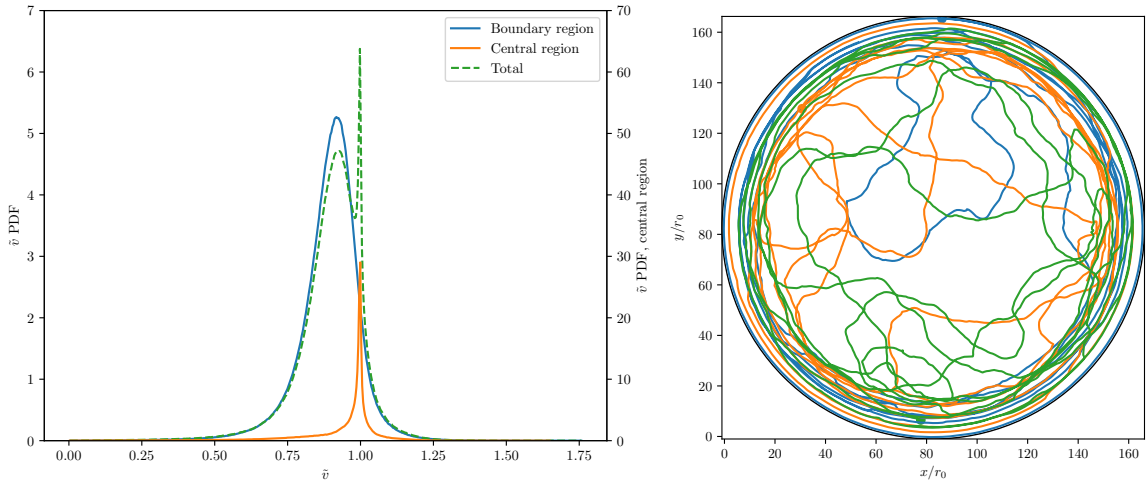

(a) **(b)**

Figure 6.10: Visualising the two different phases present for in the ordered system shown in fig. 6.7d ($\phi = 0.3$, $N = 2048$, $\zeta = 50$, $\tilde{v}_a = 1$). **(a)** shows the probability density function of dimensionless speed $\tilde{v}$. The central region plot has its own axis for readability and the region cut-off used is $r = 65r_0$. In the central region the particles are free to move unhindered at their active speed $v = v_a$, while in the boundary region the particles are slowed down due to them continuously colliding into each other. **(b)** shows the path of 3 different active particles in this system. Here we see how the particles repeatedly switch between the condensed rotating phase at the boundary and the gaseous region in the centre. We also observe that the particles in the gaseous region typically move in straight lines for distances less than the persistence length $\zeta r_0 = 50r_0$.

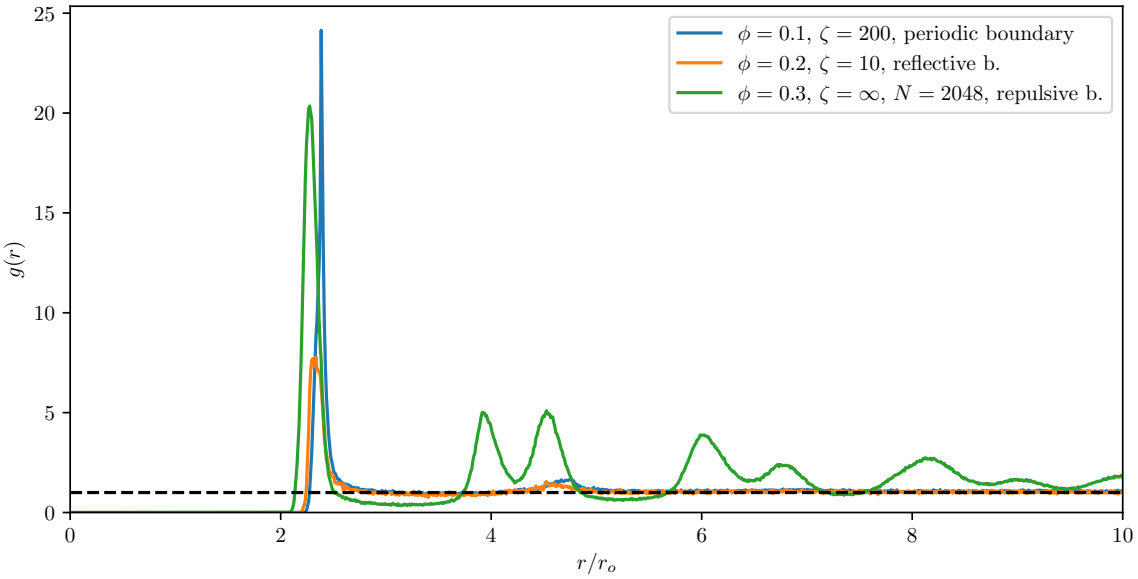

Figure 6.11: Radial distribution for different boundary configurations. $N = 1024$ except for the repulsive case. The dashed line is $g(r) = 1$, which is the value for uncorrelated distances. The blue plot is for the liquid polar phase seen in fig. 6.4c, which has a strong 1st order peak and a much weaker 2nd order peak. The orange plot is for the gaseous confined phase seen in fig. 6.7b, which is similar to the previous plot but with a smaller 1st order peak, as there should be no attraction here. The green plot is for the ordered confined phase seen in fig. 6.14c, where the split peaks are due to the hexatic ordering near the boundary. This plot remains correlated for much larger distances than the two previous plots.

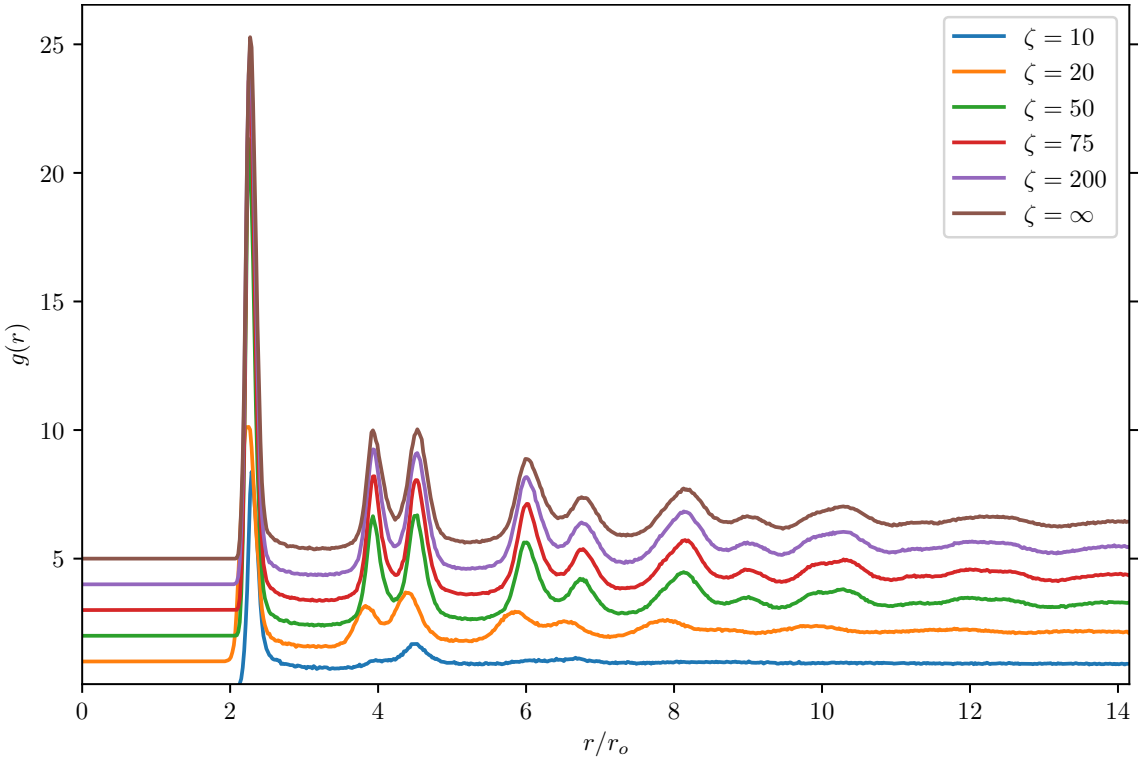

Figure 6.12: Radial distribution for systems with repulsive walls and $\phi = 0.3$, $n = 2048$, showing how the structure melts with increasing effective temperature ζ^{-1}. The plots are evenly shifted vertically for clarity.

separation, before becoming spatially decorrelated at larger r. This shows that the ordered periodic systems are predominately orientationally ordered and only spatially ordered in short chains, with particle separation sharply peaked around the potential minimum shown in fig. 4.5 at $r = 2.38r_0$. The unordered circular sytem has a smaller 1st order peak and is centred around a lower separation at $r \approx 2.33r_0$, suggesting that that the particles separation is not ordered because of attraction but rather repeated collisions, causing the separation to be compressed compared to the ordered periodic system.

The radial distribution function for the ordered circular systems is however of a different character. Here there is again a well defined 1st order peak but also well defined 2nd, 3rd and 4th order peaks. The 1st peak is once again shifted to a lower separation, this time around $r = 2.27r_0$, which can be attributed to compression due to the close packing. The 2nd peak however distinguishes itself from the others systems, as it appears to be split. This is characteristic of hexagonal structure, in which the 2nd nearest neighbour is not at twice the separation of the first neighbour but at $\sqrt{3}$ times the separation[54]. This is indeed where the peaks in fig. 6.11 are located, indicating that the boundary region in the circular systems are hexagonally ordered. This agrees with our discussion of passive dipole particles in section 6.1, where we proved that parallel chains prefer to interlock in a triangular configuration, which is just another name for hexagonal structure.

The radial distribution functions of the repulsive $\phi = 0.3$, $n = 2048$ systems are shown

in fig. 6.12. Here we see that the 2nd peak remains split even for $\zeta = 20$, a point at which Π_p is shown to go to zero in fig. 6.8 and it therefore has no polar order. The disappearance of the peak splitting is indicative of the crystal melting into a liquid, so this tells us that the orientationally ordered phase in the boundary region does not become a liquid until the polar order is already vanished. Instead, the boundary phase is similar to what is called a hexatic phase in KTHNY theory[55–58]. In this theory the hexatic phase is defined as a condensed phase where the translational order is short ranged, but the bond-angle order is still quasi-long-ranged. We will rather use the term to indicate that there is hexatic order, but that the phase is not a single solid crystal. We will go into this more in the next section, but we can still conclude that the circular systems never obtain polar liquid phases with the values of p and v_a we're using, which separates them from the polar phases in the periodic systems and in the Vicsek model.

6.3.3 Hexatic order parameter

To characterize this hexatic phase we turn to the hexatic order parameter, also known as the orientational order parameter. This is defined locally for each particle as

$$\psi_{6j} = \begin{cases} \frac{1}{nn} \sum_{k=1}^{nn} \exp(6i\theta_{jk}), & nn \geq 4 \\ 0, & nn < 4 \end{cases} \tag{6.4}$$

where nn is the number of neighbours around particle j and θ_{jk} is the angle between the centre of particle j and its neighbour k. This parameter will constructively add up so that $|\psi_{6j}| = 1$ if the particles are arranged in a hexagonal pattern, with its complex argument representing the angle at which this hexagon is rotated. Nearest neighbours are defined as particles within the threshold separation $r < 2.6r_0$, which is just above the 1st peak in fig. 6.12. For particles that have less than 4 nearest neighbours it is set to 0, which ensures particles in single chains are not counted as hexatic.

Taking $\langle|\psi_{6j}|\rangle$ is therefore a measure of the total hexatic order of the system. Notice that we are taking the absolute value inside the average, as even for a perfect crystal along the boundary we can't expect the rotation of the hexagonal structure to remain constant put instead rotate with the boundary.

Figure 6.13 shows the measured average hexatic order for the same systems plotted in fig. 6.8, along with the plot the fraction of particles considered to be close packed (particles with 4 or more neighbours within r_c). We only include these "close packed" particles when calculating the average. We see that in all cases that both $\langle|\psi_{6j}|\rangle$ and the close packed fraction increases with lower effective temperature ζ^{-1}. We note that all systems have some degree of close packing in the unordered ζ^{-1} range from fig. 6.8, with the reflective systems having the least due to the anti-clustering effect of the walls. For lower ζ^{-1} values both the hexatic order and the close packed fraction of the $\phi = 0.2$ systems approach each other, showing that the boundary configuration is no longer important.

For the $\phi = 0.3$ systems however, we see that the systems with larger particle number N are on average more close packed and more hexatically ordered. This is in contrast to the orientational order parameter Π_p in fig. 6.8, which seems to converge for larger N. We can blame this difference of the curvature of the circular boundary, which decreases with increasing N and constant ϕ, as they together determine the size of the system. The less

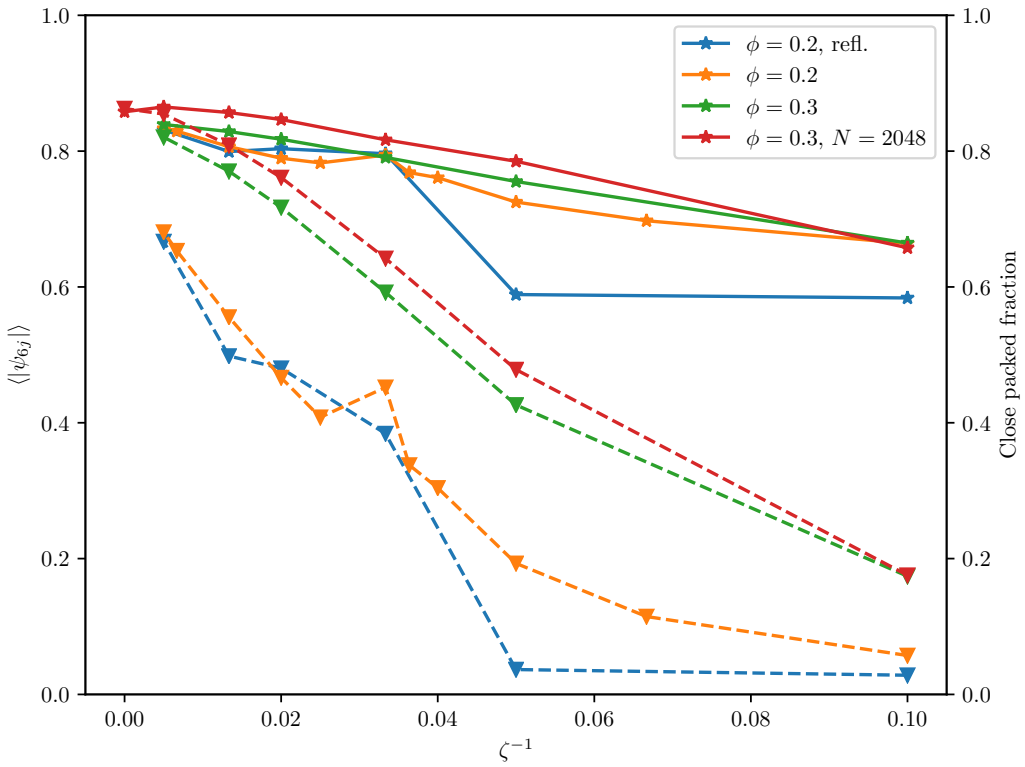

Figure 6.13: Average hexatic order (full lines, stars) as a function of effective temperature ζ^{-1}. We only include the particles that have 4 nearest neighbours ($nn \geq 4$) in the average. We call the fraction of particles where this is the case for the "close packed fraction", which we also plot (dashed lines, triangles). Both values decrease as ζ^{-1} is increased, which represents the hexatic phase near the boundary melting. $N = 1024$ for all except the red series.

curved the boundary is the easier it is to pack hexagonally against it without defects.

This curvature is what keeps the hexatic order from reaching 1 even in the deterministic limit $\zeta^{-1} = 0$. Figure 6.14 shows snapshots of systems with $\phi = 0.3$, $N = 2048$ and progressively lower effective temperatures ζ^{-1}. As the temperature is lowered the particles condense into a hexatically and orientationally ordered layer near the wall. The intermediate temperature system in fig. 6.14e displays a clear interface between the ordered hexatic phase and the unordered gas phase, but the zero temperature system in fig. 6.14f still displays defects. Unlike fig. 6.14e, where the melting occurs primarily in the interface, the zero temperature system has defect fractures originating from the curved walls. These disruptive defects are also likely why Π_p doesn't reach 1 for these systems, as it prevents the particles from staying aligned with their neighbours at all times. For $N \to \infty$ we might then expect both Π_p and $\langle|\psi_{6j}|\rangle$ to approach 1.

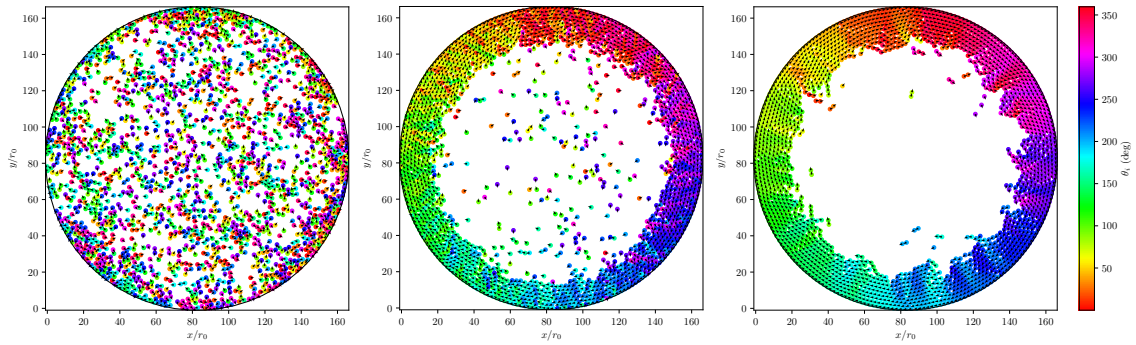

(a) Eff. temperature $\zeta^{-1} = 0.1$ **(b)** $\zeta^{-1} = 0.02$ **(c)** $\zeta^{-1} = 0$

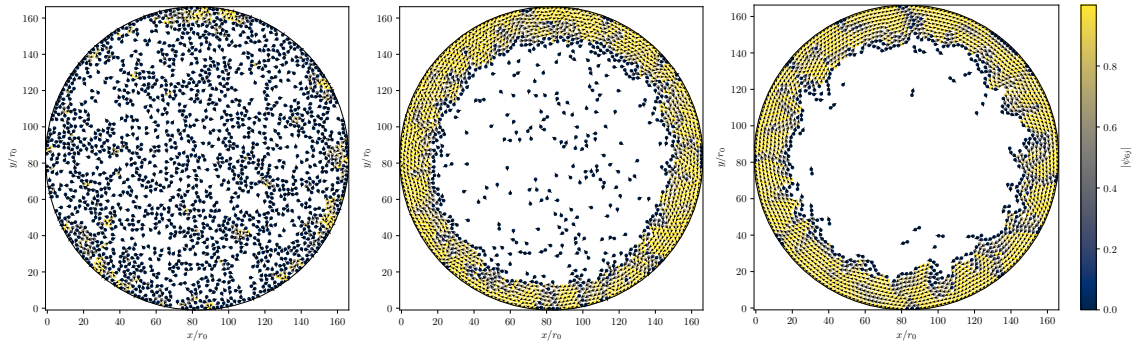

(d) $\zeta^{-1} = 0.1$ **(e)** $\zeta^{-1} = 0.02$ **(f)** $\zeta^{-1} = 0$

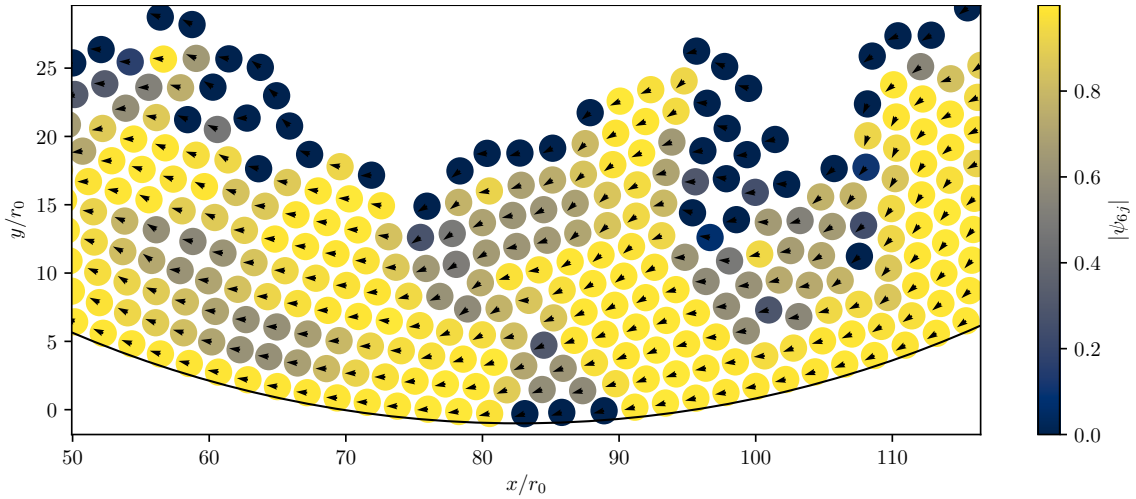

(g) $\zeta^{-1} = 0$, detail

Figure 6.14: Snapshots of a circularly confined systems with area fraction $\phi = 0.3$ and $N = 2048$. The top row colours the particles by orientation and the middle row by hexatic order. **(a)** and **(d)** show a high temperature system, where there is no hexatic or orientational order. **(b)** and **(e)** have lower temperature and display a hexatic and rotating band near the edges. **(c)** and **(f)** are the zero temperature limit, but there are still defects in the ordered hexatic band. **(g)** is a detail of **(f)**, where hexatically ordered domains are separated by defect fractures.

7 | Conclusion

Our results support the use of dipole-dipole interactions as an alignment mechanism for self-propelled particles, and it allows for both unidirectional and rotating collective motion for an ensemble of colloidal particles. This is of theoretical interest, as dipole potentials are the most simple way that anisotropic interactions can occur in electro- and magnetostatics. This is in contrast to other simulations that show emergent vortices, like [7] which is designed to imitate Quincke rollers and therefore involves several different alignment interactions, and like [41] which only uses the original Vicsek model alignment interaction with no direct physical justification. The hydrodynamic dipole potential used in the former paper is even stated to *not* yield any net alignment interaction alone[5], yet we clearly observe alignment in our simulations with our naive implementation of dipole-dipole interactions. Our model uses the same interactions as [9], but our results are novel due to the increased particle number and introduction of rotational diffusion, imitating a thermodynamic system, and by considering circular confinement.

The original Vicsek model was novel because of its simplicity and because it broke a continuous symmetry in a two dimensional system, which would not be possible in an equilibrium systems due to the Mermin-Wagner theorem. Our model is simple in its physical concepts, though decidedly more computationally complex than the Vicsek model. The interactions are also fundamentally different in that our dipole interactions are long-ranged, unlike the unquestionably short-ranged interactions of the Vicsek model. This causes our model to *not* break the classical Mermin-Wagner theorem, but this doesn't mean the phase transitions in our model are trivial.

Using periodic boundary conditions we observe a phase transition from a diffusive gaseous state to polar liquid phase, corresponding to the modern understanding of the flocking transition of the Vicsek model[27]. This transition persist when introducing confinement, but the polar phase is confined to the boundary region and obtains a hexatic spatial order. This condensed phase exchanges particles continuously with a central depleted gaseous region as the hexatic structure is broken up by defects, caused by rotational diffusion and the curvature of the domain. This is again reminiscent of the thermodynamic liquid-gas transition, and is supported by an observed bimodal velocity distributions and a radially dependant density that does not follow a power-law for the whole domain. Models using different translational force components do not observe this clear interface between the boundary and central region, suggesting that our combination of soft-core repulsion and the dipole attraction and repulsion are involved in this two-phase separation.

7.1 Suggested further work

Using particle numbers in the order $\sim 10^3$ was a matter of practicality in our case, as increasing it further would not have allowed us to investigate the parameter space in the same degree. But by rewriting the simulation code in e.g. CUDA or C++ and by implementing a robust interaction cut-off we could make investigating larger N more feasible. It would then be interesting to see if the order parameters Π and Π_p will converge to 1 in the deterministic limit, and if the clear phase interface remains in the confined circular

systems.

Making the code more optimized also enables a more exhaustive study of the phase diagram of the parameter space $(\phi, \zeta^{-1}, \tilde{v}_a, \tilde{p})$. Varying $\tilde{v}_a$ is the most immediate suggested course of action, as we only considered 0 and 1 in our simulations. A larger active speed might be able to break apart the hexatic structure in the circular system into a polar liquid covering the whole domain, which is the more common behavior for confined active matter.

A final intriguing addition is to make the dipole interaction exponentially screened, making all the interactions in the model short-ranged. This is an effect that is easily justified physically for electrostatic interactions and it would be interesting to see how this affects the symmetry breaking behaviour of the model. This would however introduce yet another free parameter into the model: the screening length. Having the phase diagram of the current model mapped out before adding further parameters is advised, as this could provide a logical place to start looking.

Bibliography

[1] M. C. Marchetti et al. “Hydrodynamics of soft active matter”. In: *Reviews of Modern Physics* 85.3 (2013), pp. 1143–1189. ISSN: 00346861. DOI: 10.1103/RevModPhys.85.1143. arXiv: 1207.2929.

[2] Enkeleida Lushi, Hugo Wioland, and Raymond E Goldstein. “Fluid flows created by swimming bacteria drive self-organization in confined suspensions”. In: *Proceedings of the National Academy of Sciences* 111.27 (July 2014), 9733 LP –9738. DOI: 10.1073/pnas.1405698111. URL: http://www.pnas.org/content/111/27/9733.abstract.

[3] Richard A. L. Jones. *Soft Condensed Matter*. New York: Oxford University Press, 2002. ISBN: 0-19-850589-2.

[4] Phillip Hofmann. *Solid State Physics: An Introduction*. 2nd Ed. Weinheim: Wiley-VCH, 2015. ISBN: 978-3-527-41282-2.

[5] Antoine Bricard et al. “Emergence of macroscopic directed motion in populations of motile colloids”. In: *Nature* 503 (Nov. 2013), p. 95. URL: https://doi.org/10.1038/nature12673.

[6] Georg Hermann Quincke. “Ueber Rotationen im constanten electrischen Felde”. In: *Annalen der Physik* 295.11 (Jan. 1896), pp. 417–486. ISSN: 0003-3804. DOI: 10.1002/andp.18962951102. URL: https://doi.org/10.1002/andp.18962951102.

[7] Charles Savoie et al. “Emergent vortices in populations of colloidal rollers”. In: *Nature Communications* 6.1 (June 2015), pp. 1–8. DOI: 10.1038/ncomms8470. URL: http://dx.doi.org/10.1038/ncomms8470.

[8] Tamás Vicsek et al. “Novel Type of Phase Transition in a System of Self-Driven Particles”. In: *Physical Review Letters* 75.6 (Aug. 1995), pp. 1226–1229. DOI: 10.1103/PhysRevLett.75.1226. URL: https://link.aps.org/doi/10.1103/PhysRevLett.75.1226.

[9] Andreas Kaiser, Katarina Popowa, and Hartmut Löwen. “Active dipole clusters: From helical motion to fission”. In: *Physical Review E* 92.1 (July 2015), p. 012301. ISSN: 1539-3755. DOI: 10.1103/PhysRevE.92.012301. URL: https://link.aps.org/doi/10.1103/PhysRevE.92.012301.

[10] Emmy Noether. “Invariante Variationsprobleme”. In: *Nachrichten von der Gesellschaft der Wissenschaften zu Göttingen, Mathematisch-Physikalische Klasse* 1918 (1918), pp. 235–257. URL: http://eudml.org/doc/59024.

[11] Dirk Helbing, Illés J Farkas, and Tamás Vicsek. “Freezing by Heating in a Driven Mesoscopic System”. In: *Phys. Rev. Lett.* 84.6 (Feb. 2000), pp. 1240–1243. DOI: 10.1103/PhysRevLett.84.1240. URL: https://link.aps.org/doi/10.1103/PhysRevLett.84.1240.

[12] J. K. Parrish and W. M. Hamner, eds. *Three Dimensional Animals Groups*. Cambridge, England: Cambridge University Press, 1997.

[13] J T Bonner. "A way of following individual cells in the migrating slugs of Dictyostelium discoideum". In: *Proceedings of the National Academy of Sciences* 95.16 (1998), pp. 9355–9359. ISSN: 0027-8424. DOI: 10.1073/pnas.95.16.9355. URL: https://www.pnas.org/content/95/16/9355.

[14] R Kemkemer et al. "Nematic order-disorder state transition in a liquid crystal analogue formed by oriented and migrating amoeboid cells". In: *The European Physical Journal E* 3.2 (2000), pp. 101–110. ISSN: 1292-8941. DOI: 10.1007/s101890070023. URL: https://doi.org/10.1007/s101890070023.

[15] Yoshie Harada et al. "Sliding movement of single actin filaments on one-headed myosin filaments". In: *Nature* 326 (Apr. 1987), p. 805. URL: https://doi.org/10.1038/326805a0%20http://10.0.4.14/326805a0.

[16] Yoko Yano Toyoshima et al. "Myosin subfragment-1 is sufficient to move actin filaments in vitro". In: *Nature* 328 (Aug. 1987), p. 536. URL: https://doi.org/10.1038/328536a0%20http://10.0.4.14/328536a0.

[17] F J Nédélec et al. "Self-organization of microtubules and motors". In: *Nature* 389 (Sept. 1997), p. 305. URL: https://doi.org/10.1038/38532%20http://10.0.4.14/38532.

[18] Guillaume Grégoire and Hugues Chaté. "Onset of Collective and Cohesive Motion". In: *Physical Review Letters* 92.2 (Jan. 2004), p. 25702. DOI: 10.1103/PhysRevLett.92.025702. URL: https://link.aps.org/doi/10.1103/PhysRevLett.92.025702.

[19] Sriram Ramaswamy. "Active Matter". In: *Journal of Statistical Mechanics* (2017), pp. 1–10. DOI: 10.1515/9783110561913-002. URL: http://www.degruyter.com/view/books/9783110561913/9783110561913-002/9783110561913-002.xml.

[20] David Saintillan. "Rheology of Active Fluids". In: *Annual Review of Fluid Mechanics* 50.October 2017 (2018), pp. 563–92. ISSN: 0066-4189. DOI: 10.1146/annurev-fluid-010816-060049. arXiv: arXiv:1011.1669v3. URL: https://doi.org/10.1146/annurev-fluid-010816-060049.

[21] Michael Rubenstein, Alejandro Cornejo, and Radhika Nagpal. "Programmable self-assembly in a thousand-robot swarm". In: *Science* 345.6198 (2014), pp. 795–799. ISSN: 0036-8075. DOI: 10.1126/science.1254295. URL: http://science.sciencemag.org/content/345/6198/795.

[22] Gábor Vásárhelyi et al. "Optimized flocking of autonomous drones in confined environments". In: *Science Robotics* 3.20 (July 2018), eaat3536. DOI: 10.1126/scirobotics.aat3536. URL: http://robotics.sciencemag.org/content/3/20/eaat3536.abstract.

[23] Étienne Fodor et al. "How Far from Equilibrium Is Active Matter?" In: *Physical Review Letters* 117.3 (2016), pp. 1–6. ISSN: 10797114. DOI: 10.1103/PhysRevLett.117.038103. arXiv: 1604.00953.

[24] John Toner and Yuhai Tu. "Flocks, herds, and schools: A quantitative theory of flocking". In: *Phys. Rev. E* 58.4 (Oct. 1998), pp. 4828–4858. DOI: 10.1103/PhysRevE.58.4828. URL: https://link.aps.org/doi/10.1103/PhysRevE.58.4828.

[25] John Toner and Yuhai Tu. "Long-Range Order in a Two-Dimensional Dynamical XY Model: How Birds Fly Together." eng. In: *Physical review letters* 75.23 (Dec. 1995), pp. 4326–4329. ISSN: 1079-7114 (Electronic). DOI: 10.1103/PhysRevLett.75.4326.

[26] N D Mermin and H Wagner. "Absence of Ferromagnetism or Antiferromagnetism in One- or Two-Dimensional Isotropic Heisenberg Models". In: *Physical Review Letters* 17.22 (Nov. 1966), pp. 1133–1136. DOI: 10.1103/PhysRevLett.17.1133. URL: https://link.aps.org/doi/10.1103/PhysRevLett.17.1133.

[27] Alexandre P Solon, Hugues Chaté, and Julien Tailleur. "From Phase to Microphase Separation in Flocking Models: The Essential Role of Nonequilibrium Fluctuations". In: *Phys. Rev. Lett.* 114.6 (Feb. 2015), p. 68101. DOI: 10.1103/PhysRevLett.114.068101. URL: https://link.aps.org/doi/10.1103/PhysRevLett.114.068101.

[28] András Czirók, H Eugene Stanley, and Tamás Vicsek. "Spontaneously ordered motion of self-propelled particles". In: *Journal of Physics A : Mathematical and General* 30 (1997), pp. 1375–1385. DOI: 10.1088/0305-4470/30/5/009. URL: https://doi.org/10.1088/0305-4470/30/5/009.

[29] David J. Griffiths. *Introduction to electrodynamics*. 3rd ed. Upper Saddle River, NJ: Prentice-Hall, 1999. ISBN: 0-13-805326-X.

[30] Arne T. Skjeltorp. "One- and Two-Dimensional Crystallization of Magnetic Holes". In: *Physical Review Letters* 51.25 (1983). DOI: 10.1103/PhysRevLett.51.2306.

[31] Sabine H.L. Klapp. "Collective dynamics of dipolar and multipolar colloids: From passive to active systems". In: *Current Opinion in Colloid & Interface Science* 21 (Feb. 2016), pp. 76–85. ISSN: 1359-0294. DOI: 10.1016/J.COCIS.2016.01.004. URL: https://www.sciencedirect.com/science/article/pii/S1359029416300036.

[32] Tommaso Brotto et al. "Hydrodynamics of confined active fluids". In: *Physical Review Letters* 110.3 (2013), pp. 1–5. ISSN: 00319007. DOI: 10.1103/PhysRevLett.110.038101. arXiv: arXiv:1208.6448v1.

[33] Kar W Yung, Peter B Landecker, and Daniel D Villani. "An analytic solution for the force between two magnetic dipoles". In: *Magnetic and Electrical Separation* 9 (1998), pp. 39–52. URL: http://www.hindawi.com/journals/psse/1998/079537.abs.html.

[34] Peter B Landecker, Daniel D Villani, and Kar W Yung. "An analytic solution for the torque between two magnetic dipoles". In: *Magnetic and Electrical Separation* 10 (1998), pp. 29–33. URL: http://www.hindawi.com/journals/psse/1999/097902.abs.html.

[35] Jones J E. and Chapman Sydney. "On the determination of molecular fields. —II. From the equation of state of a gas". In: *Proceedings of the Royal Society of London. Series A, Containing Papers of a Mathematical and Physical Character* 106.738 (Oct. 1924), pp. 463–477. DOI: 10.1098/rspa.1924.0082. URL: https://doi.org/10.1098/rspa.1924.0082.

[36] John D Weeks, David Chandler, and Hans C Andersen. "Role of Repulsive Forces in Determining the Equilibrium Structure of Simple Liquids". In: *The Journal of Chemical Physics* 54.12 (1971), pp. 5237–5247. DOI: 10.1063/1.1674820. URL: https://doi.org/10.1063/1.1674820.

[37] E M Purcell. "Life at low Reynolds number". In: *American Journal of Physics* 45.1 (Jan. 1977), pp. 3–11. ISSN: 0002-9505. DOI: 10.1119/1.10903. URL: https://doi.org/10.1119/1.10903.

[38] Ricard Matas Navarro and Suzanne M. Fielding. "Clustering and phase behaviour of attractive active particles with hydrodynamics". In: *Soft Matter* 11.38 (2015), pp. 7525–7546. ISSN: 17446848. DOI: 10.1039/c5sm01061f.

[39] A Einstein. "Über die von der molekularkinetischen Theorie der Wärme geforderte Bewegung von in ruhenden Flüssigkeiten suspendierten Teilchen". In: *Annalen der Physik* 322.8 (1905), pp. 549–560. DOI: 10.1002/andp.19053220806. URL: https://onlinelibrary.wiley.com/doi/abs/10.1002/andp.19053220806.

[40] Herbert B Callen and Theodore A Welton. "Irreversibility and Generalized Noise". In: *Physical Review* 83.1 (July 1951), pp. 34–40. DOI: 10.1103/PhysRev.83.34. URL: https://link.aps.org/doi/10.1103/PhysRev.83.34.

[41] Dieter Armbruster, Sébastien Motsch, and Andrea Thatcher. "Swarming in bounded domains". In: *Physica D* 344 (2017), pp. 58–67. ISSN: 0167-2789. DOI: 10.1016/j.physd.2016.11.009. URL: http://dx.doi.org/10.1016/j.physd.2016.11.009.

[42] Sebastien Motsch and Laurent Navoret. "Numerical simulations of a nonconservative hyperbolic system with geometric constraints describing swarming behavior". In: *Multiscale Modeling and Simulation* 9.3 (2011), pp. 1253–1275. DOI: 10.1137/100794067.

[43] G. Stokes. "On the Effect of the Internal Friction of Fluids on the Motion of Pendulums". In: *Transactions of the Cambridge Philosophical Society* 9 (1851), p. 8.

[44] Clemens Bechinger et al. "Active particles in complex and crowded environments". In: *Reviews of Modern Physics* 88.4 (Nov. 2016), p. 45006. DOI: 10.1103/RevModPhys.88.045006. URL: https://link.aps.org/doi/10.1103/RevModPhys.88.045006.

[45] R Großmann, F Peruani, and M Bär. "Diffusion properties of active particles with directional reversal". In: *New Journal of Physics* 18.4 (Apr. 2016), p. 043009. ISSN: 1367-2630. DOI: 10.1088/1367-2630/18/4/043009. URL: http://stacks.iop.org/1367-2630/18/i=4/a=043009?key=crossref.61d0472da2adae37487bbc9782d81b8e.

[46] Eric W. Weisstein. *Circle Packing*. URL: http://mathworld.wolfram.com/CirclePacking.html.

[47] Brian Ewald. "Weak versions of stochastic Adams-Bashforth and semi-implicit leapfrog schemes for SDEs". In: *Computational Methods in Applied Mathematics* 12.1 (2012), pp. 23–31. ISSN: 16094840. DOI: 10.2478/cmam-2012-0002.

[48] Florencio Balboa Usabiaga, Blaise Delmotte, and Aleksandar Donev. "Brownian dynamics of confined suspensions of active microrollers". In: *Journal of Chemical Physics* 146.13 (2017). ISSN: 00219606. DOI: 10.1063/1.4979494. arXiv: arXiv:1609.08673.

[49] Jörg Bartke. “Computer Simulation of the Stockmayer Fluid”. PhD thesis. Bergische Universität Wuppertal, 2008.

[50] P P Ewald. “Die Berechnung optischer und elektrostatischer Gitterpotentiale”. In: *Annalen der Physik* 369.3 (Jan. 1921), pp. 253–287. ISSN: 0003-3804. DOI: 10.1002/andp.19213690304. URL: https://doi.org/10.1002/andp.19213690304.

[51] P G de Gennes and P A Pincus. “Pair correlations in a ferromagnetic colloid”. In: *Physik der kondensierten Materie* 11.3 (Aug. 1970), pp. 189–198. ISSN: 1431-584X. DOI: 10.1007/BF02422637. URL: https://doi.org/10.1007/BF02422637.

[52] J Vannimenus and G Toulouse. “Theory of the frustration effect. II. Ising spins on a square lattice”. In: *Journal of Physics C: Solid State Physics* 10.18 (1977), pp. L537–L542. ISSN: 0022-3719. DOI: 10.1088/0022-3719/10/18/008. URL: http://dx.doi.org/10.1088/0022-3719/10/18/008.

[53] Peter N. Pusey. “Introduction to Scattering Experiments”. In: *Neutron, X-rays and Light. Scattering Methods Applied to Soft Condensed Matter*. Ed. by Th. Zemb and P. Lindner. Elsevier Science B.V., 2002. ISBN: 9781493302260.

[54] Brodin et al. “Melting of 2D liquid crystal colloidal structure”. In: *Condensed Matter Physics* 13.3 (2011), p. 33601. ISSN: 1607324X. DOI: 10.5488/cmp.13.33601.

[55] J M Kosterlitz and D J Thouless. “Ordering, metastability and phase transitions in two-dimensional systems”. In: *Journal of Physics C: Solid State Physics* 6.7 (1973), pp. 1181–1203. ISSN: 0022-3719. DOI: 10.1088/0022-3719/6/7/010. URL: http://dx.doi.org/10.1088/0022-3719/6/7/010.

[56] B I Halperin and David R Nelson. “Theory of Two-Dimensional Melting”. In: *Physical Review Letters* 41.2 (July 1978), pp. 121–124. DOI: 10.1103/PhysRevLett.41.121. URL: https://link.aps.org/doi/10.1103/PhysRevLett.41.121.

[57] David R Nelson and B I Halperin. “Dislocation-mediated melting in two dimensions”. In: *Physical Review B* 19.5 (Mar. 1979), pp. 2457–2484. DOI: 10.1103/PhysRevB.19.2457. URL: https://link.aps.org/doi/10.1103/PhysRevB.19.2457.

[58] A P Young. “Melting and the vector Coulomb gas in two dimensions”. In: *Physical Review B* 19.4 (Feb. 1979), pp. 1855–1866. DOI: 10.1103/PhysRevB.19.1855. URL: https://link.aps.org/doi/10.1103/PhysRevB.19.1855.

Appendices

A | Calculating the radial distribution function for circularly confined systems

The radial distribution function, $g(r)$, is defined as the average local density of particles a distance r from any given particle, normalized to be 1 at large distances (meaning distances much greater than the correlation length)[53]. In a two-dimensional system, at uncorrelated distances you would expect to find $2\pi r dr\rho$ particles in the distance range between r and $r+dr$ from a given particle, where ρ is the average particle density. Therefore, if you count the number of particles at a given distance from another particle in order to find the radial distribution function, you divide by $2\pi r dr\rho$ to properly normalize it.

First of all, the distances between all the particles are calculated. If you have N particle positions, then this gives $N(N-1)/2$ unique distances. The radial distribution function can then be presented using a histogram, with proper normalization weights. Every distance contributes with a weight $(2\pi r dr\rho N/2)^{-1}$ in their histogram bin, where the first part is the normalization discussed previously (here dr is the bin width) and $N/2$, the half particle count, is there because we are averaging over the distances seen by N particles, but without counting the same distance twice (in other words: only one of r_{ij} and r_{ji} is calculated).

However, this weight does not take into account edge effects for bounded domains. The neighbourhood around a particle near the boundary will on average contain fewer particles than one in the centre, assuming the particles are uniformly distributed throughout the domain. This is illustrated in fig. A.1. Here we see that the particle placed near the edge sees a smaller sector than the ones in the middle. For particles placed near the boundary (area marked B), the seen sector can become less than π, while particles in the centre (area marked C) will always see the full 2π. Thus, what we need to do is to calculate the average visible sector at some r for a particle randomly placed in the image. This is done by double integration over the areas.

For C the integral is trivial, as the visible sector is simply 2π and the area is $\pi(R-r)^2$, R being the radius of the circular domain.

For B however, the case is more complicated. First we need to determine where the small circle with radius r intersects the bounding circle with radius R. If the distance between the two particle centres is D then the equations for the two circles can be written as

$$x^2 + y^2 = R^2 \tag{A.1}$$

$$(x - D)^2 + y^2 = r^2. \tag{A.2}$$

The x value of the point of intersection is then the root of $(x-D)^2 + (R^2 - x^2) = r^2$, which is

$$x = \frac{D^2 - r^2 + R^2}{2D}. \tag{A.3}$$

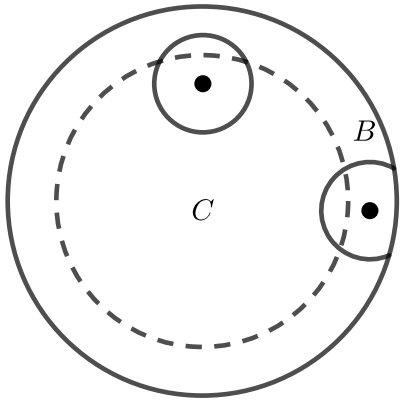

Figure A.1: Illustration of the sector seen by particles found at different positions in the image. The small circle radii and distance from the dashed lines to the edge are equal to r. As we consider larger r, the B area will become larger and the C area smaller.

The angle of the small arc shown in fig. A.1 is then $2\pi - 2\arccos(\frac{x-D}{r})$. The average arc angle over B is then

$$\frac{1}{\pi(R^2-r^2)}\int_{R-r}^{R} 2\pi D\left[2\pi - 2\arccos\left(\frac{R^2-r^2-D^2}{2Dr}\right)\right]dD. \tag{A.4}$$

Summing over the two cases weighted by their area then gives the total average

$$\frac{1}{\pi R^2}\left((R-r)^2 2\pi + \int_{R-r}^{R} 2\pi D\left[2\pi - 2\arccos\left(\frac{R^2-r^2-D^2}{2Dr}\right)\right]dD\right). \tag{A.5}$$

This integral is solvable, but using a tool like Maple is recommended as it is quite involved. The closed-form expression is

$$\frac{1}{\pi R^2}(2(R-r)^2\pi^2 - \frac{\pi}{R-r}(\pi R^3 - \pi R^2 r + 4\arcsin\left(\frac{r}{2R}\right)R^3 - 4\arcsin\left(\frac{r}{2R}\right)R^2 r - \\ 4R^2 r\pi + 6Rr^2\pi - 2r^3\pi - \pi R^2(R-r) + \frac{1}{\sqrt{4R^2-r^2}}(4R^3 r - 4R^2 r^2 - Rr^3 + r^4))). \tag{A.6}$$

This expression is used instead of 2π in the histogram normalization weight. It also only needs to be calculated once per histogram bin, so the computational cost is not large. These results are verified by looking at randomly generated uniform particle positions, which should have a flat $g(r)$. This is shown in fig. A.2. The uncorrected plot overestimates the particles expected to be present for each r, so it drops below 1. For our confined systems, where the density is highest near the walls, leaving this uncorrected would be even more noticeable.

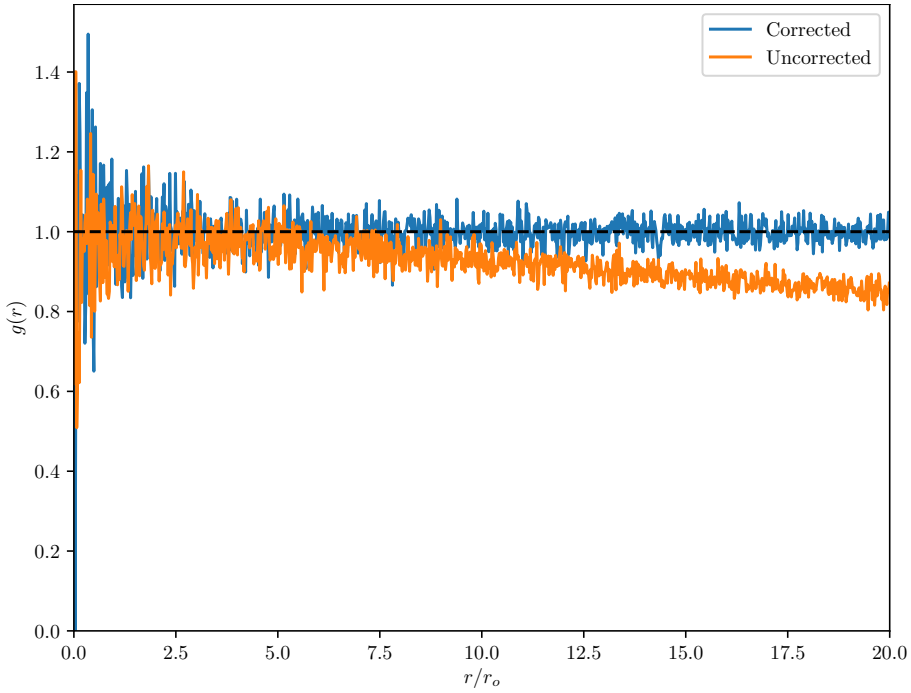

Figure A.2: Calculated $g(r)$ for a system with the same parameters as fig. 6.12, but with randomly distributed particle positions uniformly in the circular domain. The uncorrected plot drops noticeably below the expected $g(r) = 1$ line, while the corrected plot remains centred at this line throughout.

B | Using weaker or stronger dipole moment

As stated in section 5.1, $\tilde{p} = 3$ was chosen because it was deemed to be a satisfactory value for interesting phase behaviours with a changing ζ. There is no rigorous argument for why this value is special, but some decisions have to be made in order to limit the scope of the work. Running simulations over a range of $\tilde{p}$ values, like a large N version of [9], is something that can be considered for further work.

In this work we were primarily interested in how pure dipole-dipole interactions play into active matter dynamics, and increasing $\tilde{p}$ does indeed make these interactions more dominant. But at some point the dipole interactions will be so strong that the particles will form chains for all $\zeta > 1$, which is the region where we expect to see possible alignment behaviour. For example, see fig. B.1c where $\tilde{p} = 10$ and the rotational noise is high with $\zeta = 2$. Due to the high dipole moment the particles spend almost all their time in chains, but they jump between different chains frequently as they collide. This strongly directional clustering replaces the more classic gas behaviour we would observe for lower $\tilde{p}$.

If the noise is entirely removed nothing will stop the particles from forming one long travelling band of chains. This is what's shown in fig. B.1d, where the boundaries have been made periodic and the density lowered to $\phi = 0.025$. An interesting behaviour here is that chains appear to zip and unzip when they collide. This is a consequence of the strong directional attraction of the chains, which force the particles to follow wherever the particle in front of it goes. So if a single particle is knocked out of the chain or becomes attached to another, the rest of its tail will follow.

Going the other way, we investigate what happens when the dipole moment is lowered to $\tilde{p} = 1$. Initializing from a ordered rotating state like fig. 6.7c can tell us if this dipole moment still can sustain the rotating behaviour. As shown in fig. B.1a, the dipole moment is indeed too low to keep the particles aligned parallel to the boundary and they instead end up pushing against the repulsive wall like the unordered state in fig. 6.7a. Switching instead to reflective walls does not help the particles get unstuck, as the outer layer is kept in place by the particles pushing outwards but they will not align themselves with this outer player.

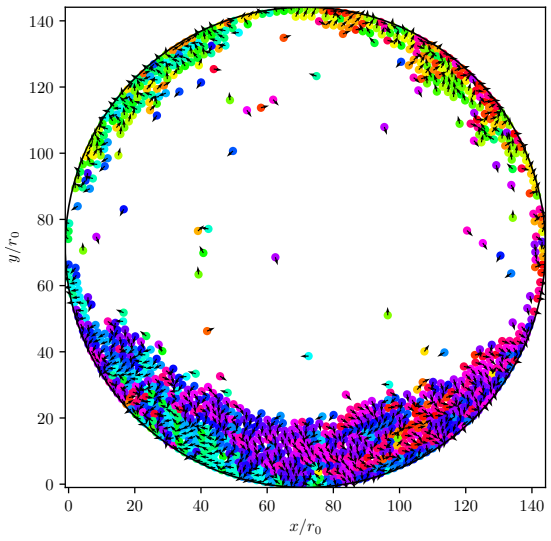

(a) $\tilde{p} = 1$, $\zeta = 200$, $\phi = 0.2$, repulsive walls.

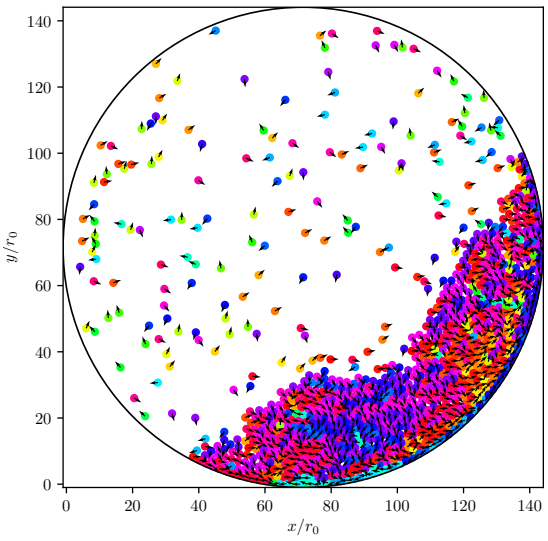

(b) $\tilde{p} = 1$, $\zeta = 200$, $\phi = 0.2$, reflective walls.

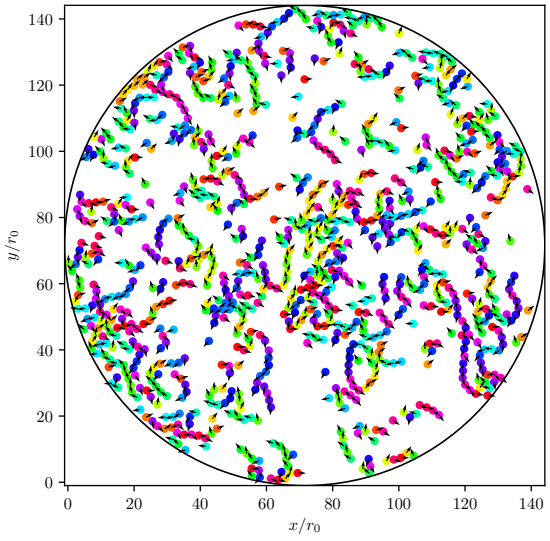

(c) $\tilde{p} = 10$, $\zeta = 2$, $\phi = 0.2$, reflective walls.

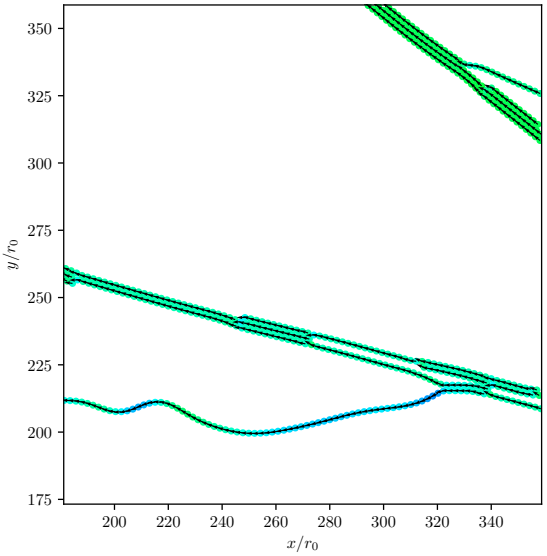

(d) $\tilde{p} = 10$, $\zeta = \infty$, $\phi = 0.025$, periodic boundaries.

Figure B.1: Snapshots of different systems using $\tilde{p} = 1$ or 10.

C | Vortex solution of the macroscopic Vicsek model

In addition to the original microscopic formulation of the Vicsek model presented in chapter 3, it can be expressed as a macroscopic model by coarse graining the individual particles into a density scalar field ρ and a orientation vector field $\mathbf{\Omega}$. Following the formulation in [42], a stationary solution of the macroscopic Vicsek model satisfies

$$\boldsymbol{\nabla} \cdot (\rho \mathbf{\Omega}) = 0, \tag{C.1}$$

$$c(\mathbf{\Omega} \cdot \boldsymbol{\nabla})\mathbf{\Omega} + \lambda(Id - \mathbf{\Omega} \otimes \mathbf{\Omega})\frac{\boldsymbol{\nabla}\rho}{\rho} = 0, \tag{C.2}$$

where the first equation ensures mass conservation and the second provides the alignment and noise term. λ increases with the noise amplitude, in our case either η for the Vicsek model or D_r for the active dipoles.

A rotationally symmetric solution to these equations is

$$\rho(r) = Cr^{c/\lambda}, \quad \mathbf{\Omega} = \mathbf{e}_\theta, \tag{C.3}$$

where $\mathbf{e}_\theta$ is the azimuthal unit vector in polar coordinates.

In a Vicsek-like active matter model, we should therefore expect the radial density to increase with r, with higher noise providing higher λ and flatter $\rho(r)$. Simulations of the microscopic Vicsek model in circular confinement do appear to follow this power law closely[41], but the general behaviour is also present for circularly confined experimental Quincke rollers[7]. See fig. C.1 for snapshots of these two systems.

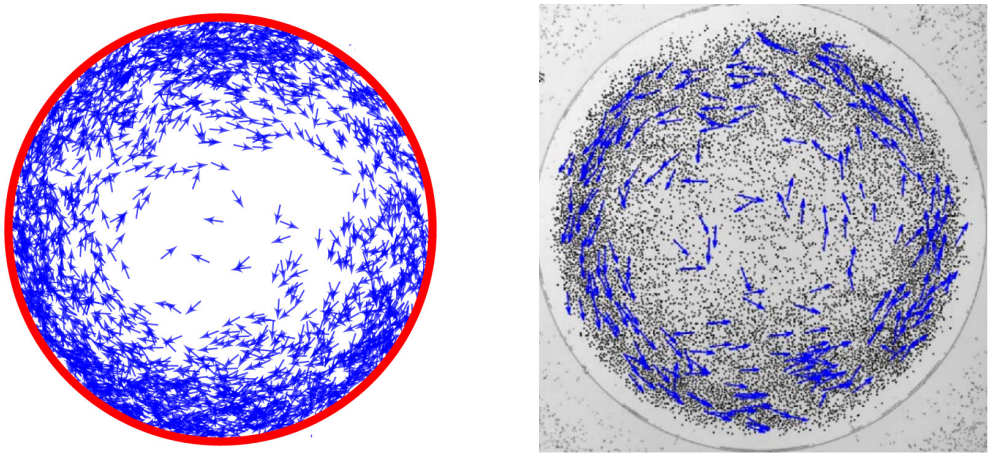

(a) **(b)**

Figure C.1: Snapshots of vortex states. (a) is from a simulation of the microscopic Vicsek model, following eq. (C.3) closely (reused from [41]). (b) is a collection of Quincke rollers, with confinement radius 1.35 mm and area fraction 5×10^{-2} (from [5], CC BY 4.0).

D | Attached animations

Some animated systems are included as attachments. The counter in the animations are the time passed in units of τ and the colouring is orientational according to fig. 3.2d. The videos use the following parameters:

- `stable_chains.mp4`:
  periodic boundary conditions, $\tilde{v} = 0$, $\phi = 0.1$, $D_r = 0.01$, $N = 1024$. Same as fig. 6.1c
- `collapsed_chains.mp4`:
  periodic boundary conditions, $\tilde{v} = 0$, $\phi = 0.1$, $D_r = 0.1$, $N = 1024$. Same as fig. 6.1d
- `peridic_polar_liquid.mp4`:
  periodic boundary conditions, $\tilde{v} = 1$, $\phi = 0.1$, $\zeta = \infty$, $N = 1024$. Same as fig. 6.4d
- `confined_gas.mp4`:
  repulsive circular confinement, $\tilde{v} = 1$, $\phi = 0.2$, $\zeta = 10$, $N = 1024$. Same as fig. 6.7b
- `rotating_with_noise.mp4`:
  repulsive circular confinement, $\tilde{v} = 1$, $\phi = 0.3$, $\zeta = 30$, $N = 2048$.
- `rotating_no_noise.mp4`:
  repulsive circular confinement, $\tilde{v} = 1$, $\phi = 0.3$, $\zeta = \infty$, $N = 2048$. Same as fig. 6.14c.
- `strongly_transient.mp4`:
  repulsive circular confinement, $\tilde{v} = 1$, $\phi = 0.2$, $\zeta = 150$, $N = 1024$. Included because of its interesting transient behavior before stabilizing as a vortex.
- `periodic_high_p.mp4`:
  periodic boundary conditions, $\tilde{p} = 10$, $\tilde{v} = 1$, $\phi = 0.025$, $\zeta = \infty$, $N = 1024$. Same as fig. B.1d. Initialized from a vortex.
- `confined_high_p.mp4`:
  reflective circular confinement, $\tilde{p} = 10$, $\tilde{v} = 1$, $\phi = 0.2$, $\zeta = 2$, $N = 1024$. Same as fig. B.1c. Initialized from a vortex.

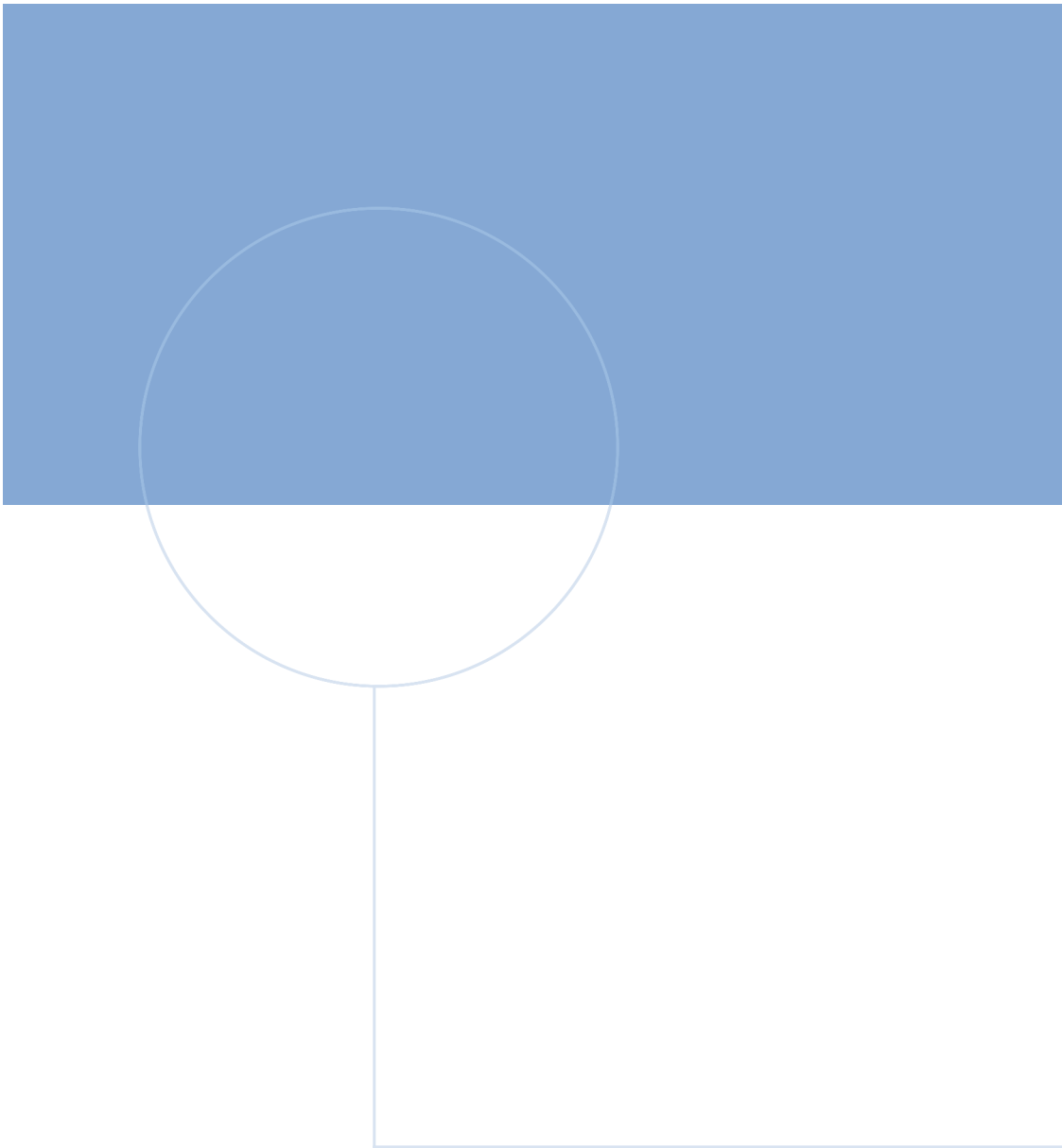

NTNU
Norwegian University of
Science and Technology